Master Thesis of Science

A new LLJ model and its application to wind turbine power analysis

Yifei He

25/07/2014

European Wind Energy Master - EWEM- Rotordesign Track

A new LLJ model and its application to wind turbine power analysis

Master of Science Thesis

For obtaining the degree of Master of Science in Engineering Wind Energy at Technical University of Denmark and in Aerospace Engineering at Delft University of Technology.

Yifei He

25/07/2014

European Wind Energy Master - EWEM
Delft University of Technology
Denmark Technical University
DTU Wind Energy

European Wind Energy Master - EWEM
Of
Rotordesign Track

The undersigned hereby certify that they have read and recommend to the European Wind Energy Master - EWEM for acceptance a thesis entitled **“A new LLJ model and its application to wind turbine power analysis”** by **Yifei He** in partial fulfillment of the requirements for the degree of **Master of Science**.

Dated: 25/07/2014

Supervisor:
Dr. A. Peña of Denmark Technical University

Supervisor:
Ir. M. Holtslag of Delft University of Technology

Reader:
Prof.dr. G.J.W. van Bussel of Delft University of Technology

Reader:
Dr.ir. W.A.A.M Bierbooms of Delft University of Technology

Summary

Low level jets (LLJs) are situations where wind speed maximums occurs close to the surface. Unfortunately, the influence of LLJs on wind turbine power production is still difficult and costly to quantify due to that the existing LLJ models are all time-based. The work that is done in this report addresses the research question should low level jets be included in offshore wind turbine design.

In this report, data from an offshore meteorology site IJmuiden is studied to analyze the occurrences and properties of LLJs. It is found that LLJs are frequent phenomena which occur at 1/3 of the days in a year. Most of the LLJs are observed when the atmosphere is very stable, which means stability is a crucial factor to LLJs. Based on the diabatic wind profile model, an assumption is made that the LLJ wind speed profile is related to friction velocity, Obukhov length and roughness length. The observed data is divided into groups by Obukhove length to find the relationship between these factors and the wind speed profile of a LLJ. It is found that the LLJ model can be fully defined by introducing an intersection height. The newly developed model is applied to wind turbine power analysis. The theoretical results agree with the simulations on Bladed, which show that power production variation due to the occurrence of LLJs depends on multiple factors, these are: Obukhov length, friction velocity, wind turbine hub height and wind turbine rotor radius. The power production of 5 MW reference wind turbine due to the occurrence of LLJs differs from -0.27 to +0.31 MW compared to the expected power production considering constant wind speed across the rotor disc when Obukhov length varied from 60 to 180 m. The results also imply the applicability of the new LLJ model. It is recommended that wind turbine engineers should include LLJs in wind resource assessment. This LLJ model can be further improved by future research with data obtained from onshore meteorology sites. In addition, this research can be extended by applying this model to fatigue and load studies.

Acknowledgements

I wish to thank the people working for EWEM program, who offered me the best opportunity and a perfect academic environment.

I would like to express all my gratitude to my supervisors Alfredo Peña, Maarten Holtslag and Wim Bierbooms, who gave me advises and helped me in my master thesis work.

Finally I would like to thank my family and all of my friends for the constant support and love.

Delft, The Netherlands
25/07/2014
Yifei He

Contents

List of Figures

List of Tables

Nomenclature

Latin Symbols

A	Parameter A	$[-]$
A_i	The segment of rotor plane area	$[m^2]$
a	Coefficient a	$[-]$
b	Coefficient b	$[-]$
C_P	Power coefficient	$[-]$
C_p	Heat capacity at constant pressure	$[JK^{-1}]$
c	Coefficient c	$[-]$
c_1	Empirical parameter c_1	$[-]$
d	Coefficient d	$[-]$
dz	The height interval	$[m]$
f_c	Coriolis parameter	$[s^{-1}]$
g	Gravity (9.81 ms^{-2})	$[ms^{-2}]$
H	Surface heat flux	$[Wm^{-2}]$
$KE_{profile}$	The kinetic energy flux of a particular wind profile	$[Jm^{-2}s^{-1}]$
L	Obukhov length	$[m]$
L_{MBL}	Middle boundary layer length scale	$[m]$
P	Power	$[W]$
R	Wind turbine rotor radius	$[m]$
Ri_b	The bulk Richardson number	$[-]$
Ri_f	The flux Richardson number	$[-]$
Ri_g	The gradient Richardson number	$[-]$

$\overline{T}$	Average temperature	$[K]$
U	Wind speed	$[ms^{-1}]$
$U(z)$	Wind speed at height z	$[ms^{-1}]$
$U_{diabatic}$	Diabatic wind speed	$[ms^{-1}]$
U_{eq1}	Equivalent wind speed with definition 1	$[ms^{-1}]$
U_{eq2}	Equivalent wind speed with definition 2	$[ms^{-1}]$
U_{eq3}	Equivalent wind speed with definition 3	$[ms^{-1}]$
U_{diff}	The wind speed difference between diabatic wind speed and LLJs wind speed	$[ms^{-1}]$
U$_g$	Eastward component of geostrophic wind	$[ms^{-1}]$
U_i	Wind speed corresponds to the segment of rotor plane area	$[ms^{-1}]$
$U_{\log}$	The wind speed calculated by simple log wind profile at height z	$[ms^{-1}]$
U_{LLJs}	LLJs wind speed	$[ms^{-1}]$
U_{ref}	The reference wind speed at reference height z_{ref}	$[ms^{-1}]$
u_*	Friction velocity	$[ms^{-1}]$
u	Eastward moving Cartesian wind components	$[ms^{-1}]$
$\overline{u'w'}$	Kinematic flux of U-momentum	$[Jm^{-2}s^{-1}]$
V$_g$	Northward component of geostrophic wind	$[ms^{-1}]$
v	Northward moving Cartesian wind components	$[ms^{-1}]$
v_r	The velocity along beam velocity	$[ms^{-1}]$
$\overline{v'w'}$	Kinematic flux of V-momentum	$[Jm^{-2}s^{-1}]$
x	Cartesian coordinate towards east	$[-]$
y	Cartesian coordinate towards north	$[-]$
Z_{hub}	Wind turbine hub height	$[m]$
Z_i	Mean height of height segments	$[m]$
z	The height	$[m]$
z_i	The height of ABL	$[m]$
z_{ref}	The reference height	$[m]$
z_s	The height of surface layer	$[m]$
z_{int}	The height where diabatic wind speed equal to LLJs wind speed	$[m]$
z_0	Roughness length	$[m]$

Greek Symbols

α	Parameter α	$[-]$
α_c	Charnock parameter (≈ 0.015)	$[-]$
β	Empirical parameter	$[-]$
Δf	Doppler shift	$[s^{-1}]$

ζ	Atmospheric stability parameter	$[-]$
θ	Potential temperature	$[K]$
θ_v	Virtual potential temperature	$[K]$
κ	The von Kármán constant (0.41)	$[-]$
λ_l	The laser wavelength	$[m]$
ρ	Air density	$[K]$
τ_0	Surface shear stress	$[Pa]$
$\psi\left(\frac{z}{L}\right)$	Stability parameter	$[-]$
$\overline{w'\theta_v'}$	Kinematic heat flux in the vertical direction	$[Wm^{-2}]$

Chapter 1

Introduction

The offshore wind power market is developing rapidly due to advantages regarding wind resource and noise limit offshore. In Europe, 12 offshore projects are under construction at present, which are expected to increase the installed capacity from 6.4 GW to around 9.4 GW. The wind shear, which is an important research topic in wind energy, is closely related to wind turbine fatigue and power performance. Low level jets (LLJs) are typical phenomena with strong wind shear, which may occur under stable atmospheric conditions. LLJs have mostly been studied onshore [1, 2, 3], but detailed LLJs occurrence and property offshore are unknown.

LLJs can generate unexpected high wind speed and cause a strong wind shear below and above the maximum wind speed height, which is very crucial to wind power engineering. The high wind speeds make LLJs attractive for wind energy purposes [3, 4]. At the same time, the dramatic change in vertical wind shear makes them risky to wind turbine blades [2]. The International Electrical Commissions Normal Turbulence Models provide inflow conditions for wind turbine design without the consideration of the LLJs in stable boundary layers [5]. Lacking of a simple model for such phenomenon causes suboptimal wind energy production and turbine failures [3, 6]. Moreover, the neutral log wind profile and diabatic log wind profile, which are mostly used in wind turbine power analysis, are only reliable under neutral conditions. Unfortunately the characteristics of LLJs are not included in the simple wind profiles. Therefore, it is questionable if simple log wind profiles used in wind turbine design are reliable to model all the possible wind conditions under stable condition.

The main research question that arises is: Should low level jets be included in offshore wind turbine design?

The sub questions are:

- How is the occurrence of LLJs offshore?
- Which parameters define the shape of LLJs?
- Is it possible to define an engineering model of LLJs?

- What is the impact of LLJs on wind turbine power production?

The corresponding hypothesis are:

- LLJs frequently occur offshore;
- The parameters are Obukhov length, friction velocity, roughness length, air pressure, air temperature;
- An engineering model of LLJs can be defined;
- Wind turbines gain power when LLJs occur.

In this research the objective is to build a new LLJ model which can be easily used for wind turbine power (and load) analysis and simulations. Some relevant research can be found in the literature. For instance Wharton used one year data from West Coast North American to find out the impact of atmospheric stability to the power curves of tall wind turbines [7]. Wagner implemented an experiment to explain the relationship between the vertical wind shear in front of the rotor plane and the wind turbine power performance [8].

The structure of the report is summarized below.

- Chapter 1: The LLJs and its relation to offshore wind turbine are introduced;
- Chapter 2: Atmospheric stability, simple log wind profile, diabatic wind profile and LLJs are introduced in detail;
- Chapter 3: The installed sensors (metmast and LiDAR) at the offshore meteorology site IJmuiden are described;
- Chapter 4: The process of data treatment is explained;
- Chapter 5: The climate at IJmuiden and the observed wind profiles are illustrated. Detailed information and discussion of observed LLJs can also be found in this chapter;
- Chapter 6: The process of developing the LLJ model, verification and sensitivity analysis are included;
- Chapter 7: The application of the LLJ model on wind turbine power analysis is accomplished and verified with Bladed simulation;
- Chapter 8 and Chapter 9: The main findings of the thesis are concluded, some constructive criticisms are pointed and suggestions on further research are made.

Additional observed LLJs information can be found in the Appendix at the end of this report.

Chapter 2

Theoretical background

In this chapter, background knowledge related to neutral wind profile, diabatic wind profile, atmospheric stability and LLJs is presented.

2.1 The surface layer and the neutral wind profile

The atmospheric boundary layer (ABL) is defined as the part of the troposphere that is influenced directly by earth's surface. The average height of ABL is 1km above the ground. The estimated height can be calculated by Equation 2.1 [9].

$$z_i = \frac{c_1 u_*}{f_c} \tag{2.1}$$

Where z_i is the height of ABL, u_* is the friction velocity, c is advised by Plate [10] to take as 0.2 in an empirical manner, and f_c is the Coriolis parameter. At IJmuiden the Coriolis parameter is equal to $1.12 \times 10^{-4}\ s^{-1}$.

Inside the ABL there is a region defined as the surface layer z_s, which is the bottom 10% of the ABL. It can be calculated by Equation 2.2 [9].

$$z_s = 0.1 z_i \tag{2.2}$$

In the surface layer, the wind profile can be determined by using dimensional analysis based on the stationary neutral atmosphere and flat terrain assumptions.

$$\frac{dU}{dz} = \frac{u_*}{\kappa z} \tag{2.3}$$

Where U is the wind speed and κ is the von Kármán constant. Integrate Equation 2.3 from z_0 to z,

$$U(z) = \frac{u_*}{\kappa} \ln(z) + const \tag{2.4}$$

The constant in equation 2.4 is defined in accordance with the height where the wind profile turns zeros, this height is called roughness length, leads to $const = -\frac{u_*}{\kappa}\log(z_0)$. Thus the wind profile can be expressed as,

$$U(z) = \frac{u_*}{\kappa}\ln\left(\frac{z}{z_0}\right) \tag{2.5}$$

Where $U(z)$ is the wind speed at height z.

The simple logarithmic wind profile which is widely used in wind turbine design can then be inferred from Equation 2.5, which is Equation 2.6.

$$U_{\log} = U_{ref}\frac{\log(z/z_0)}{\log(z_{ref}/z_0)} \tag{2.6}$$

Where $U_{\log}$ is the wind speed calculated by simple log wind profile at height z, U_{ref} is the reference wind speed at reference height z_{ref}, z_0 is the roughness length.

Over oceans, z_0 can be related to friction velocity empirically as $z_0 = \alpha_c\frac{{u_*}^2}{\mathrm{g}}$, where the Charnock parameter $\alpha_c \approx 0.015$ and the gravity $g = 9.81m/s$. Then the equation can be rewritten as,

$$z_0 = 0.015\frac{{u_*}^2}{\mathrm{g}} \tag{2.7}$$

This equation is known as Charnocks relation [11].

2.2 Atmospheric stability and the diabatic wind profile

Monin and Obukhov used similarity theory to describe the surface layer [9], which is called Monin-Obukhov similarity or surface-layer similarity. Wind profiles which are either based on surface-layer theory or Monin-Obukhov scaling are only valid in the surface layer, such as the simple log wind profile mentioned above (see Equation 2.6) and diabatic wind profile, see Equation 2.17.

Atmospheric stability is defined as the resistance of atmosphere to its vertical motion. When the atmosphere is stable, the air flow remains laminar. The degree of atmospheric stability can be determined by using stability parameters, which are normally ratios between stabilizing factor and destabilizing factor. The Richardson number is one of the characteristic stability parameters.

A surface-layer scaling parameter $\zeta = z/L$ can also be used to describe the atmospheric stability. According to this parameter, the stability depends on height and Obukhov length L. The Obukhov length L is the length scale defined by Monin-Obukhov similarity. Monin-Obukhov similarity suggests that there are 4 parameters which define the surface layer wind and temperature conditions. These parameters are surface heat flux $H = C_p\rho\overline{w'\theta'}$ (Where C_p is heat capacity at constant pressure and ρ is the air density), height z, buoyancy parameter g/θ (where θ is potential temperature), and surface shear stress

τ_0. Based on these 4 parameters, the length scale Obukhov length can be defined by dimensional analysis [9],

$$u_* = (\tau_0/\rho)^{1/2} \tag{2.8}$$

$$L = \left[u_*^3/\kappa(g/\theta)\right]\left[-H/C_p\rho\right]^{-1} = \frac{-u_*^3 C_p \rho \theta}{\kappa g H} \tag{2.9}$$

Expressed in virtual potential temperature and virtual temperature heat flux [9],

$$L = \frac{-\overline{\theta_v} u_*^3}{\kappa g (\overline{w'\theta_v{}'})} \tag{2.10}$$

Where θ_v is the virtual potential temperature and $\overline{w'\theta_v'}$ is the kinematic heat flux in the vertical direction.

The data needed to calculate the kinematic heat flux is often not available in regular observation data. As a substitution, relation between the bulk Richardson number and the Obukhov length is applied. This method can be found in literature [12, 13, 14]. The bulk Richardson number is widely used in meteorological studies because of the convenience and availability of the needed data. It is derived from the flux Richardson number [9].

$$Ri_f = \frac{\left(\frac{g}{\overline{\theta_v}}\right)\left(\overline{w'\theta_v{}'}\right)}{\left(\overline{u'w'}\right)\frac{\partial \overline{u}}{\partial z} + \left(\overline{v'w'}\right)\frac{\partial \overline{v}}{\partial z}} \tag{2.11}$$

Where v and u are northward and eastward moving Cartesian wind components, $\overline{u'w'}$ and $\overline{v'w'}$ are the kinematic flux of u-momentum and v-momentum in the vertical direction. The flux Richardson number is the ratio of the buoyant production to the mechanical production term in the TKE budget equation (Stull, 1988). The kinematic flux is proportional to the negative value of the gradient, which can be expressed as $\overline{w'\theta_v{}'} \propto -\frac{\partial \overline{\theta_v}}{\partial z}$, $\overline{u'w'} \propto -\frac{\partial \bar{u}}{\partial z}$, $\overline{v'w'} \propto -\frac{\partial \bar{v}}{\partial z}$. Based on this relationship a new ratio can be developed, which is called the gradient Richardson number Ri_g [9],

$$Ri_g = \frac{\left(\frac{g}{\overline{\theta_v}}\right)\frac{\partial \overline{\theta_v}}{\partial z}}{\left[\left(\frac{\partial \overline{u}}{\partial z}\right)^2 + \left(\frac{\partial \overline{v}}{\partial z}\right)^2\right]} \tag{2.12}$$

Then approximation of $\frac{\partial \overline{\theta_v}}{\partial z}$, $\frac{\partial \overline{u}}{\partial z}$, and $\frac{\partial \overline{v}}{\partial z}$ by $\frac{\Delta \overline{\theta_v}}{\Delta z}$, $\frac{\Delta \overline{u}}{\Delta z}$, and $\frac{\Delta \overline{v}}{\Delta z}$ respectively, bulk Richardson number is obtained [9],

$$Ri_b = \frac{g}{\overline{\theta_v}} \frac{\Delta \overline{\theta_v} \Delta z}{\left[(\Delta \overline{u})^2 + (\Delta \overline{v})^2\right]} \tag{2.13}$$

The Obukhov length then can be calculated using the approximations [14], for unstable conditions when $Ri_b < 0$,

$$L = \frac{z}{10 Ri_b} \tag{2.14}$$

For stable conditions when $0 < Ri_b < 0.2$,

$$L = \frac{z}{10 Ri_b (1 - 5 Ri_b)} \tag{2.15}$$

Table 2.1: *Classification of stability*

Group	Range of L (m)
Very stable	$0 < L < 200$
Stable	$200 < L < 1000$
Near-neutral	$\lvert L\rvert > 1000$
Unstable	$-1000 < L < -200$
Very unstable	$-200 < L < 0$

For neutral conditions when $Ri_b = 0$,

$$L = \infty \tag{2.16}$$

Wijk distinguished the stability conditions into five different classes according to Obukhov lengths [15], see table 2.1. This classification is applied in this research as well.

Taking stability into consideration, the logarithmical relation can be further developed to diabatic wind profile [9],

$$U(z) = \frac{u_*}{\kappa}\left[\ln\left(\frac{z}{z_0}\right) - \psi\left(\frac{z}{L}\right)\right] \tag{2.17}$$

Where $\psi\left(\frac{z}{L}\right)$ is the stability parameter. According to Dyer [16], under stable conditions when $0 < \mathrm{z}/L \leq 0.5$,

$$-\psi\left(\frac{z}{L}\right) = \frac{4.7\mathrm{z}}{L} \tag{2.18}$$

Under unstable conditions when $\mathrm{z}/L < 0$,

$$-\psi\left(\frac{z}{L}\right) = -2\ln\left[\frac{(1+m)}{2}\right] - \ln\left[\frac{(1+m^2)}{2}\right] + 2\tan^{-1}(m) - \frac{\pi}{2} \tag{2.19}$$

Where $m = [1 - (\beta z/L)]^{1/4}$, Paulson applied the empirical parameter $\beta = 15$ [17].

Equation 2.18 is only applicable under weak stable conditions. Besides, by dimensional analysis, under very unstable conditions, there is $\psi\left(\frac{z}{L}\right) \propto -\left(\frac{z}{L}\right)^{1/3}$. So these two stability parameter equations are not accurate when describing very unstable and very stable conditions. as an alternative, Holtslag's equation is applied to describe the stability parameter under stable conditions [18]. Under stable condition $0 < \mathrm{z}/L \leq 10$,

$$-\psi\left(\frac{z}{L}\right) = a\frac{\mathrm{z}}{L} + \mathrm{b}\left(\frac{\mathrm{z}}{L} - \frac{c}{d}\right)\cdot\exp\left(-d\frac{\mathrm{z}}{L}\right) + \frac{bc}{d} \tag{2.20}$$

Where the coefficients are taken as $a = 1,\ b = \frac{2}{3},\ c = 5,\ d = 0.35$. So the equation becomes,

$$-\psi\left(\frac{z}{L}\right) = \frac{\mathrm{z}}{L} + \frac{2}{3}\left(\frac{\mathrm{z}}{L} - \frac{5}{0.35}\right)\cdot\exp\left(-0.35\frac{\mathrm{z}}{L}\right) + \frac{2}{3}\cdot\frac{5}{0.35} \tag{2.21}$$

Under unstable condition when $z/L < 0$, free convection formulation [19] is applied,

$$-\psi\left(\frac{z}{L}\right) = -\frac{3}{2}\ln\left[\frac{(1+n+n^2)}{3}\right] + \sqrt{3}\tan^{-1}\left(\frac{2n+1}{\sqrt{3}}\right) - \frac{\pi}{\sqrt{3}} \tag{2.22}$$

Where $n = [1-(12z/L)]^{1/3}$. The diabatic wind profile can be compared to the LLJs observed under similar atmospheric stability conditions.

Also, Gryning has shown a more complex wind profile model [19]. He compared the analysis of two measurement test site at Hand Hamburg, and showed that the diabatic wind profiles are only valid up to 50-80 m based on surface-layer theory and Monin-Obukhov scaling. Gryning extended the wind profile model for applied use. The wind profile was formulated for the entire boundary layer [19]. Under neutral conditions,

$$U(z) = \frac{u_*}{\kappa}\left[\ln\left(\frac{z}{z_0}\right) + \frac{z}{L_{MBL}} - \frac{z}{z_i}\left(\frac{z}{2L_{MBL}}\right)\right] \tag{2.23}$$

Under unstable conditions,

$$U(z) = \frac{u_*}{\kappa}\left[\ln\left(\frac{z}{z_0}\right) - \psi\left(\frac{z}{L}\right) + \frac{z}{L_{MBL}} - \frac{z}{z_i}\left(\frac{z}{2L_{MBL}}\right)\right] \tag{2.24}$$

Under stable conditions,

$$U(z) = \frac{u_*}{\kappa}\left[\ln\left(\frac{z}{z_0}\right) - \psi\left(\frac{z}{L}\right)\left(1-\frac{z}{2z_i}\right) + \frac{z}{L_{MBL}} - \frac{z}{z_i}\left(\frac{z}{2L_{MBL}}\right)\right] \tag{2.25}$$

Where L_{MBL} is the middle boundary layer length scale. Though the applicable height is improved compared to diabatic wind prole, the characteristics of LLJs are not included.

2.3 Introduction of LLJs

LLJ is an atmospheric phenomenon in which a wind speed maximum of 10 to 20 m/s [9] occurs close to the surface. It normally forms at night, therefore it is also known as the nocturnal jet. It was first described by Goualt [20] and Farquharson [21] in the 1930s, then after 1950s the theory of LLJs started developing fast. Blackadar stated that LLJs are likely to be better developed at night [22]. He also stated that the wind speed maxima of LLJs in the Great Plains can be supergeostrophic and the wind speed maximum heights are normally corresponding to the nocturnal inversion height. In 1961 a program was conducted in the USA that showed the maximum wind speed height of LLJs are between 300 and 700 m height above the surface and differ from the nocturnal inversion height as stated before [23]. Bonner observed North American LLJs occurring most frequently in the central and eastern US and most frequently occur in summer rather than winter in the Great Plain [24]. Uccellini conducted studies on the LLJs which have been reported in literature and concluded that the pressure gradients is a precondition for the LLJs development [25]. The heights of the maximum wind speed in the LLJs can vary during the night. Baas used 7 year wind speed data at Cabauw to find the characteristics of

LLJs. In his research, LLJs occurred in around 20 % of the nights, and the typical jet heights and jet speeds varied from 140 to 160 m and from 6 to 10 m/s respectively [1].

LLJs are not rare phenomena and are widely observed over the world [9]. For example, North America, South America, Africa, Australia, Asia and Antarctica [24, 26, 27, 28, 29, 30].

The causes of LLJs can be:

1. Baroclinicity over sloping terrain [31, 32];
2. Inertial oscillation [22];
3. Coupling with return circulation in the jet streak [25, 33].

The first two LLJ forcings will be introduced in this report.

2.3.1 Baroclinicity over sloping terrain

Holton mentioned that at sloping terrain, LLJs are responses to the thermal forcing mechanism. This phenomenon results in periodically varied thermal wind related to baroclinicity and LLJ diurnal oscillation [31]. Thermal wind relationship is expressed as below [34],

$$\frac{\partial \mathrm{U}_g}{\partial z} = -\frac{g}{f_c\overline{T}}\frac{\partial \overline{T}}{\partial y} \tag{2.26}$$

$$\frac{\partial \mathrm{V}_g}{\partial z} = \frac{g}{f_c\overline{T}}\frac{\partial \overline{T}}{\partial x} \tag{2.27}$$

Where U_g and V_g are eastward and northward component of geostrophic wind, $\overline{T}$ is average temperature and x , y are Cartesian coordinate towards east and north.

Figure 2.1 shows the mechanism of thermal wind forcings that cause a LLJ diurnal oscillation. Figure (a) and (b) show the daytime situation, while figure (c) and (d) show the nighttime situation. At day time, temperature decreases with height adiabatically from the sun heated ground surface, which causes a negative eastward temperature gradient $\frac{\partial T}{\partial x} < 0$ near the ground surface and aloft. This results in thermal wind $\frac{\partial \mathrm{V}_g}{\partial z} < 0$ at all heights. At the night time, the ground cools down more quickly than the air, which causes a reversion of temperature gradient near the ground surface. As a result, the geostrophic wind shear is also reversed near the surface. At the upper part the temperature gradient keeps the same as at day time. This phenomenon leads to a local maximum wind speed at the lower altitude. However, this reason has strict geographical precondition which is not applicable to offshore meteorological site.

2.3.2 Inertial oscillation

Inertial oscillation is assumed to be the dominant cause of the occurrence of LLJs offshore. At the day time, the winds are subgeostrophic in the mixed layer (ML) due to the strong

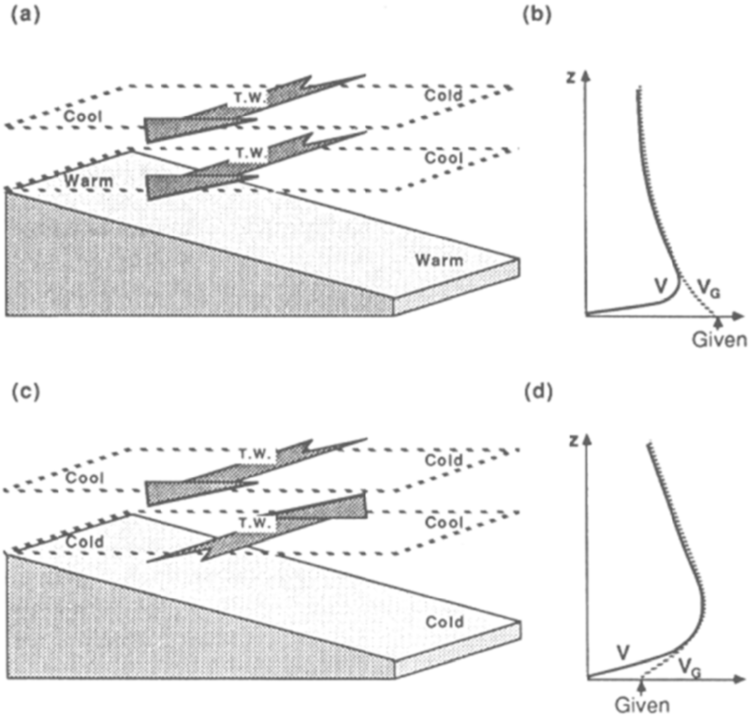

Figure 2.1: *Diurnal oscillation of the low level jet mechanism. Source: [9]*

frictional drag (The mixed layer is a atmospheric zone in which the potential temperature and specific humidity are nearly constant with height). At nightfall, the air layer in contact with the ground surface cools down and becomes stable. The pressure gradients enable the upper layer to accelerate. The influence of the Coriolis force on this phenomenon is to generate an inertial oscillation in the wind, and to make it supergeostrophic after several hours [35].

Consider the momentum equations under dry, horizontally homogeneous and no subsidence environment. In absence of friction.

$$\frac{\partial\left(\overline{U}-\overline{U_g}\right)}{\partial t}=f_c\left(\overline{V}-\overline{V_g}\right) \tag{2.28}$$

$$\frac{\partial\left(\overline{V}-\overline{V_g}\right)}{\partial t}=-f_c\left(\overline{U}-\overline{U_g}\right) \tag{2.29}$$

Differentiate these two equations about time,

$$\frac{\partial^2\left(\overline{U}-\overline{U_g}\right)}{\partial t^2}=f_c\frac{\partial\left(\overline{V}-\overline{V_g}\right)}{\partial t} \tag{2.30}$$

$$\frac{\partial^2\left(\overline{V}-\overline{V_g}\right)}{\partial t^2}=-f_c\frac{\partial\left(\overline{U}-\overline{U_g}\right)}{\partial t} \tag{2.31}$$

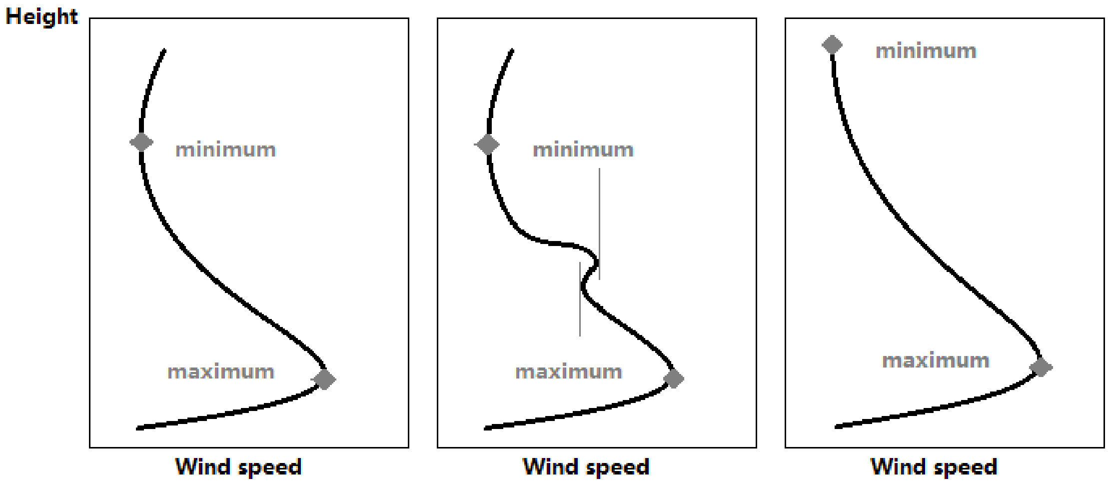

Figure 2.2: *LLJs criteria proposed by Baas*

And then substitute from Equations 2.28 and 2.29,

$$\frac{\partial^2\left(\overline{U}-\overline{U_g}\right)}{\partial t^2} = -{f_c}^2\left(\overline{U}-\overline{U_g}\right) \tag{2.32}$$

$$\frac{\partial^2\left(\overline{V}-\overline{V_g}\right)}{\partial t^2} = -{f_c}^2\left(\overline{V}-\overline{V_g}\right) \tag{2.33}$$

The solution of the two equations above are in the form of:

$$\left(\overline{U}-\overline{U_g}\right) = A\sin\left(f_c t+\alpha\right) \tag{2.34}$$

$$\left(\overline{V}-\overline{V_g}\right) = A\cos\left(f_c t+\alpha\right) \tag{2.35}$$

Where A and α are two parameters. The LLJ oscillation period is 2π/f, which is a function of latitude.

2.4 The criteria of LLJs

In the literature different criteria of LLJs have been applied. Stull defined the LLJ as a situation where the wind speed maximum is at least 2 m/s faster than the wind speed above it within the lowest 1500 m of the atmosphere [9]. Andreas applied a similar definition which is that the maximum is 2 m/s faster than the wind speed minimum above and below [36]. Banta applied Andreas' criteria in his research but used smaller thresholds of 1.5, 1.0 and 0.5 m/s to prevent from excluding too many LLJs [37]. Bonner applied different wind speed thresholds and falloffs to classify LLJs into three types [24], and his definition has been applied by Whiteman [38].

Baas defined LLJs as: 1) the maximum wind speed must be 2 m/s and 25% faster than the next minimum above; 2) If the next minimum increases less than 1 m/s before decreasing again, the minimum should be neglected; 3) If no minimum is present, the lowest wind speed above the maximum is regarded as the minimum. See figure 2.2. Besides, he also defined that only if two neighboring 30 minutes records satisfy the criteria above, a wind profile is classified as a LLJ (hereinafter referred to as “the time criteria”) [1]. These criteria are applied in this research.

Comparing to the other criteria mentioned above, Baas defined LLJs specifically and in more detail. In addition, the time criteria can also help avoiding instantaneous phenomenon which might be incorrectly taken into consideration.

Chapter 3

Site description

In this chapter, the detail of the meteorological site IJmuiden is elaborated. The information regarding the site is taken from the Instrumentation Report of the mast [39]. Besides, the working principle of LiDAR, as an important sensor at the site, is introduced.

3.1 General description

In this research observed data from the meteorology site IJmuiden is used to study LLJs. Figure 3.1 shows the location of IJmuiden. It is located 85 *km* from the coast of IJmuiden, coordinates N52°50.89' E3°26.14'. The water depth is approximately 28 *m*.

The platform at IJmuiden is 18 *m* above Lowest Astronomical Tide (LAT), a container (control room) and a metmast are built on the platform. The metmast top is 92 *m* above LAT. On heights of 25.5 *m*, 57 *m* and 86.5 *m*, booms have been installed on the metmast in three directions, pointing outward from each face of the metmast, see figures 3.2 and 3.3.

Sensors have been installed on the roof of the container and in the metmast to measure wind speed, wind direction, air pressure, air temperature and relative humidity. To minimize the mast influence, the wind cup anemometers, wind vanes, and sonic anemometers have been installed on vertical spigots mounted on the booms. The information regarding sensors in the metmast and on the roof of the container is listed in the table 3.1.

In addition, a LiDAR and a wave bouy have been installed for wind speed, wind direction measurements and wave height and current measurements. The installation height of the LiDAR is 20.88 *m* above LAT. The LiDAR measures the wind speed and wind direction on heights of 59, 90, 115, 140, 165, 190, 215, 240, 265, 290 and 315 m above LAT. The LiDAR type installed at IJmuiden is a Zephir 300. The wind speed and wind direction accuracy is greater than 99.5% according to the Zephir 300 LiDAR specification.

Figure 3.1: Site location [39]

Table 3.1: Sensors installed at the metmast[39]

Sensors	Height	Signal/stored data
Laser precipitation sensor, air pressure sensor, humidity and temperature probe	21 m	Precipitation, temperature, relative humidity, air pressure, air density
Wind cup anemometer, wind vane	27 m	Wind speed, wind direction
Wind cup anemometer, wind vane	58 m	Wind speed, wind direction
Sonic anemometer	85 m	Wind speed
Wind vane	87 m	Wind direction
Air pressure sensor, humidity and temperature probe	90 m	Air pressure, relative humidity, air pressure, air density
Wind cup anemometer	92 m	Wind speed

3.2 LiDAR

LiDAR is a remote sensing technology that measures wind speed by shining a laser to a target area and analyzing the reflected light. Within the observed area, aerosols move along the wind. When the target aerosol moves relative to the laser beam direction, the frequency of the backscatter light shifts because of the Doppler Effect, so the shift is also

Figure 3.2: *The mast and the installation of booms [39]*

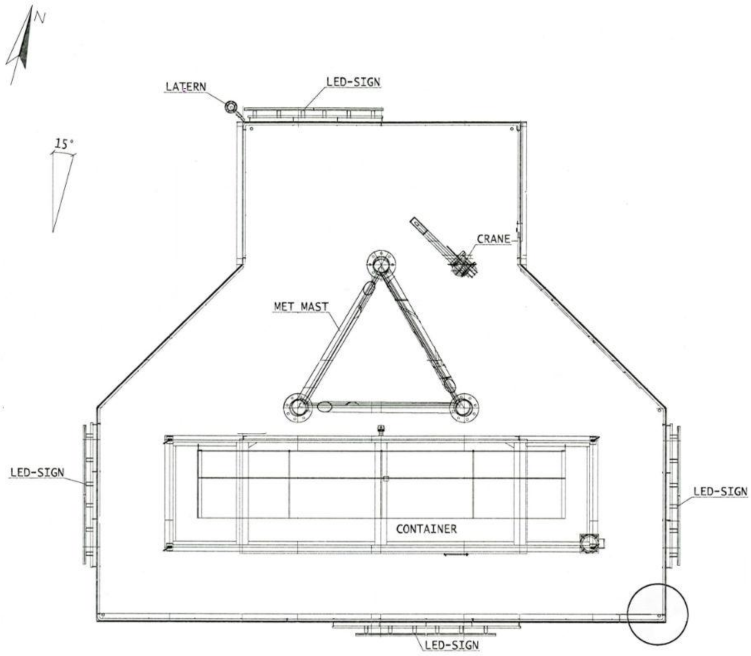

Figure 3.3: *The platform and its orientation [39]*

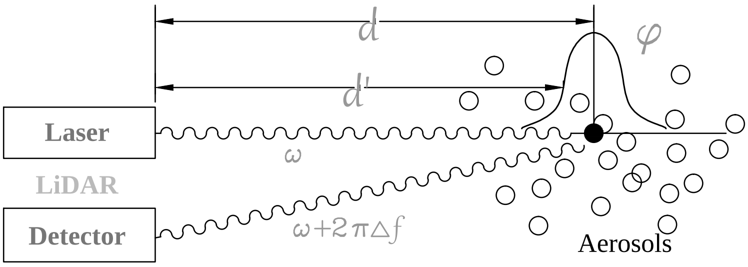

Figure 3.4: LiDAR measurement principle

called the Doppler shift. The principle can be described as [40],

$$v_r = \frac{\lambda_l \Delta f}{2} \tag{3.1}$$

Where v_r is the velocity along beam velocity, λ_l is the laser wavelength, Δf is the Doppler shift.

When LiDAR is focused on a target aerosol at a distance d, all aerosols at distance d' moving along the laser beam path will contribute to the frequency ω_0 of the signal that returns to the LiDAR, and these contributions commonly assumed to be weighted by a function φ. See figure 4.3.

There are two different LiDAR systems, the first one is called Pulsed system and the second one is called Continuous-wave system. They can be distinguished by their transmitted signals. A Pulsed system transmits signal with a series of laser pulses. The pulse rate varies from 10 to 150 kHz. The distance from a LiDAR Pulsed system to the target is calculated from the time to receive the pulse. A Continuous-wave system transmits signal with sinusoidal wave at a known wavelength. The distance from a LiDAR Continuous-wave system to the target is calculated from the number of full waveform together with the phase displacement between transmitted and received signal. The LiDAR system installed at IJmuiden is a continuous-wave LiDAR.

Chapter 4

Data treatment

In this research 10-min wind speed and wind direction data at IJmuiden from 0:00 on 1st Jan 2012 to 23:50 on 31st Dec 2012 are used. The data treatment follows the procedure below.

4.1 Invalid data filtering

Wind data at heights 27, 58, 59, 90, 115, 140, 165, 190, 215, 240, 265, 290 and 315 m are available for the research at IJmuiden. From 27 to 58 m the data is measured by wind cups and wind vanes, and from 59 to 315 m the data is measured by LiDAR. At each 10-minute observation one wind profile is recorded together with air temperature, air pressure, relative humidity and sea surface temperature. The wind profile will only be included for analysis if observation data at all heights is available.

Every 10-minute period data that contains invalid data such as 0, 9999 or NaN are removed. After this process, 43210 out of 52704 10-minute time steps remain.

4.2 Calculation of wind direction/speed

At IJmuiden, the LiDAR is installed with North marker points of 46.5 degrees, see figure 4.1, thus all the wind direction data measured by LiDAR need to be adjusted by 46.5 degrees.

The wind direction/speed data at 27 and 58 m are measured by 3 wind vanes/cups on each height. At each height, one or two wind vanes/cups measure a correct value, while one or two wind vanes/cups are disturbed by mast influence[39]. If we define the three wind direction signal as WD0, WD120, WD240 and the three wind speed signal as WS0, WS120, WS240 according to the wind vanes installed position (see figure 4.1), the rules to find the true wind direction (TWD) and the true wind speed (TWS) can be calculated by

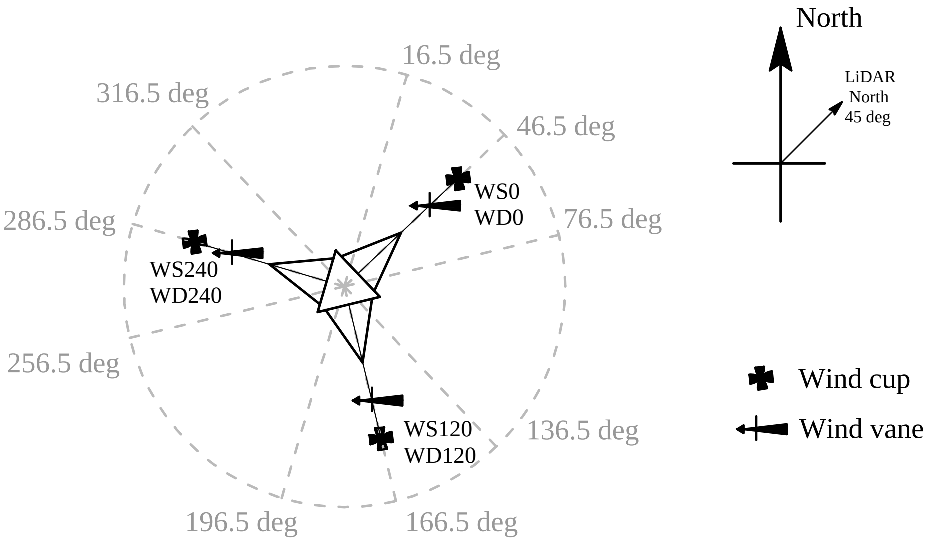

Figure 4.1: *Installation position and orientation of the sensors*

following the Instrumentation Report of the mast IJmuiden. The methodology is shown in figure 4.1 [39].

Pick the middle one (MWD) from three values,

- If MWD is in the range of 16.5 to 76.5 or 196.5 to 256.5, then the TWD is the mean of WD120 and WD240;
- If MWD is in the range of 76.5 to 136.5 or 256.5 to 316.5, then the TWD is the mean of WD0 and WD120;
- If MWD is in any other range, then the TWD is the mean of WD0 and WD240;

After determining the TWD, the TWS can be calculated as follows,

- If TWD is in the range of 46.5 to 166.5, then the TWS is the mean of WS0 and WS120;
- If TWD is in the range of 166.5 to 286.5, then the TWS is the mean of WS120 and WS240;
- If TWD is in any other range, then the TWS is the mean of WS0 and WS240.

This methodology is further examined by plotting the wind speed ratio of each two of the sensors against the TWD at every time steps. The results are shown in figure 4.2. The results verify the validity of the methodology. For instance, when the wind comes from the range of 50 to 150 degree, the ratio of WS0 and WS120 (blue line) shows better performance. There is a maximum and a minimum in the figure when the wind comes from about 110 degree, this is because of the erroneous measurements of WS240 which are caused by the tower shadow (see figure 4.1). Next to these maximum and minimum

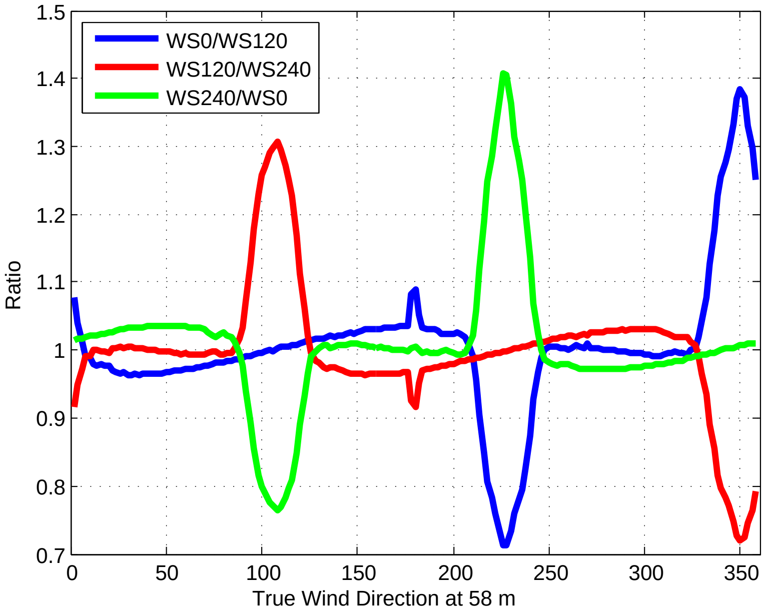

Figure 4.2: *Examination of the methodology. In a specific range of wind direction, two wind vanes measure more accurately and the ratio of these two measurement are close to 1.*

there are smaller ones when the wind comes from about 175 degree, from the figure it can be inferred that the WS120 measurement is disturbed, but this error is not directly shown in figure 4.1.

4.3 LiDAR wind direction data adjustment

Compared to the wind cups and the wind vanes that are installed on the booms outside the main metmast structure (figure 4.1), the LiDAR is less accurate and reliable at IJmuiden because of its installation position, see figure 4.3. The LiDAR is installed at one corner inside the metmast structure, so the measurement of wind speed and wind direction will be disturbed by the mast.

As a verification, data measured by wind cups and wind vanes is assumed to be correct, and it is used as a reference to check the quality of the LiDAR data.

Figure 4.4 shows the wind direction scatter plot at the 'overlapping' height of LiDAR and wind vanes. In the measurement, only 1599 out of 43210 data pairs are with wind direction difference more than 30 deg. Considering these data pairs for further analysis, 1171 out of 1599 data pairs are from the range of 170 to 190 degree. It is known as a common phenomenon of this type of LiDAR that sometimes the direction is estimated oppositely. An adjustment of 180 degree is applied to each time step when this phenomenon occurs. 170 to 190 degree is decided to be the range to apply the adjustment.

Figure 4.5 shows the wind direction scatter plot as a result after the adjustment. It can be seen that after applying the adjustment, there are still some situations with different wind direction remaining. Since it is hard to distinguish these from the random outliers

Figure 4.3: *Top view of LiDAR installation at IJmuiden*

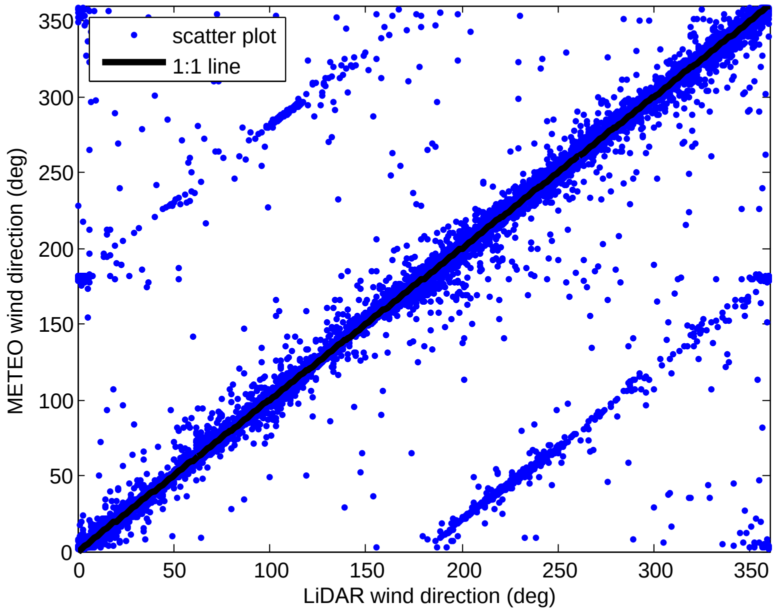

Figure 4.4: *Wind direction scatter plot at 58 m and 59 m*

because the amount of them are very small, these 'residues' should not be arbitrarily adjusted.

4.4 Erroneous data filtering

Normally quality parameters recorded by LiDAR are used to filter erroneous data in research. These parameters are backscatter (a measure of signal strength), CS (an internal

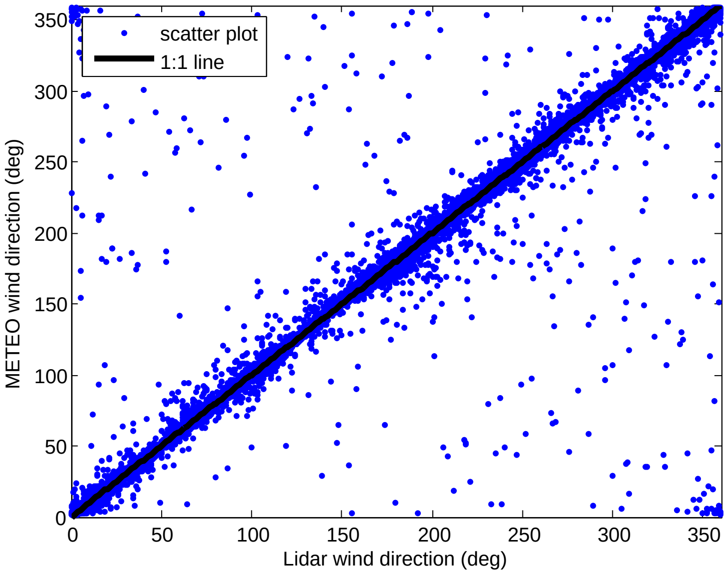

Figure 4.5: *Wind direction scatter plot after the adjustment at 58 m and 59 m*

parameter used for internal quality checking). However, in this research these parameters are not available in the data source. As a substitution, it is assumed that the data at 58 m measured by wind cups and wind vanes should be equal to the data at 59 m measured by LiDAR. Data pairs are marked with different symbols according to the difference value of wind speed, see figure 4.6. According to the assumption that wind cups and wind vanes measure data correctly, data measured by LiDAR which has a big difference to data measured by wind cups and wind vanes can be considered as erroneous data.

It can be seen from the scatter plots (figures 4.6 and 4.7) that if the data pairs show a big difference value in the wind speed scatter plot, the observation also doesn't fit the 1:1 line well in the wind direction scatter plot. Based on these results shown in these two figures, wind profiles with a wind speed difference value (between 58 m and 59 m) bigger than 3 m/s are all filtered. After this process, 43124 out of 52704 wind profiles remain. Figures 4.8 and 4.9 show the wind speed and wind direction scatter plots after this process.

4.5 LiDAR wind speed data adjustment

Wind speed data measured by LiDAR at height 59 m should be equal to data measured by wind cups and wind vanes at height 58 m. For each time step, there are three different simple approaches which can be applied. Expressing the wind speed at height 'X' m as 'WSX' (for example, 'WS58' means wind speed at height 58 m), and expressing the data after adjustment as 'WSXa' (for instance, 'WS58a' means wind speed after adjustment at height 58 m), then the three methods can be described as follows.

- The first method (hereafter referred to as "difference value method") is: Calculating the difference value of these two measurements $ERR1 = WS58 - WS59$ of each

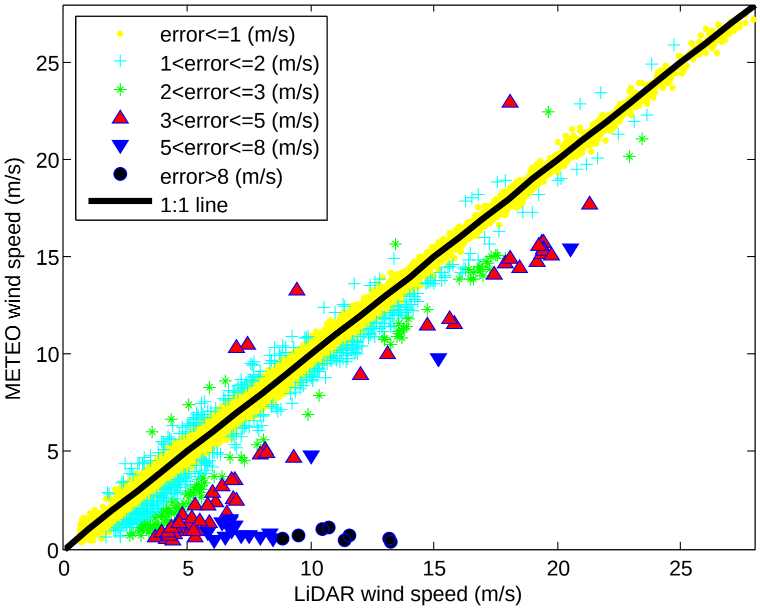

Figure 4.6: *Marked wind speed scatter plot at 58 m and 59 m*

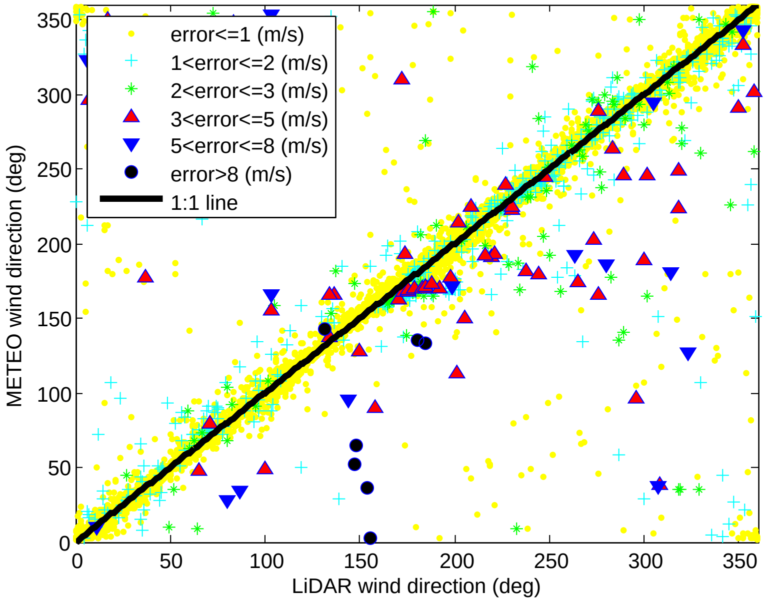

Figure 4.7: *Marked wind direction scatter plot at 58 m and 59 m*

10 min. Then an adjustment is made to wind speed data measured by LiDAR by adding the corresponding difference value: $WS90a = WS90 + ERR1$; $WS115a = WS115 + ERR1$; $WS315a = WS315 + ERR1$. The risk of this method is the possibility of negative wind speed data generation, this would happen when the difference value 'ERR1' is negative and the wind speed above 58 m is low. To prevent this, a large amount of wind profiles with smaller wind speed needs to be

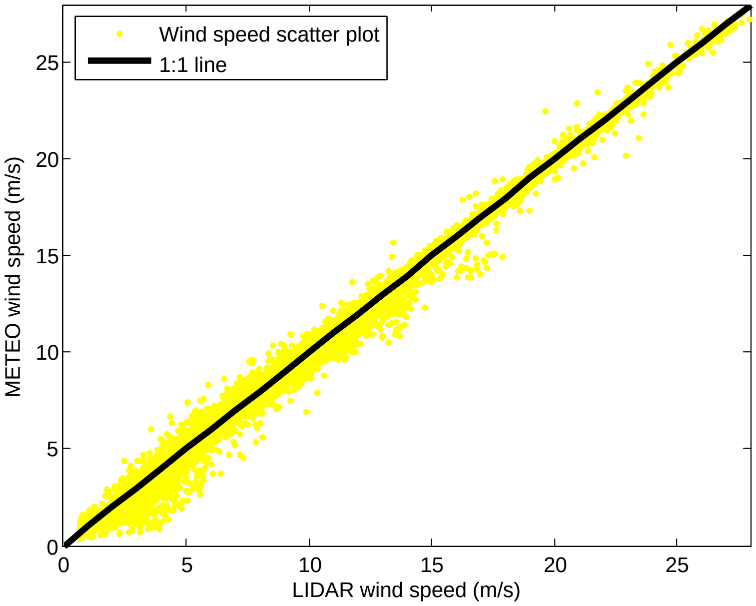

Figure 4.8: *Wind speed scatter plot after filtering at 58 m and 59 m*

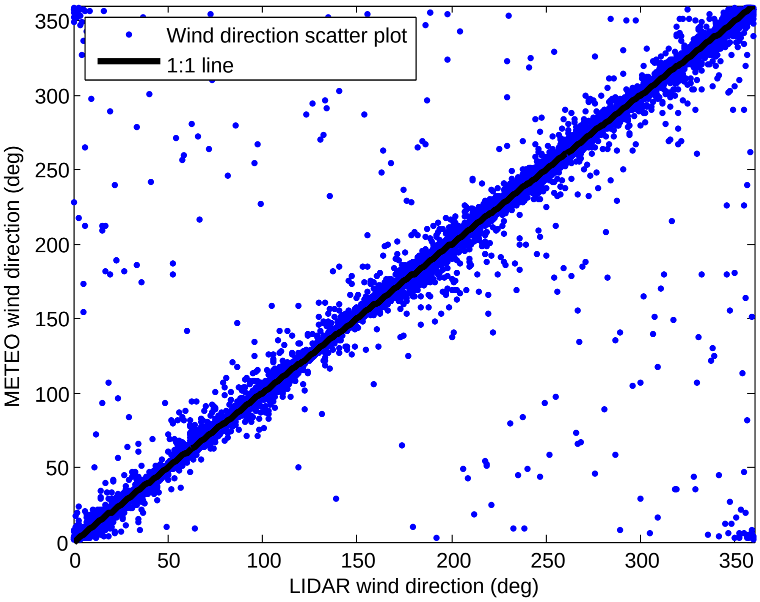

Figure 4.9: *Wind direction scatter plot after filtering at 58 m and 59 m*

filtered in advance, which might change the actual mean wind profile dramatically.

- The second method (hereafter refer to as "ratio method") is: Calculating the ratio of these two measurements $ERR2 = WS58/WS59$ of each 10 min. And then adjusting the LiDAR data by multiplying the LiDAR data by this ratio: $WS90a = WS90 \times ERR2$; $WS115a = WS115 \times ERR2$; $WS315a = WS315 \times ERR2$. This

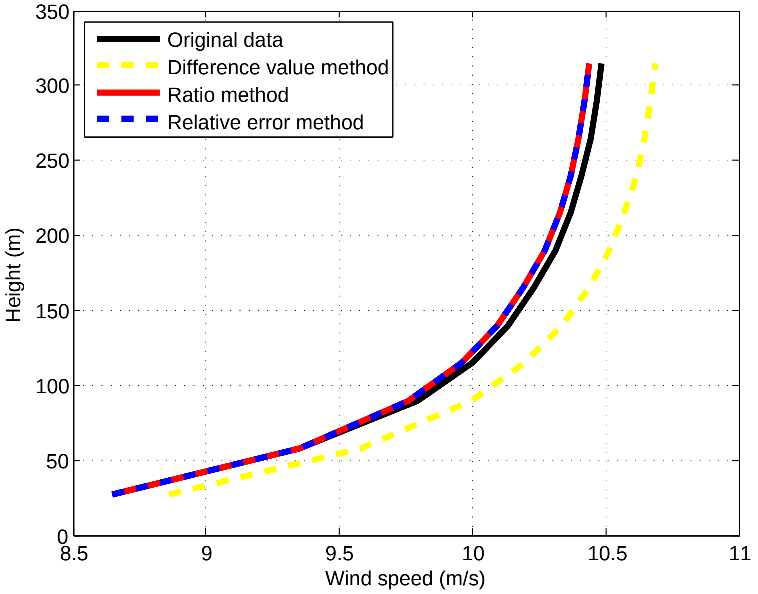

Figure 4.10: *Comparison of three methods*

Table 4.1: *Data filtering*

Statues	Number of wind profiles/time steps
Before filtering	52704
Filtering out invalid data	43210
Filtering out erroneous data	43124

method won't cause negative value, but the disadvantage is for the generally higher wind speed at a higher level, the error will also become bigger when multiplying by the same value.

- The third method (hereafter refer to as "relative error method") is: Calculating the relative error value of each 10 min and adjusting the LiDAR data $ERR3 = (WS58 - WS59)/WS58$. Then applying that $WS90a = WS90/(1 - ERR3)$; $WS115a = WS115/(1 - ERR3)$; $WS315a = WS315/(1 - ERR3)$. It also won't cause any negative speed.

In this research, the mean wind profile after data treatment is expected to be close to its original look. To avoid losing the original property of the data, mean wind profiles after applying the three different adjustment methods mentioned above are plotted with the original mean wind profile in figure 4.10. In this figure ratio method and relative error method show highly consistency with the original mean wind profile. For simplicity, the ratio method is chosen in the research. Table 4.1 shows the overview of filtering processes.

Chapter 5

Observed results

In this chapter, the climate of the site, the observed mean wind profile and the observed mean LLJ are shown. At IJmuiden, most winds come from the Southwest, while most LLJs come from the Northeast. Most of these LLJs are observed under very stable conditions. The occurrence and characteristic of observed LLJs are also analyzed.

5.1 Climate generality

Figure 5.1 shows the wind rose of wind speed and wind direction data in 2012. The winds at IJmuiden mainly come from the south-west sector with high wind speed and almost no wind from south-east and north-east sectors. This might be caused by the North-Atlantic Current that comes from the south-west and goes through the English Channel that drives the wind.

The wind speed distribution and Weibull fit at 90 m are shown in figure 5.2. Weibull distribution plays an important role in wind resource assessment. Weibull parameters k and A, referred to shape parameter and scale parameter respectively, are 10.48 and 2.16 respectively. Table 5.1 shows the mean wind speed and maximum wind speed at each height from 27 to 315 m at IJmuiden, and Weibull parameters for each height are also shown in the table. It can be seen from the table that there is a clear difference of Weibull parameters between wind cups measurement at 27 and 58 m and LiDAR measurement from 90 to 315 m. This might be due to the adjustment process which is done at 58 m high.

The 43124 wind profiles are divided into 12 sectors according to the wind direction at 58 m height (see table 5.3). The mean wind profile of all data and of each sector can be seen at Fig 5.3 . The mean wind profile in sector 3 (45 to 75 deg) is obviously different to typical log wind profile. As is shown later, many LLJs also correspond to this sector.

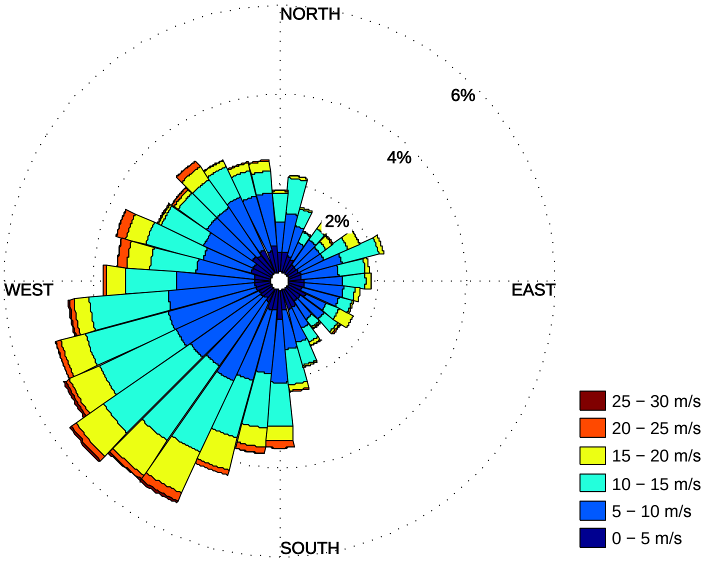

Figure 5.1: *Wind rose map at 90 m height at IJmuiden*

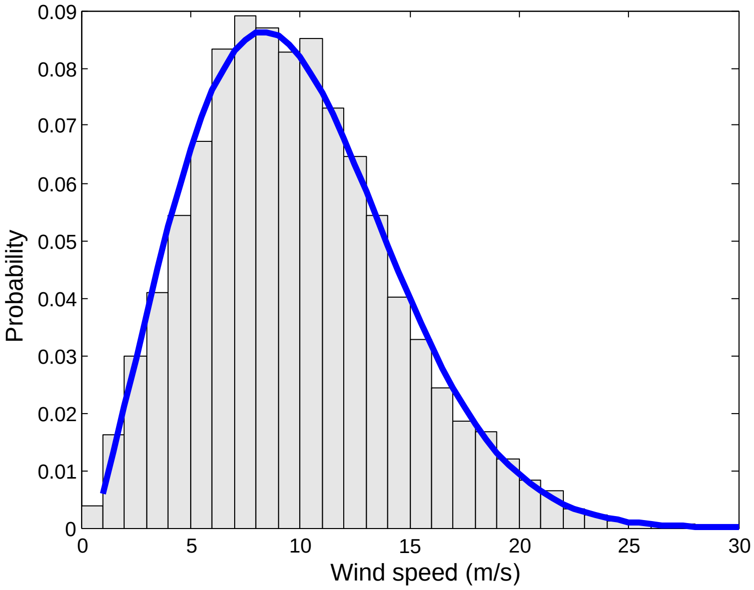

Figure 5.2: *Wind speed Weibull distribution at 90 m level. Weibull parameters: A=10.48, k=2.16*

5.2 Overview of the LLJs observed

In this research LLJs are defined by Baas' definition [1]. A total amount of 448 LLJs are observed at IJmuiden following Baas' criteria. These LLJs belong to 29 days in a

Table 5.1: *Wind speed characteristics at each height*

Height (m)	Mean wind speed (m/s)	Maximum wind speed (m/s)	Shape parameter k	Scale parameter A
27	8.67	25.84	2.09	9.14
58	9.37	27.85	1.95	11.08
90	9.77	29.19	2.16	10.48
115	9.97	30.41	2.13	10.70
140	10.11	32.34	2.09	10.83
165	10.21	33.53	2.05	10.92
190	10.29	34.34	2.02	10.98
215	10.34	34.66	1.99	11.02
240	10.39	35.42	1.97	11.04
265	10.42	35.89	1.96	11.06
290	10.44	36.35	1.95	11.07
315	10.46	36.81	1.95	11.08

Table 5.2: *Sectors and amount of wind profiles*

Sector	Wind direction at 58 m height (deg)	Wind profiles amount
1	345 to 15	2839
2	15 to 45	1739
3	45 to 75	2498
4	75 to 105	2133
5	105 to 135	1965
6	135 to 165	2005
7	165 to 195	4207
8	195 to 225	6304
9	225 to 255	6786
10	255 to 285	2839
11	285 to 315	4967
12	315 to 345	4173

year. If the time criteria is dropped, the amount of LLJs observed increases to 1140 and correspond to 114 days in 2012, which means nearly 1/3 days of the year are observed with LLJs. The mean wind profile of the observed LLJs is plotted in figure 5.4. The black dashed line shows the mean wind profile of LLJs with time criteria, and the red solid line is the mean wind profile of the LLJs without time criteria. It can be seen that after confining the threshold of LLJs duration to 1 hour and 10 minute, the wind speeds at each height reduces but the wind shear above the maximum becomes stronger. The reason that the LLJs become stronger with applying the time criteria might be that the LLJs are time-dependent phenomena, and in time the LLJs strengthen in terms of wind shear.

The amount of wind profiles which have been defined as LLJs in each sector is listed in table 5.3. These LLJs are shown in Appendix A (with time criteria and without time

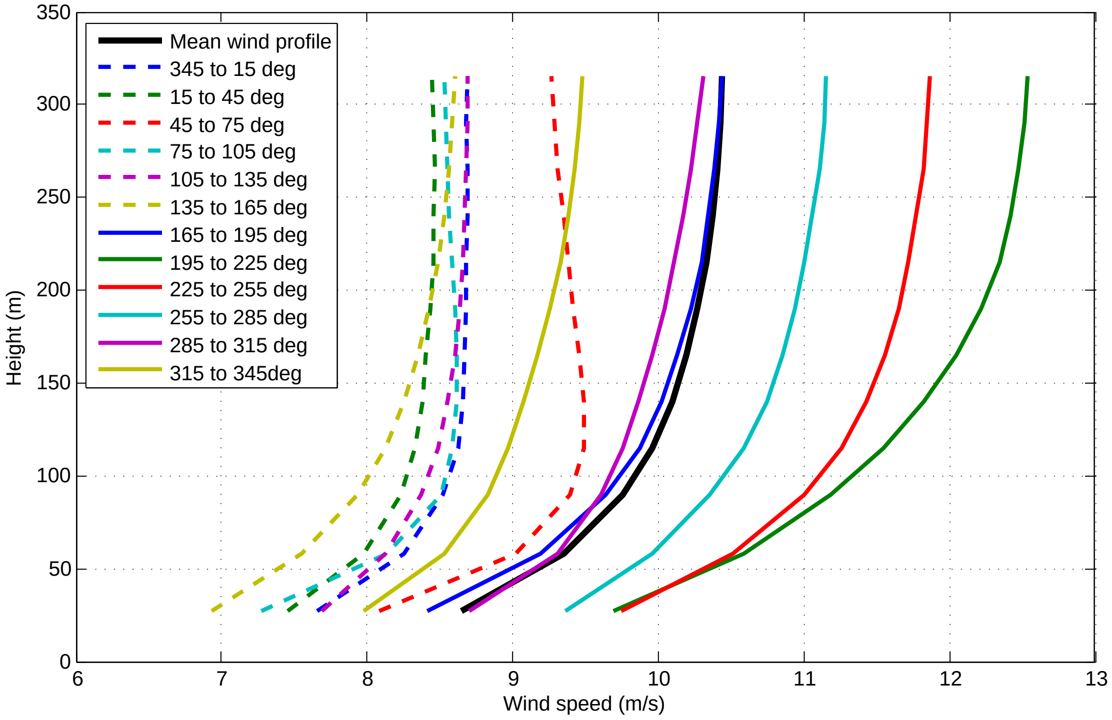

Figure 5.3: *Mean wind profiles for each wind sector at IJmuiden*

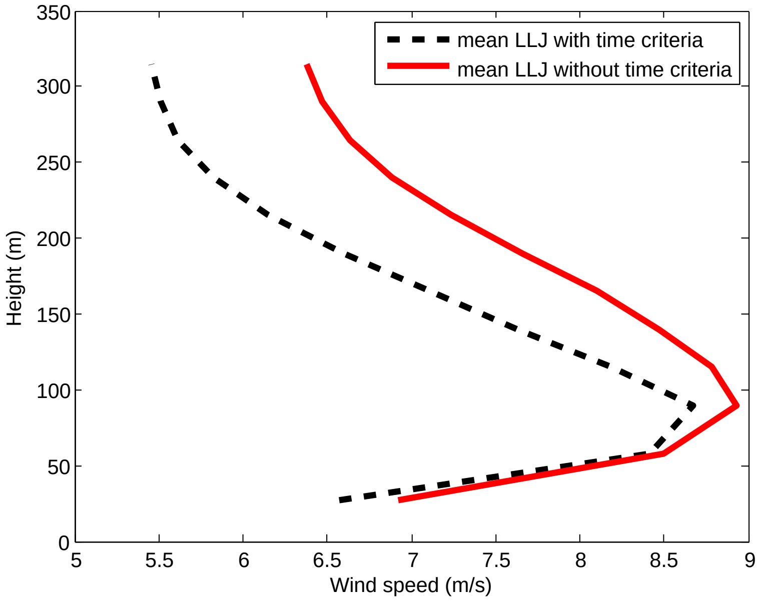

Figure 5.4: *Mean LLJ observed at IJmuiden. Mean LLJ with time criteria and without time criteria are shown seperately*

criteria). The result is that most LLJs come from sector 3, which is consistent with the mean wind profile of sector 3 in figure 5.3 .

Table 5.3: *Sectors and amount of LLJs. Total amount of LLJs is 448 with time criteria, and is 1140 without time criteria*

Sector	Amount of LLJs with time criteria	Amount of LLJs without time criteria
1	15	85
2	41	78
3	178	288
4	91	176
5	3	24
6	8	35
7	20	88
8	24	115
9	50	139
10	1	42
11	9	36
12	8	34

Table 5.4: *Stability and amount of LLJs. Total amount of LLJs is 448 with time criteria, and is 1133 without time criteria*

Stability conditions	Amount of LLJs with time criteria	Amount of LLJs without time criteria
Very stable	410	903
Stable	13	72
Near-neutral	1	11
Unstable	2	25
Very unstable	22	122

5.3 LLJs and stability

By calculating the Obukhov length for each time step, LLJs can be further classified into five groups according to the stability conditions under which the LLJs occur. The classification method is shown in table 2.1. These LLJs are listed in table 5.4 and are plotted in figure 5.5. Without time criteria there are 1140 LLJs, 7 of them are with Richardson number bigger than 0.2, thus the Obukhov length for these 7 LLJs cannot be correctly calculated. Those LLJs are filtered in the stability analysis.

LLJ are expected to occur under (very) stable conditions, and in this research, 423 out of 448 LLJs occur under (very) stable conditions. The LLJs that do not occur under very stable conditions are discussed in more detail. There are 13 wind profiles observed with LLJs under stable condition, 4 of those profiles are continuations (at an earlier or later time step) of the LLJs under very stable conditions. These 4 LLJs can be explained by the generation, development and disappearance of LLJs under fluctuating stability conditions. However, the remaining 9 LLJs are independently generated under stable conditions, this could happen with relatively smaller probability.

The middle two plots in figure 5.5 show the LLJs under near neutral conditions and

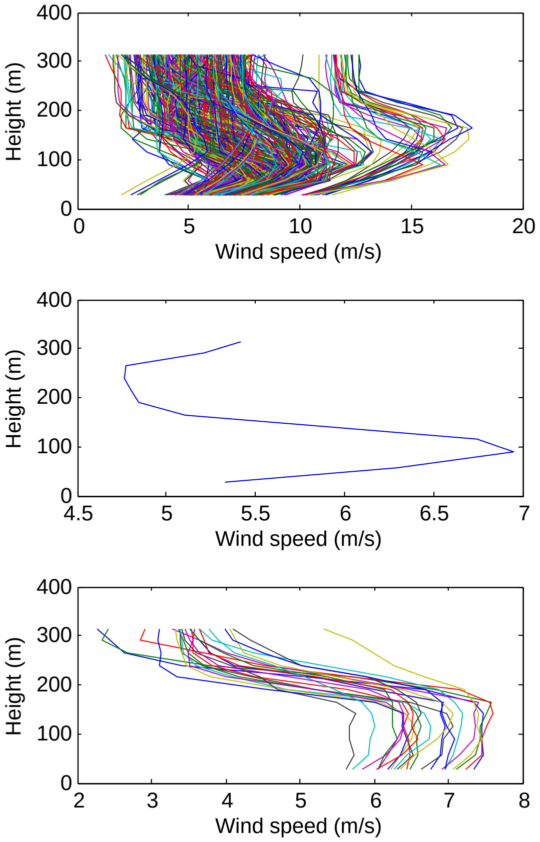

Figure 5.5: *The LLJs observed under different stability conditions. From left to right, from top to bottom are of very stable, stable, near neutral, unstable and very unstable conditions. Larger figures are shown in appendix B*

unstable conditions. These three LLJs were observed at 7th Sep 21:40:00 (near neutral), 7th Sep 21:30:00 (unstable), 9th Sep 03:10:00 (unstable) respectively. The occurrence of these LLJs might be due to an error of the observation data or other phenomenon which influenced the wind speed profile, for instance, the migration of birds. The last plot shows the LLJs under very unstable conditions. They were all continuous and occurred on the 5th Feb from 16:50 to 20:30, and the wind profile of these LLJs do not correspond to typical LLJs profiles. According to the observation, these LLJs were not instantaneous phenomenon, thus the possibility of erroneous measurements is quiet small. These LLJs cannot be explained by the standard theory. Further analysis for these LLJs can be seen below.

The upper two plots in figure 5.6 show the wind speed profiles from 12:00 to 23:00 on 5th Feb, and the next two plots show the wind direction profiles in the same time horizon. These figures show how these LLJs formed, developed and vanished under very unstable conditions. It illustrated that the overall wind speeds slowed down gradually from 12:00 to 23:00. The wind speeds above 150 m slowed down rapidly from 16:00 to 18:00. After 18:00 the shear above 150 m reduced and then at 22:00 these LLJs disappeared. In conformity with the wind direction profile figures, there were also obvious wind direction changes at the higher part of the wind profile from 16:00 to 21:00, which was exactly same time range of the occurrence of LLJs. The reason of the occurrence of this phenomenon is unknown due to the observation and research time limit. Nevertheless, it can be concluded that these LLJs are not typical LLJs because the formation of these LLJs are at the higher part of the profile, while the formation of typical LLJs are at the lower part of the wind profile. Some further information can be seen in the figures 5.7, 5.8 and 5.9.

Figure 5.7 shows the air temperature, relative humidity, air pressure, and air density at 21 and 90 m height from 12:00 to 23:00. Except for the relative humidity, air temperature, air pressure and air density were all in reasonable trends. The relative humidity shows an abnormal curve from 14:00 to 23:00. It decreased sharply from 74%at around 14:00 to a minimum of 61% at around 18:00, and then increased again to a maximum of 71% at around 23:00. The speculation from the trend is that the fluctuating relative humidity was a side effect of the LLJs formation. Figure 5.8 shows the wind speed, wind direction and stability conditions during same time period at 21 and 90 m height. Since the wind shears were above 150 m height, the LLJs cannot be perceived in this figure. However, the atmospheric stability shows a slowly decline in this time period.

The weather conditions in early February are checked on the KNMI website. According to the description (the information below is translated and modified from the description at KNMI website [41]), from the end of January to the middle of February 2012 the temperature was relatively low in the Netherlands, and at 4th February there was a severe drop in the apparent temperature which was caused by the strong easterly winds. The weather at 5th February is shown in figure 5.9, we can see from the figure that the weather in north-western Europe was in a low pressure area in front of the Norwegian coast, and a high pressure area can be seen in front of the Portuguese coast. During the day a local low pressure area developed over the Channel, which moved southwards to southern France and eventually to North-East Spain in the evening. Due to the low pressure area in front of the coast of Norway, the wind in the Netherlands (and at the North Sea) was primarily southerly. This is also found in the LIDAR observation data. Due to the presence of quite cold air over the warm sea, the majority of observations taken in the first few days of February are extremely unstable (with $-30 < L < 0\ m$ most of the time).

5.4 Characteristics of observed LLJs

Several histograms are plotted to show the properties of LLJs observed. LLJs without time criteria are also included for comparison.

The frist two plots in figure 5.10 show the amount of LLJs observed with and without time criteria in each month through a year. The amount of LLJs in March and May is far larger than the other months. To explain this, a stability analysis has been done for each time step in a year. The results are shown in the third plot. It is found that most of the very stable conditions (during which LLJs mostly occur) are in March and May, which is basically coincident with the LLJs observation.

LLJs are expected to occur under stable conditions, which are normally at night onshore. Similarly, a study has been done regarding the time at which LLJs most likely to occur.

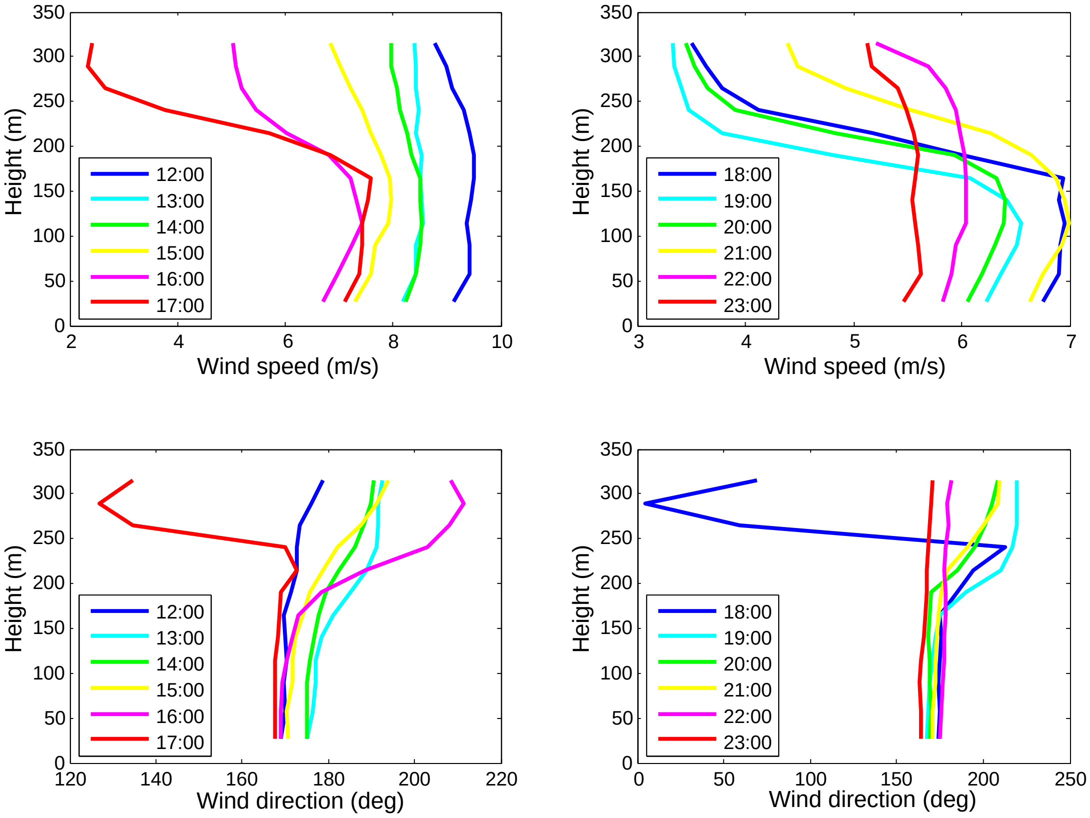

Figure 5.6: *The development and disappearance of LLJs under very stable condition*

In figure 5.11, the amount of LLJs observed with and without time criteria at IJmuiden are distributed into 24 hours according to the occurring time in the first two plots. In addition, a stability analysis has been done for each time step in a year, it shows how many very stable conditions there are per hour in a day in 2012. The results are shown in the last plot. It can be seen from this figure that the peak time of LLJs with time criteria (6 am) is different from the peak time without time criteria (0 am). Furthermore, the very stable conditions are quite equally distributed in each hour in the year. Thus the observed peak time of LLJs can be concluded as a random occurrence.

The duration of LLJs with and without time criteria is shown in figure 5.12. The maximum duration of LLJs with and without time criteria are 1170 min and 1230 min. There is only a single series of LLJs observed with duration longer than 600 min. This LLJs series are excluded in the figure for readability. It can be concluded from the figure that most of the LLJs are observed with duration shorter than 1 hour.

The most important characteristics of LLJs observed are shown in figure 5.13. The first row is the jet height, which is defined as the maximum wind speed height. The second row is the LLJ strength, which in this research is defined as the difference between the maximum wind speed and the next minimum wind speed. And the third row is the LLJ falloff, which in this research is defined as the height difference between the maximum wind speed and the next minimum wind speed. It can be seen from this figure that at IJmuiden, majority of LLJs are observed with jet height less than 100 m, LLJ strength

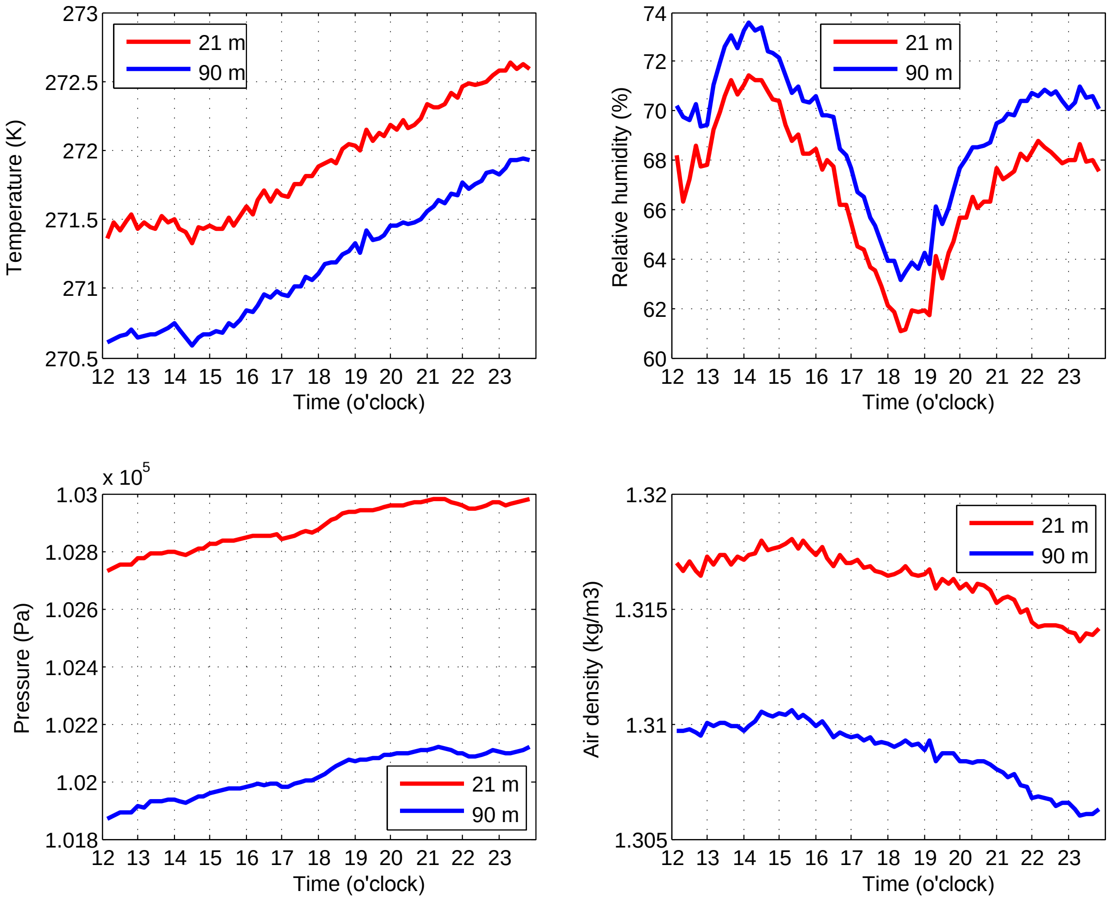

Figure 5.7: *Atmospheric conditions from 12:00 to 23:00 on 5th Feb*

around 3 m/s and LLJ falloff around 200 m. These properties show the importance for wind turbines.

These three properties of each LLJ are tried to match with its corresponding stability condition, but no obvious relation has been found. It can be speculated that the change of the wind speed profile can be large when LLJs are developing since LLJs are time-based phenomena. Besides, the LLJs formation is complicated which is not only related to the stability condition, but also to other conditions like friction velocity, roughness length, etc.

5.5 LLJs and diabatic wind profile

Diabatic wind profiles are plotted together with LLJs in this section. Stability analysis was accomplished for each time step of LLJs occurrence, then the stability parameter was used to calculate the diabatic wind profile in each time step. Hence for every LLJ-moment, one theoretical diabatic wind profile was calculated under exactly the same stability condition with that of the LLJs. Finally the mean wind profile of these theoretical wind profiles is plotted to compare with the mean LLJs profiles.

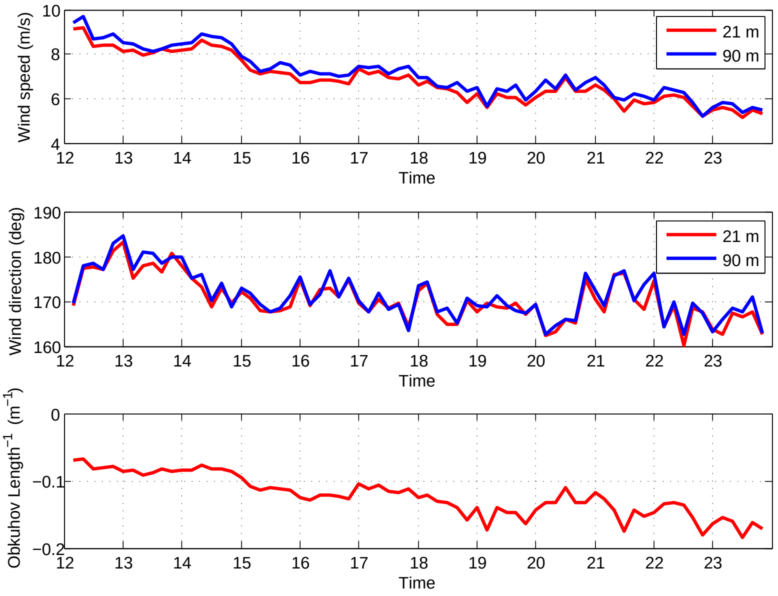

Figure 5.8: *Wind speed, wind direction and stability condition from 12:00 to 23:00 on 5th Feb*

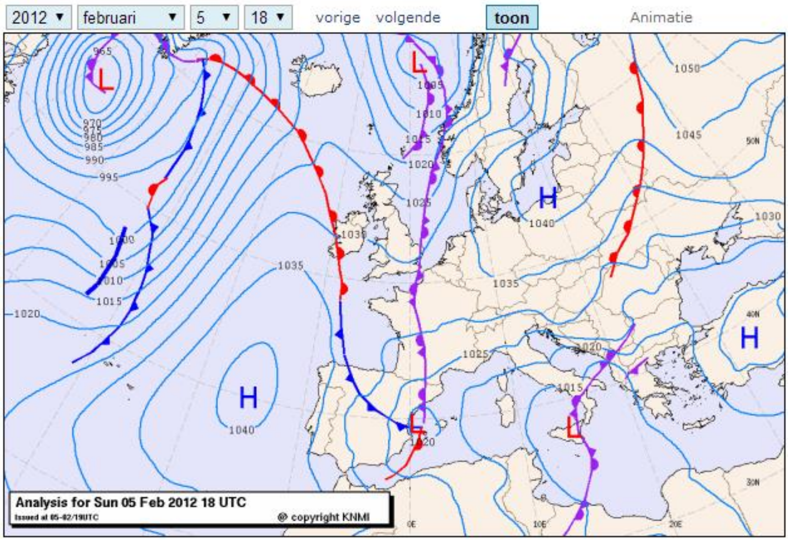

Figure 5.9: *Weather map on 5th Feb[41]*

Figure 5.14 shows the mean observed LLJs profile and theoretical wind profile under stable conditions ($L > 0$). The black solid line is the mean LLJs profile, the blue dashed line is the diabatic wind profile calculated by Equations 2.17 and 2.18, while the green dashed line is the improved diabatic wind profile calculated by Equations 2.17 and **??**. The blue dashed line is very extreme that it is nearly a straight line, this shows that Equation 2.18 is not applicable under very stable conditions. Compared to the blue dashed line, the green dashed line shows a better result, it intersect with the mean LLJ at around 80 m height, below this height, the wind speeds are constantly and slightly bigger than the theoretical wind speeds, and vice versa above 80 m.

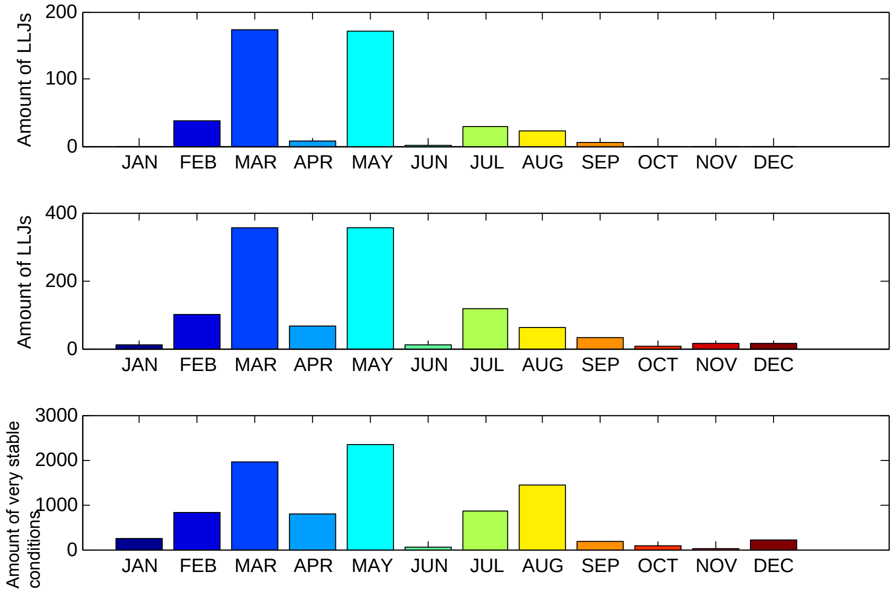

Figure 5.10: *LLJs and very stable condition occurring month in a year. From top to bottom are LLJs observed in each month with time criteria, LLJs observed in each month without time criteria and very stable conditions in each month.*

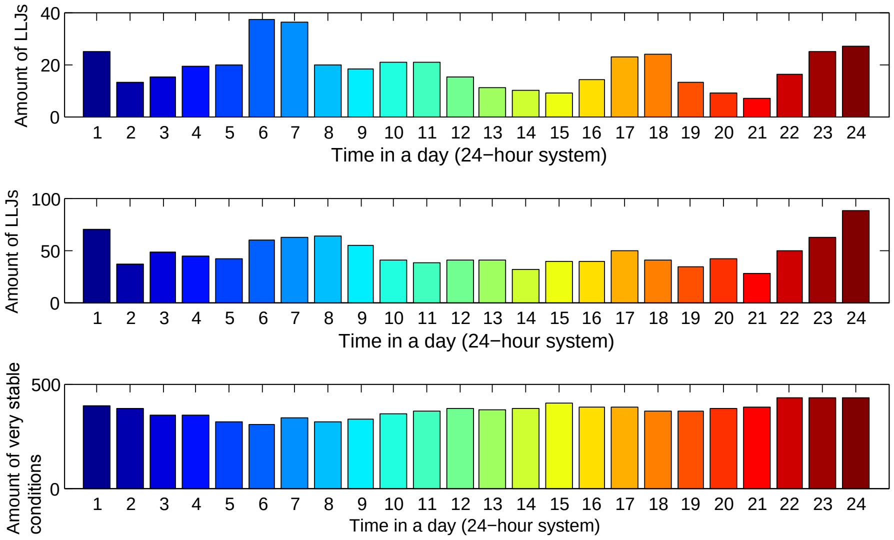

Figure 5.11: *LLJs and very stable condition occurring month in a day. From top to bottom are LLJs observed in a day with time criteria, LLJs observed in a day without time criteria and very stable conditions in a day.*

Figure 5.15 shows the mean observed LLJs profile and theoretical wind profile under unstable conditions ($L < 0$). The black solid line is the mean LLJs profile, the red dashed line is the diabatic wind profile calculated by Equations 2.17 and 2.19, while the pink dashed line is the improved diabatic wind profile calculated by Equations 2.17 and 2.22. Under unstable conditions the difference is small between the two dashed

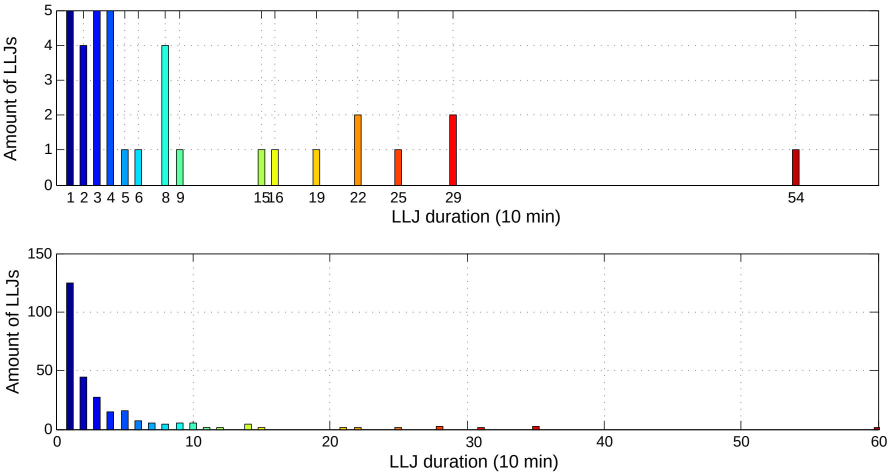

Figure 5.12: LLJs duration with (upper figure) and without (bottom figure) time criteria. The unit of the duration is 10 minutes

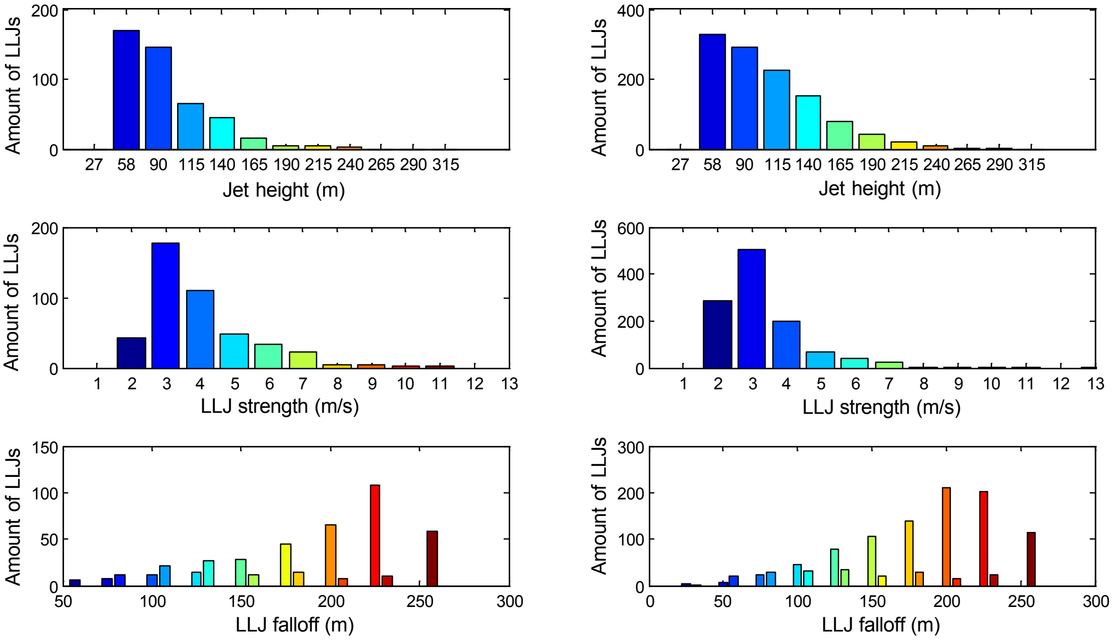

Figure 5.13: LLJs properties. Left three figures are of LLJs with time criteria and right three figures are of LLJs without time criteria, from top to bottom are jet height, LLJs strength and LLJs falloff.

lines, the improved equation results in slightly lower wind speeds than the red dashed line. Below the height of 150 m, the wind speed of LLJs is constantly bigger than the theoretical wind speeds. Above 80 m, the wind speed of the diabatic wind profile increases with height, while the wind speed of the mean LLJs profile decreases with height. So their difference is increasing with height.

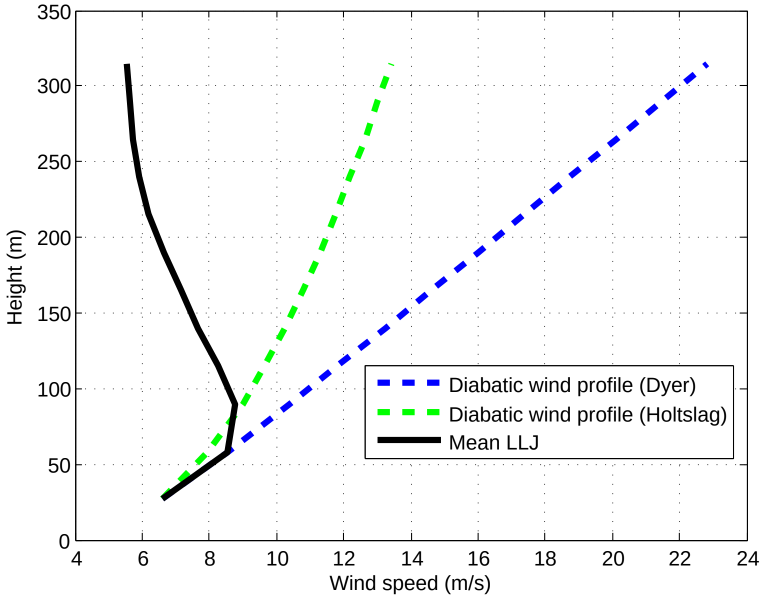

Figure 5.14: *Diabatic wind profile and mean LLJ under stable conditions*

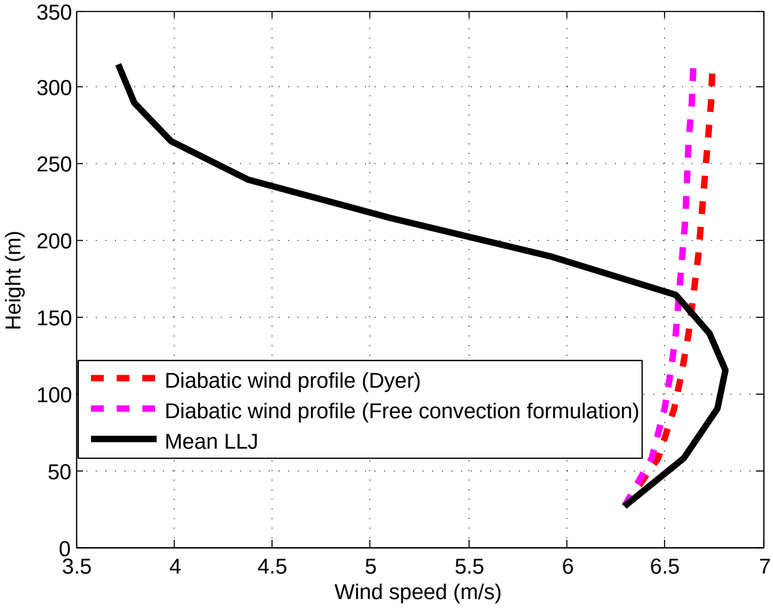

Figure 5.15: *Diabatic wind profile and mean LLJ under unstable conditions*

Chapter 6

A new LLJ model

The existing LLJ models are all time-based, for instance [42] and [43]. They hamper the analysis for engineering use.

In this chapter, a new LLJ model (hereafter referred to as "the LLJ model") is defined based on the the common parameters friction velocity u_*, roughness length z_0, and Obukhov length L. The new model is simple and can be easily applied to load and power analysis and simulations.

6.1 The structure of the model

U_{diff} is introduced to develop the LLJ model, which represents the wind speed difference between the diabatic wind speed $U_{diabatic}$ and LLJs wind speed U_{LLJs} at different height z,

$$U_{LLJs} = U_{diabatic} - U_{diff} \tag{6.1}$$

The new LLJ model can be then regarded as an extension on the diabatic wind profile model,

$$U_{LLJs} = \frac{u_*}{\kappa}\left[\ln\left(\frac{z}{z_0}\right) - \psi\left(\frac{z}{L}\right) - f\left(\frac{z}{z_{int}}\right)\right] \tag{6.2}$$

Where $U_{diff} = \frac{u_*}{\kappa} f\left(\frac{z}{z_{int}}\right)$. The 'intersection height' z_{int} is introduced, which is defined as the height at where U_{diff} becomes zero (see figure 6.1).

The reason to choose the intersection height for nondimensionalizing the height z is that the z_{int} is closely related to L (see next section). Besides, it is one of the important parameters that determines the shape of the LLJs profile. Below this height, the wind turbine gains power and vise versa compared to the diabatic profile, see figure 6.1.

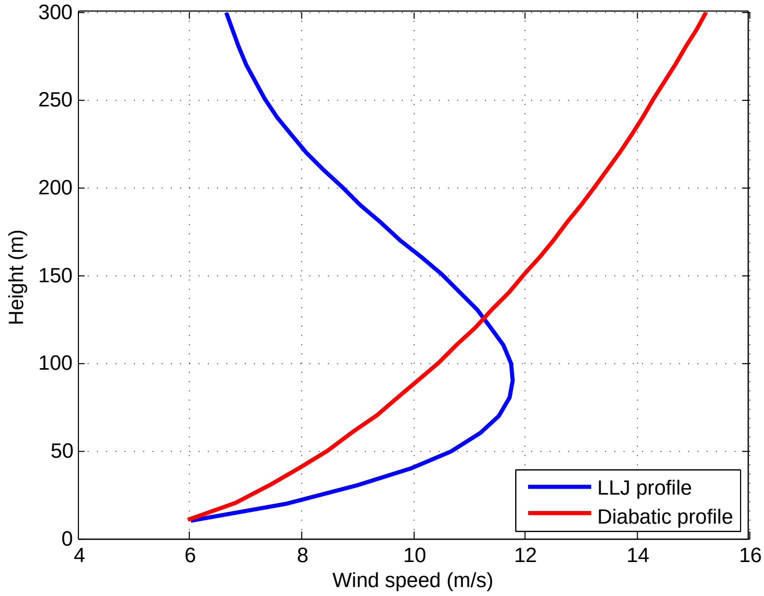

Figure 6.1: *An example of the diabatic wind profile and LLJ wind profile. The height at around 125 m is the intersection height* z_{int}.

6.2 Development of the model

In this section, the equations of z_{int}, U_{diff} , and U_{LLJs} are defined sequentially. The development of the model is based on the observed wind data, and only the time steps under very stable conditions $0 < L \leq 200$ where LLJs mostly occurred are considered.

6.2.1 The equation of z_{int}

Firstly, the LLJs wind speed profiles with time criteria are divided into 6 groups according to the Obukhov length (see table 6.1). After this division, the intersection height z_{int} is calculated for each time step by using an interpolation method. Interpolation method is a mathematical way to add new point within known discrete points according to the estimation of the function. The intersection heights z_{int} are found to be related to Obukhov length L (averaged L of each group), see figure 6.2. The errors are relatively large but there is a clear overall increasing trend in the mean values. The possible explanation is that in the formation and deformation process of LLJs, the change of the wind profile can be great, which will cause remarkable variation of the intersection height.

The overall increasing trend in the mean values can be fitted by the first order polynomial approach (black dashed line in figure 6.2), which is found to be,

$$z_{int} = 0.4L + 68 \tag{6.3}$$

With the equation above, the approximated mean value of intersection height z_{int} can be calculated as a function of Obukhov length L.

Table 6.1: Division of data for defining the equations

Group	Range of L (m)	Amount
1	$L < 20$	91
2	$20 \leq L < 40$	110
3	$40 \leq L < 60$	78
4	$60 \leq L < 80$	42
5	$80 \leq L < 100$	55
6	$100 \leq L < 200$	34

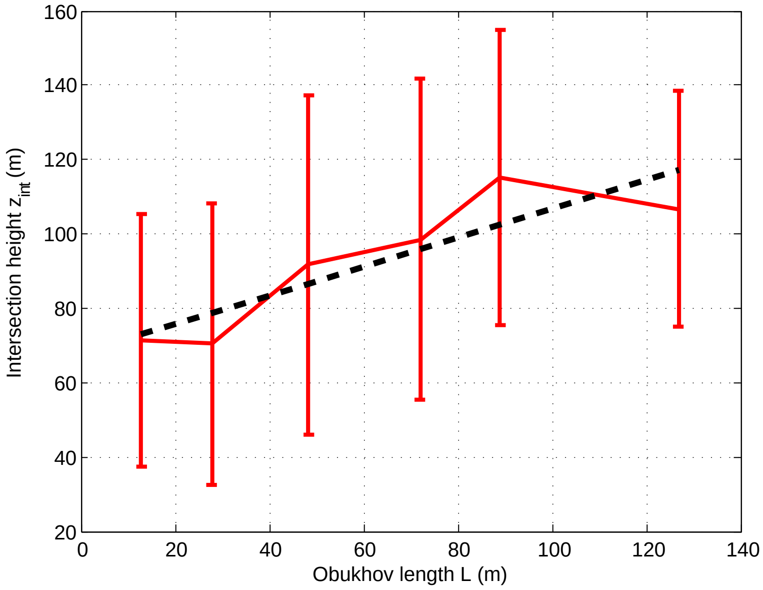

Figure 6.2: *The relation between Obukhov length and intersection height (with time criteria). The red solid lines are the errorbar plot with 'error=standard deviation', and the black dashed line is the fitted line in first order polynomial approach.*

6.2.2 The equation of U_{diff}

The equation $U_{diff} = \frac{u_*}{\kappa} f\left(\frac{z}{z_{int}}\right)$ can be fully defined if a relationship between $\frac{\kappa}{u_*}U_{diff}$ and $\frac{z}{z_{int}}$ could be found. In order to obtain the relationship, for each group the relation between the mean values of $\frac{z}{z_{int}}$ and $\frac{\kappa}{u_*}U_{diff}$ are plotted on the x-axis and y-axis respectively, see figure 6.4. Assuming that there is an equation which can describe all the conditions (different L and u_*), the mean profile is calculated from all groups (black dashed line in figure 6.3) and used to develop the equation. It is found that the fourth order polynomial fits the observed data the best. A small adjustment is applied on the polynomial result to make sure that for $z = z_{int}$, $U_{diff} = 0$. The equation is,

$$U_{diff} = \frac{u_*}{\kappa}\left[0.73\left(\frac{z}{z_{int}}\right)^4 - 7.0\left(\frac{z}{z_{int}}\right)^3 + 22.5\left(\frac{z}{z_{int}}\right)^2 - 20.2\left(\frac{z}{z_{int}}\right) + 3.97\right] \quad (6.4)$$

The examination of Equations 6.3 and 6.4 is done by applying the equations with known

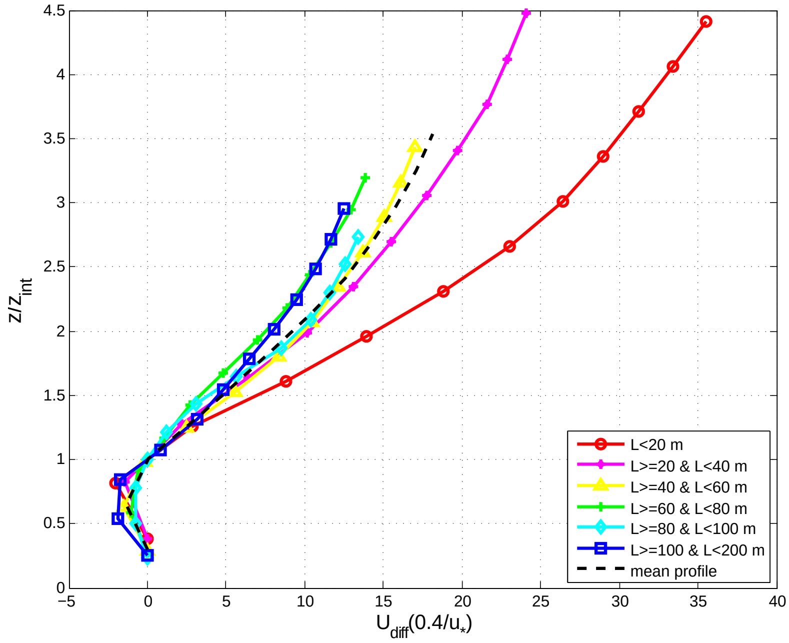

Figure 6.3: *The relationship between* $\frac{\kappa}{u_*}U_{diff}$ *and* $\frac{z}{z_{int}}$.

Table 6.2: *Division of data for examining the equations*

Group	Range of L (m)	mean u_* (m/s)	mean z_0 ($*10^{-5}$ m)	mean L (m)	Amount
1	$L < 10$	0.068	0.715	5.47	25
2	$10 \leq L < 20$	0.127	2.49	15.56	66
3	$20 \leq L < 30$	0.155	3.68	23.89	71
4	$30 \leq L < 40$	0.154	3.64	34.76	39
5	$40 \leq L < 50$	0.165	4.19	44.99	48
6	$50 \leq L < 60$	0.163	4.07	53.43	30
7	$60 \leq L < 70$	0.157	3.77	65.25	14
8	$70 \leq L < 80$	0.201	6.18	75.29	28
9	$80 \leq L < 90$	0.211	6.83	85.32	34
10	$90 \leq L < 100$	0.194	5.78	94.69	21
11	$100 \leq L < 110$	0.154	3.62	104.58	14
12	$L > 110$	0.165	4.17	223.05	33

grouped mean parameters friction velocity u_*, roughness length z_0, and Obukhov length L of LLJs occurring time steps with time criteria (see table 6.1) to calculate the LLJ profile, and then comparing the results with the grouped mean observed LLJs profile. The parameters are devided into 12 groups according to the value of Obukhov length L, see table 6.2.

Equations 6.2, 6.3 and 6.4 are employed to calculate the LLJs wind speed profiles. The results are shown in figures 6.4 and 6.5. Figure 6.4 shows the comparison between the mean LLJs profile calculated by the model and the observed mean LLJs profile. It can be seen that there is an overestimation of wind speed above the jet nose. Below the jet nose the mean profile calculated by equation fits well to the observation profile.

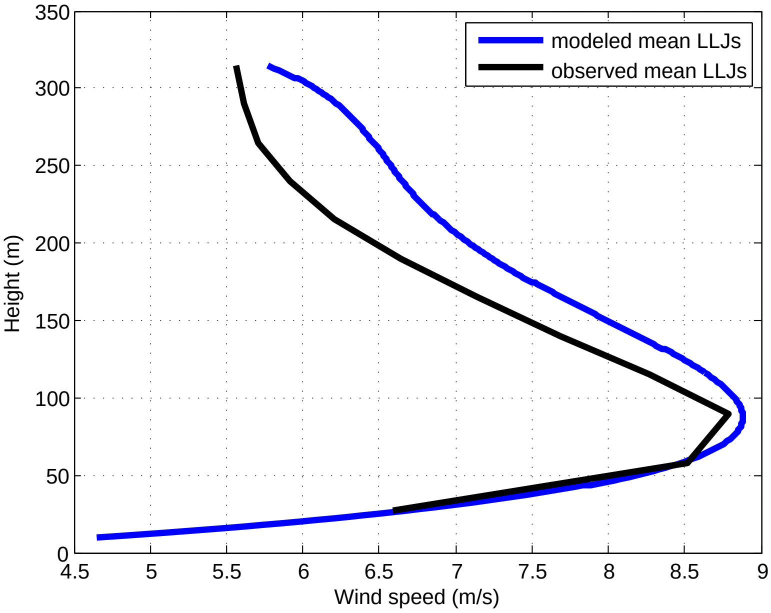

Figure 6.4: *The mean LLJs calculated by the model (blue solid line) and from observation (black solid line). The left figure is of L¡10, and the right figure is of* $L\geq 10$.

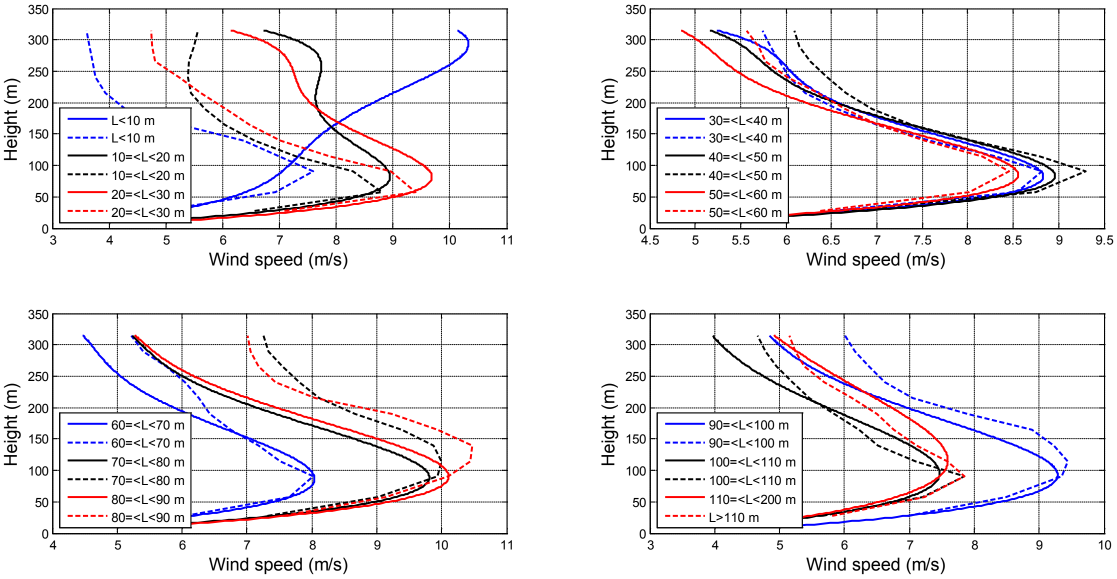

Figure 6.5: *Comparison of modeled and observed LLJs with time criteria. The data is divided into 12 groups with different range of L, where the solid lines represent the modeled results and the dashed lines represent the observed results.*

Figure 6.5 shows the comparison for each group. It can be seen that there is an overestimation of wind speed in the first three groups ($L < 30$) and underestimation in the eighth and ninth groups ($70 \leq L < 90$). Especially when $L < 10$, there are large differences, to look into it more specifically, figure 6.3 is re-plotted with showing $L < 10$, $10 \leq L < 20$, and $20 \leq L < 30$ respectively, see figure 6.6. In addition, a similar figure has been plotted

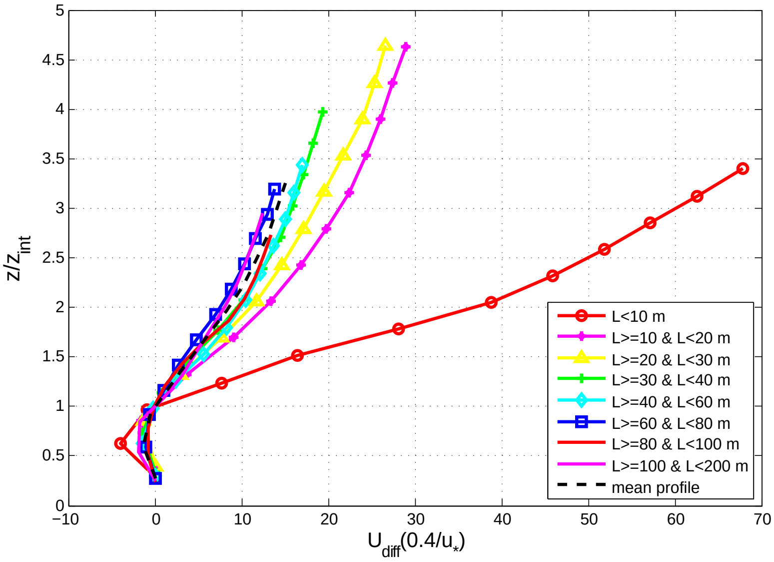

Figure 6.6: *The relationship between* $\frac{\kappa}{u_*}U_{diff}$ *and* $\frac{z}{z_{int}}$ *with time criteria.*

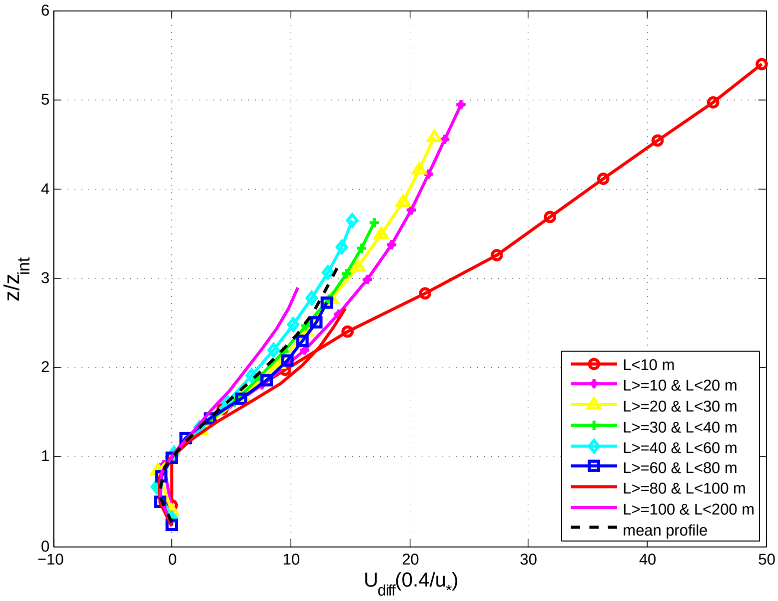

Figure 6.7: *The relationship between* $\frac{\kappa}{u_*}U_{diff}$ *and* $\frac{z}{z_{int}}$ *without time criteria.*

without time criteria for comparison, see figure 6.7.

It can be concluded from figures 6.6 and 6.7 that the condition of $L < 10$ differs significantly from all other stability groups. The superficial reason can be seen in figure 6.6 that equation 6.3 is obtained from the mean profile (black dashed line), which fits better to its neighboring lines. The fundamental reason is that the stability parameter $-\psi\left(\frac{z}{L}\right)$ applied in the diabatic wind profile equation is only applicable in the range of $0 \leq \frac{z}{L} < 10$ [18]. In this research, the height varies from 0 to 315 m. To ensure that the maximum of $\frac{z}{L} = 10$, the maximum Obukhov length L should be 31.5 m.

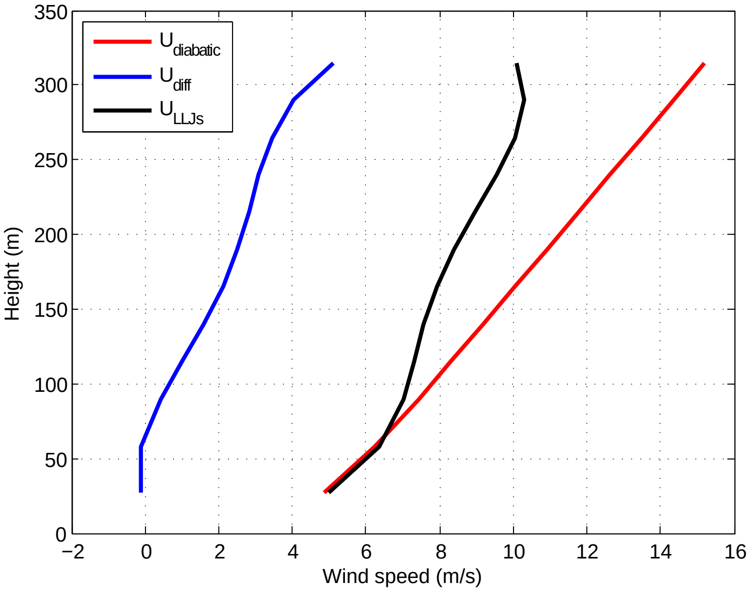

Figure 6.8: *The reason of differences when $L < 10$. The diabatic wind profile is nearly a straight line under extremely stable conditions.*

Especially within the range of $L < 10$, the diabatic wind profile is nearly a straight line (see figure 6.8). At the same time, the LLJs wind profile can be very strong under extremely stable conditions, which results in a huge difference between these two profiles. Moreover, comparing figure 6.6 to figure 6.7, the largest change is found for $L < 10$ than the other lines. It indicates that even though the condition of $L < 10$ is considered as an exception, it is still difficult to define an appropriate equation, so in the following sections, $L < 10$ will be considered separately.

6.2.3 Improvement of the equations

The same process is applied on differently grouped LLJs wind speed profiles to define the equation of LLJs. The new division method can be found in table 6.3, and the condition of $L < 10$ is considered separately. The new equations for U_{diff} are 6.5 and 6.6(adjustments are made to make sure that when $z = z_{int}$, $U_{diff} = 0$.).

For $L < 10$,

$$U_{diff} = \frac{u_*}{\kappa}\left[3.4\left(\frac{z}{z_{int}}\right)^4 - 31.1\left(\frac{z}{z_{int}}\right)^3 + 96.4\left(\frac{z}{z_{int}}\right)^2 - 86.8\left(\frac{z}{z_{int}}\right) + 18.1\right] \tag{6.5}$$

For $L \geq 10$

$$U_{diff} = \frac{u_*}{\kappa}\left[0.7\left(\frac{z}{z_{int}}\right)^4 - 6.7\left(\frac{z}{z_{int}}\right)^3 + 21.4\left(\frac{z}{z_{int}}\right)^2 - 19.1\left(\frac{z}{z_{int}}\right) + 3.7\right] \tag{6.6}$$

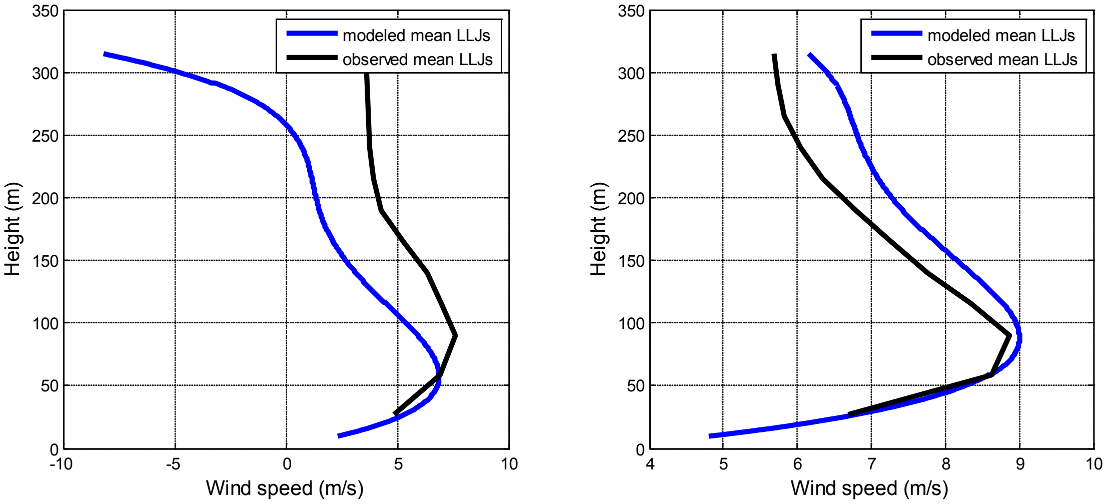

Figure 6.9: *The mean LLJs calculated by the model (blue solid line) and from observation (black solid line)*

Table 6.3: *Division of data for defining the equations*

Group	Range of L (m)	Amount
1	$L < 10$	25
2	$10 \leq L < 20$	66
3	$20 \leq L < 40$	110
4	$40 \leq L < 60$	78
5	$60 \leq L < 80$	42
6	$80 \leq L < 100$	55
7	$100 \leq L < 200$	34

The results can be seen in figures 6.9 and 6.10. Figure 6.9 compares the mean LLJs profile calculated by the two Equations 6.5 and 6.6 to the observed mean LLJs profile. Figure 6.10 shows the comparison for each group. According to Figure 6.6, if the condition of $L < 10$ is considered separately, the two equations should fit very well to the observation. As can be seen from the figure that there are still scatters, the most likely reason is a difference of estimated intersection height. To verify this speculation, diabatic wind profiles are added to the profiles with big scatters (see figure 6.11), and then the figure is compared with the inaccuracy of z_{int} equation(see figure 6.12).

In figure 6.11, we can see that there are overestimations of around 15 and 10 m when $L < 10$ and $20 \leq L < 30$ respectively, and when $70 \leq L < 80$ and $80 \leq L < 90$, there are underestimations of around 30 and 20 m respectively. Figure 6.11 coincides with the solid lines in figure 6.12, which verified that one important reason of the difference between modeled LLJ profile and observed LLJ profile is the calculation of z_{int}. For further verification, group $L < 10$ is shown with and without the correction of z_{int}, see figure 6.13.

After correcting the underestimation of z_{int}, the modeled LLJ matches perfectly with the observed one (figure 6.13). It confirms the importance of the accuracy of calculating z_{int}.

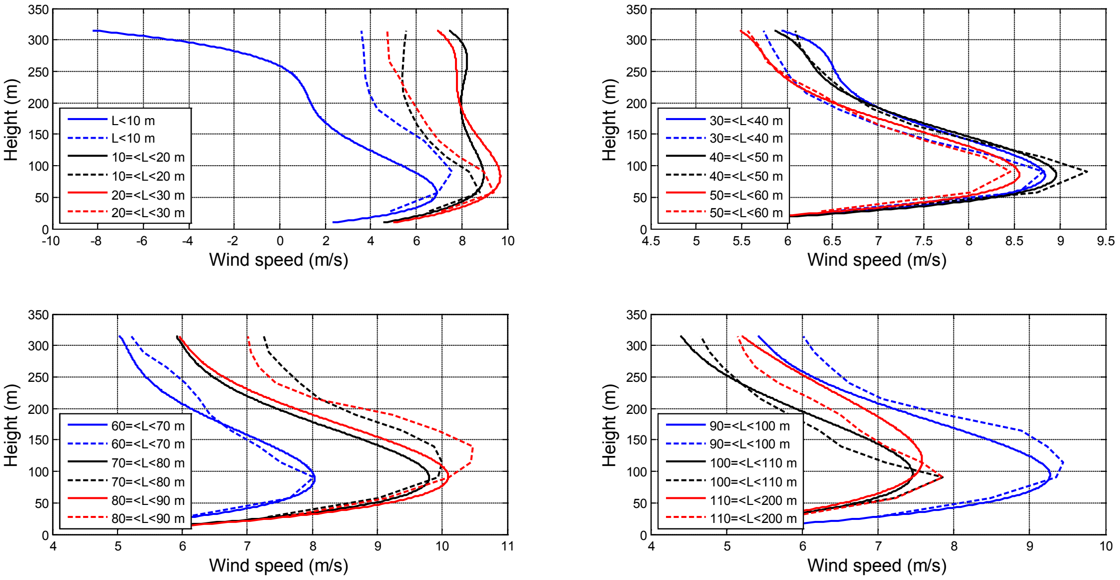

Figure 6.10: *Comparison of modeled and observed LLJs with time criteria(improved model). The data is divided into 12 groups with different range of L, where the solid lines represent the modeled results and the dashed lines represent the observed results.*

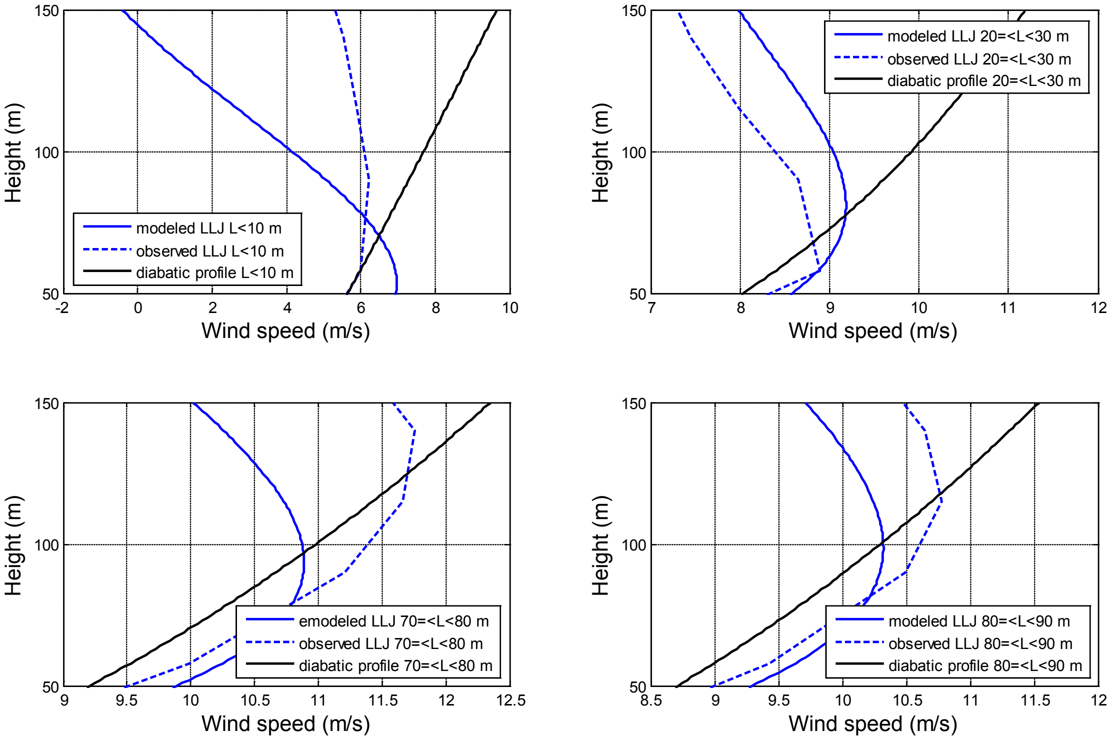

Figure 6.11: *Overestimation and underestimation of z_{int} as the reason of scatter*

Referred to the blue dashed line in figure 6.12, there is an overestimation of z_{int} without time criteria which is opposite to the situation with time criteria, and in the range of

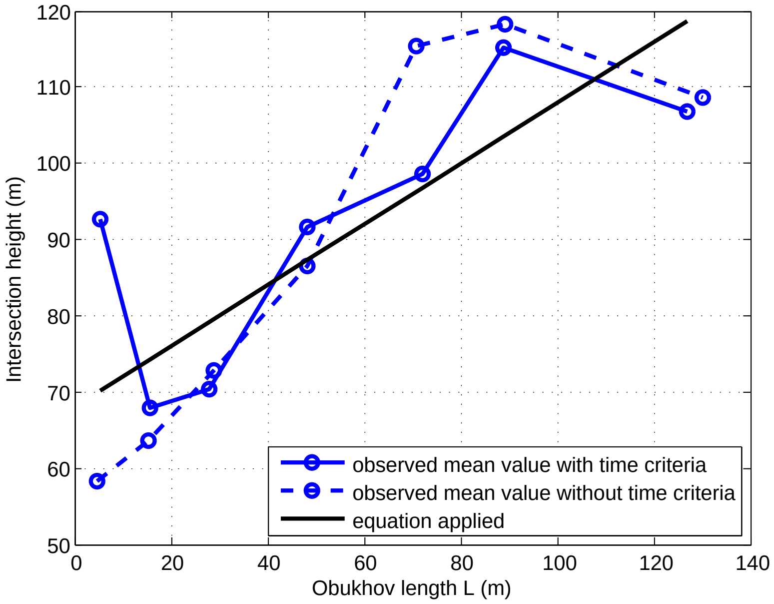

Figure 6.12: *The comparison between observed* z_{int}*(both with and without time criteria) and calculated* z_{int}

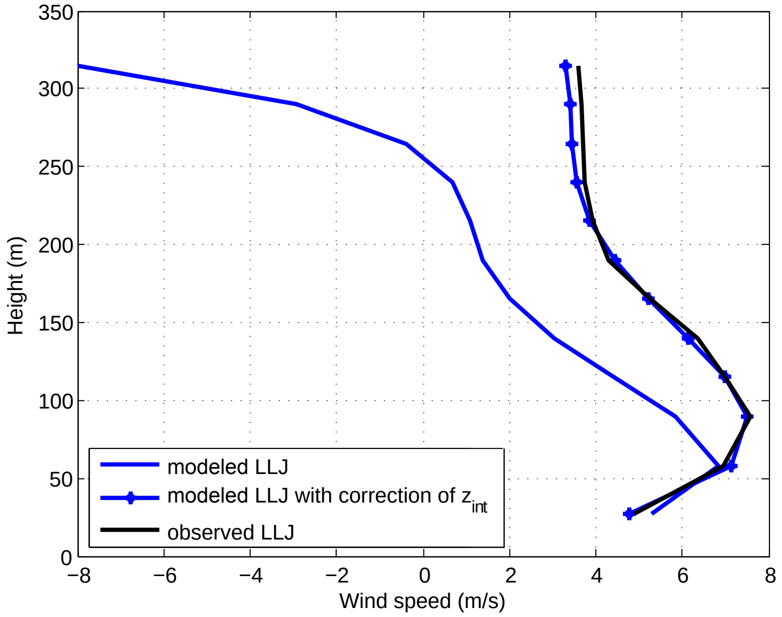

Figure 6.13: *The correction of* z_{int} *(*$L < 10$*). The blue solid line with stars shows the results with an correction of 22.5 m underestimation, where* $z_{int} = 0.4L + 68 + 22.5m$

$L < 100$ the trend is quite linear, which implies that an correction of z_{int} might not be proper. Since the equation of U_{diff} under the condition of $L < 10$ is developed from the observed LLJs profile with the observed intersection height, as a compromise, a correction

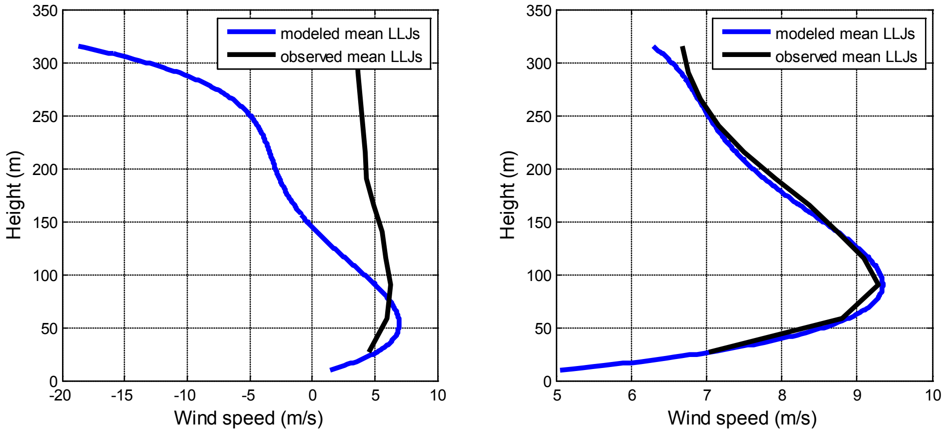

Figure 6.14: *The mean LLJs calculated by the model (blue solid line) and from observation (black solid line) without time criteria. The left figure is of L¡10, and the right figure is of L*≥ 10.

is made for z_{int} when $L < 10$,

$$z_{int,L<10} = 0.4L + 90 \tag{6.7}$$

It can be seen from figure 6.12 that there is a decrease of intersection height in the range of $L > 100$. There are two possible reasons, the first one is that there is an upper observation limit of 315 m in this research, which may also confine the maximum value of intersection height; the second one is that there are less LLJs observed when $100 \leq L < 200$ with time criteria (see table 6.3), thus within this range the result shown in the figure is unconvincing. As a compromise, the adjustment in the intersection height equation is only applied for $L < 10$ (Equation 6.7).

6.2.4 Discussion and summary

In the process of developing the LLJ model, LLJs profiles with time criteria are used because they are more typical. There is a more clear order of the lines in the figure with time criteria (figure 6.6 comparing to the figure without time criteria (figure 6.7).

For engineering use, all LLJs need to be included. Because even untypical LLJs can influence the power production and the load cases. Thus the equations are applied to parameters friction velocity u_*, roughness length z_0, and Obukhov length L of LLJs occurring time steps without time criteria. The process is similar to the previous one, so only results are shown, see below.

It can be seen from figure 6.14 that the LLJ model are unreliable under extremely stable condition $L < 10$. And when $L > 10$, the two LLJs profiles match very well. Moreover, In Chapter 7 this model will be applied to do wind turbine power production analysis and simulations. In accordance with figure 6.14, the modeled profile is quiet accurate to be applied. The detailed results can be seen in figure 6.15. The scatter as discussed above is mostly caused by the inaccurately estimated intersection height z_{int}, especially when the value of L is around 80, there is a severe underestimation of the intersection height (see figure 6.3).

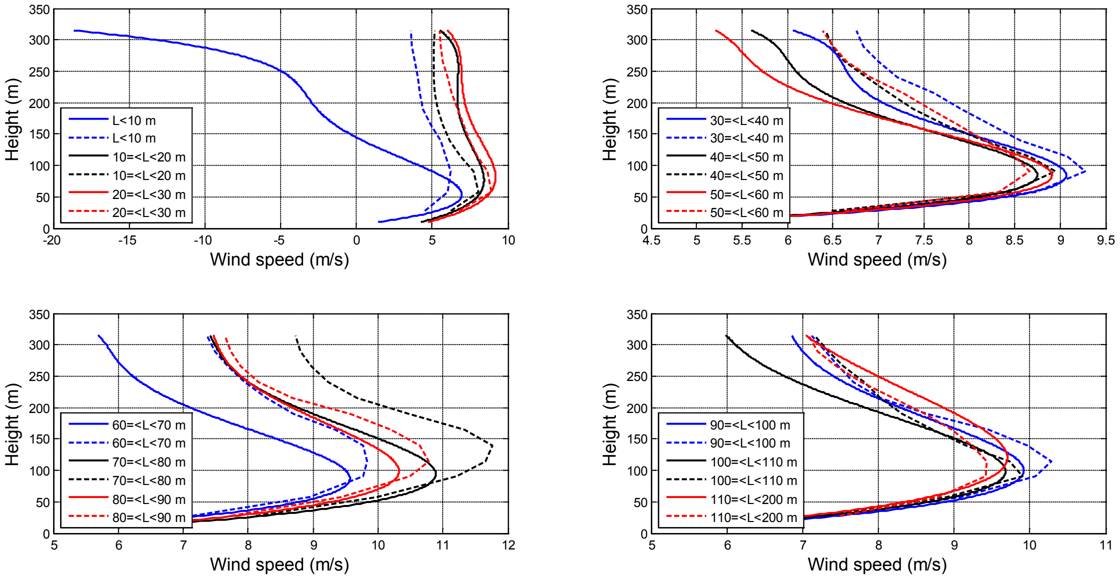

Figure 6.15: *Comparison of modeled and observed LLJs without time criteria (improved model). The data is divided into 12 groups with different range of L, where the solid lines represent the modeled results and the dashed lines represent the observed results.*

As a summary, under stable conditions ($L \geq 10$), the process of calculating a LLJ profile is (The extremely stable condition is not included here):

(1) Calculate z_{int} by $z_{int} = 0.4L + 68$;

(2) Calculate U_{diff} by $U_{diff} = \frac{u_*}{\kappa}\left[0.7\left(\frac{z}{z_{int}}\right)^4 - 6.7\left(\frac{z}{z_{int}}\right)^3 + 21.4\left(\frac{z}{z_{int}}\right)^2 - 19.1\left(\frac{z}{z_{int}}\right) + 3.7\right]$

(3) Calculate stability parameter $-\psi\left(\frac{z}{L}\right)$ by $-\psi\left(\frac{z}{L}\right) = \frac{z}{L} + \frac{2}{3}\left(\frac{z}{L} - \frac{5}{0.35}\right)e^{-0.35\frac{z}{L}} + \frac{2}{3}\frac{5}{0.35}$

(4) Calculate $U_{diabatic}$ by $U_{diabatic} = \frac{u_*}{\kappa}\left[\ln\left(\frac{z}{z_0}\right) - \psi\left(\frac{z}{L}\right)\right]$,

(5) Calculate U_{LLJs} by $U_{LLJs} = U_{diabatic} - U_{diff}$

6.3 Sensitivity analysis

A sensitivity analysis is done to show how the parameters in the LLJ model influence the modeled result. The baseline of the sensitivity analysis is: $L = 100\ m$; $z0 = 0.0002\ m$; $ustar = 0.36\ m/s$. The constants in the analysis are the heights $z = 10 : 10 : 300\ m$ and $\kappa = 0.4$. The results are shown in figures 6.16, 6.17 and 6.18.

Figures 6.16, 6.17 and 6.18 show how the variances of Obukhov length L, friction velocity u_* and roughness length z_0 influence the results calculated by the LLJ model respectively.

- When Obukhov length L is increasing (which means the atmospheric stability is decreasing), the jet speed is decreasing slightly and the jet height is increasing slightly.

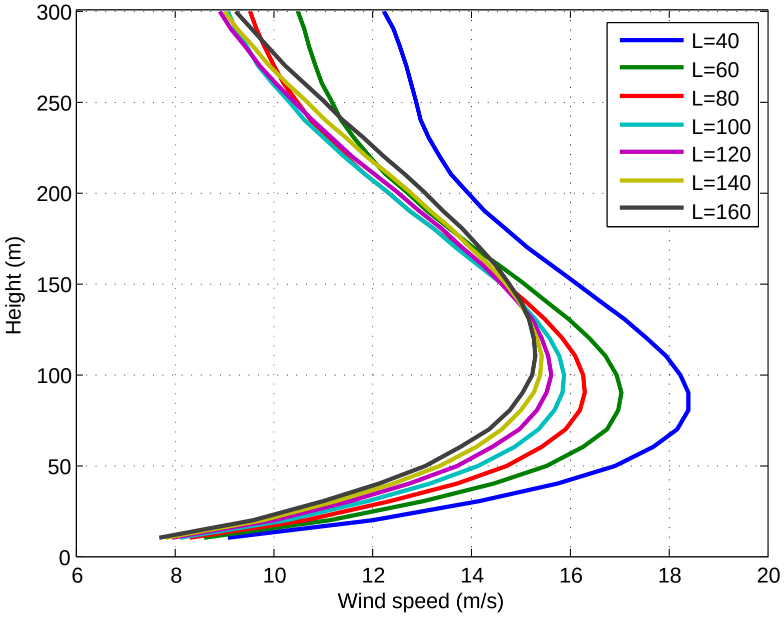

Figure 6.16: *The variance of the modeled LLJs profile as a function of Obukhov length L* (z_0=0.0002, u_*=0.36)

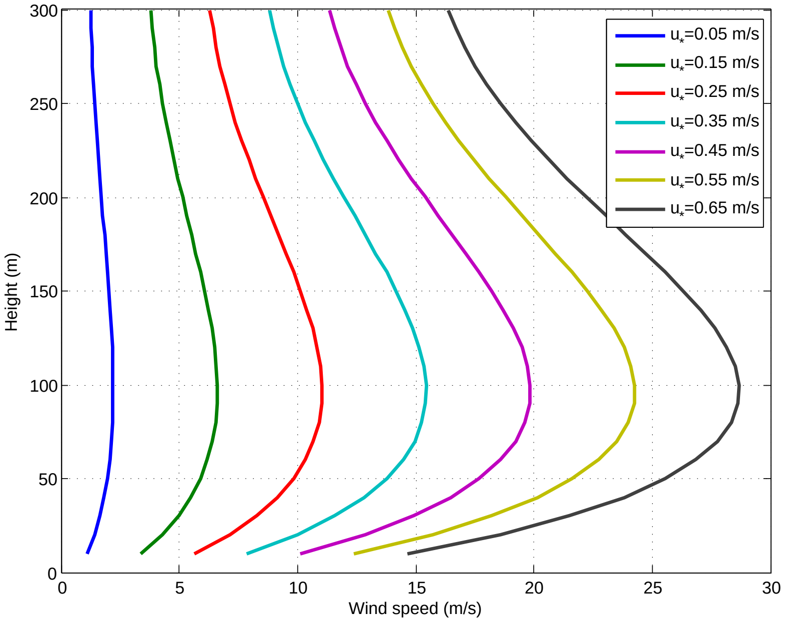

Figure 6.17: *The variance of the modeled LLJs profile as a function of friction velocity* u_* (z_0=0.0002, L=100)

- When friction velocity u_* is increasing, the jet speed is increasing severely, and the wind shear is increasing.

- When roughness length z_0 is increasing (which reflects the increasing frictional force

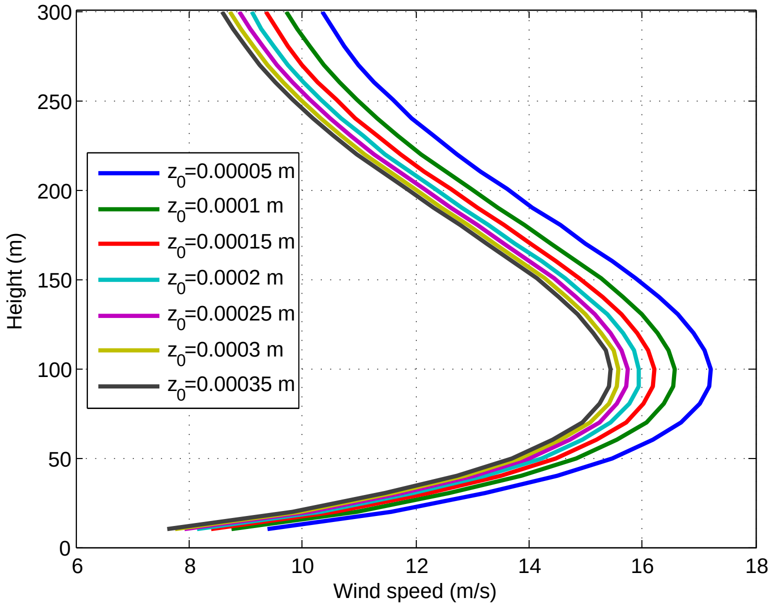

Figure 6.18: *The variance of the modeled LLJs profile as a function of roughness length* z_0 *(*u_**=0.36, L=100)*

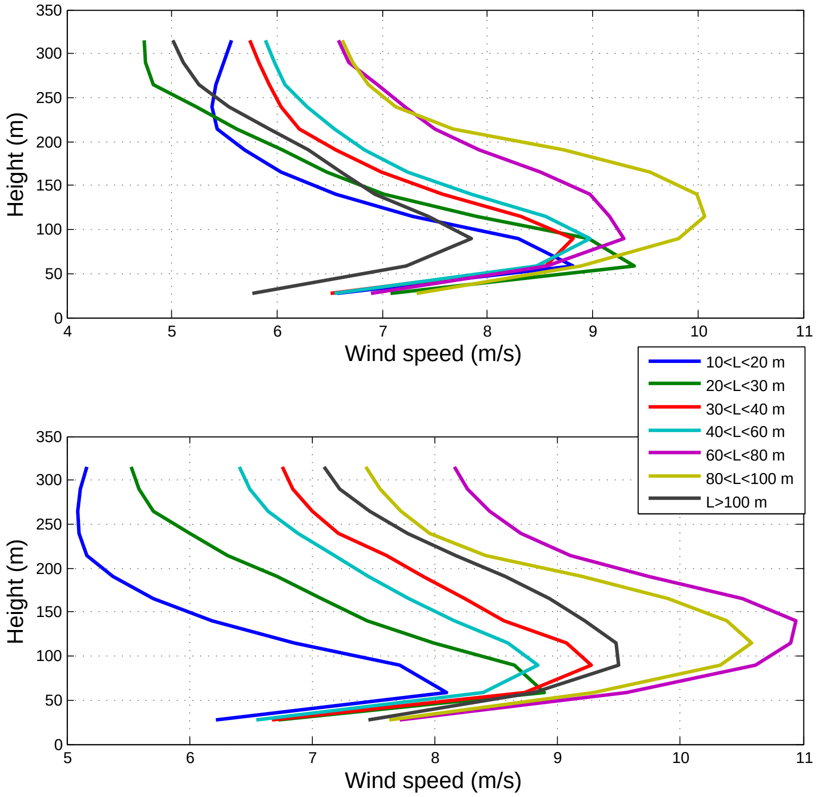

Figure 6.19: *The observed influence of L with (top) and without (bottom) time criteria*

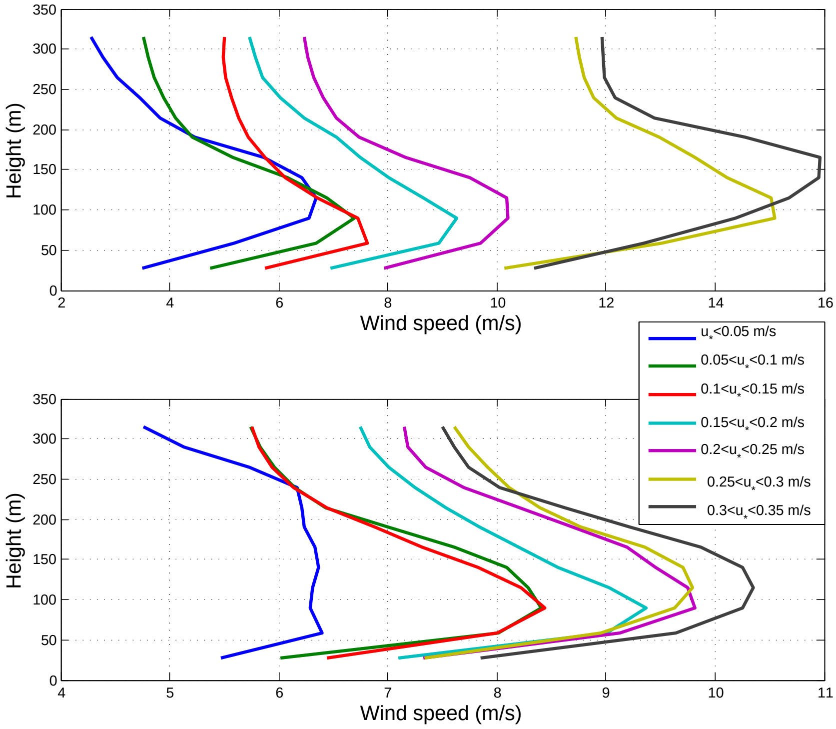

Figure 6.20: *The observed influence of u_* with (top) and without (bottom) time criteria*

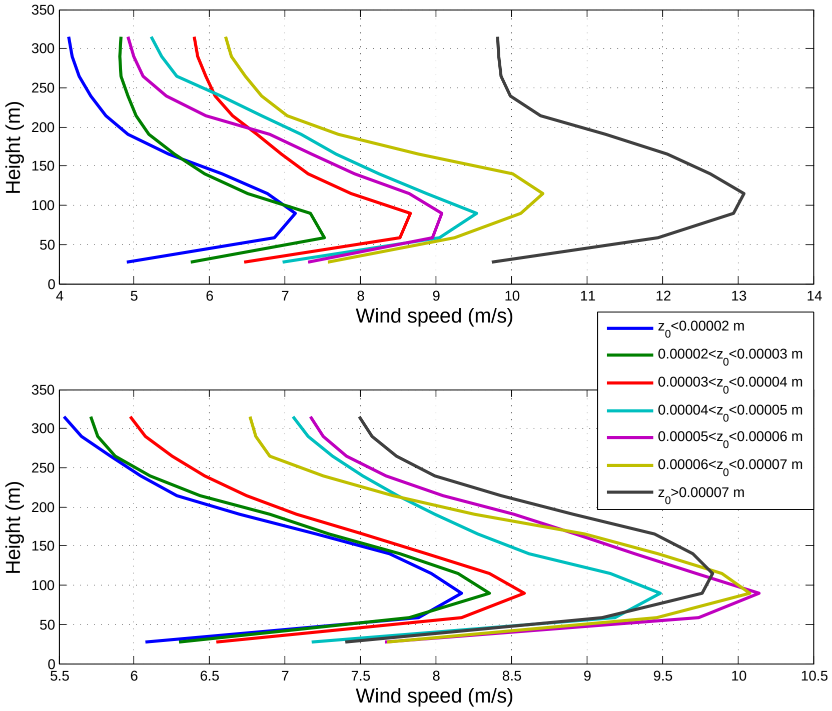

Figure 6.21: *The observed influence of z_0 with (top) and without (bottom) time criteria*

on the surface), the overall wind speed of LLJs is decreasing.

Figures 6.19, 6.20 and 6.21 show the observed influence of L, u_* and z_0. When L increasing, the wind speed is increasing and the jet height is increasing, the difference between the observed influence and the sensitivity analysis is caused by the polynomial regression process. However, the overall model show good performance that the modeled LLJs fits well to the observed LLJs with different range of L which has been shown before. From these two figures we can see that when u_* is increasing, the wind speed is increasing which is coincides with the sensitivity analysis. When z_0 is increasing, the wind speed is also increasing which is opposite to the sensitivity analysis. The reason is in this research z_0 is calculated by Charnocks' relation, when the observed u_* is increasing, z_0 is increasing, and the observed wind speed is increasing. In the sensitivity analysis, the LLJ model is influenced by the diabatic model, in which when z_0 is increasing, the wind speed is decreasing.

Chapter 7

Power production

As shown in the previous chapter, the LLJ model is not able to fit an observed instantaneous (every 10-min) LLJs profile because LLJs are time-dependent. However, the LLJ model corresponds well to the mean observed LLJs under a specific ambient condition (friction velocity, Obukhov length). This allows the model to be applied for wind turbine power production analysis. The results will be compared to power production analysis done with simple log wind profile and/or diabatic wind profile which are widely used models in wind turbine power production analysis. Zero-shear wind profile is not included for comparison, because under this model, the wind speed over the whole rotor plane is constant, the influence can be directly found in the power curve (refer to figure 7.1 for comparison).

7.1 Background of the analysis

In this chapter, the NREL 5 MW reference wind turbine and DTU 10 MW reference wind turbine are used for power production assessment. The properties of these two turbines are listed in the table 7.1, and the power curves of these two turbines are illustrated in figure 7.1.

The equivalent wind speed concept, which is proposed by Wagner [44], is applied to convert the wind speeds of an arbitrary wind shear to zero-shear wind profiles in front of the wind turbine rotor plane by assuming that these two profiles generate the same kinetic energy flux. The principle of this concept can be seen in figure 7.2. Three different definitions of the equivalent wind speed are proposed in [44] (see Equations 7.1, 7.2 and 7.3). In this study we consider Equation 7.1 since no turbulence is included in this research.

$$U_{eq1} = \frac{1}{A}\sum_i U_i \cdot A_i \tag{7.1}$$

$$U_{eq2} = \frac{1}{A}\sum_i A_i \sqrt[3]{U_i^3} \tag{7.2}$$

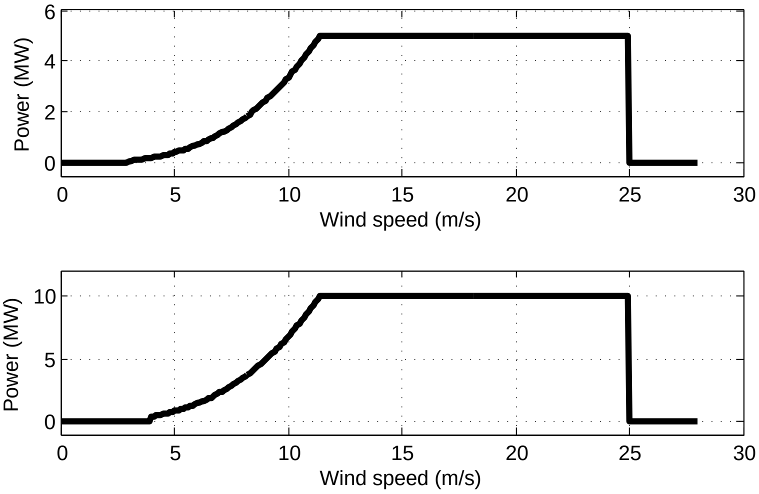

Figure 7.1: *Power curves of the two reference turbines. From top to bottom are of NREL 5 MW wind turbine and DTU 10 MW wind turbine.*

Table 7.1: *Properties of two reference turbines*

Properties	NREL 5-MW reference turbine	DTU 10-MW reference turbine
Rated Power	5 MW	10 MW
Control	Variable speed	Variable speed
Cut-in wind speed	3 m/s	4 m/s
Cut-out wind speed	25 m/s	25 m/s
Rated wind speed	11.4 m/s	11.4 m/s
Hub height	90 m	119 m
Rotor diameter	126 m	178.3 m

$$U_{eq3} = \sqrt[3]{\frac{1}{A}\sum_i U_i^3 \cdot A_i} \tag{7.3}$$

Where U_{eq1}, U_{eq2} and U_{eq3} are different definitions of equivalent wind speed proposed by Wagner [44]; A_i is the segment of rotor plane area and U_i is the corresponding wind speed as shown in figure 7.2.

The power of a particular wind shear in front of the rotor plane can be calculated as,

$$P = C_P \cdot KE_{profile} \tag{7.4}$$

Where P is power, C_P is the power coefficient and $KE_{profile}$ is the kinetic energy flux of a particular wind profile. $KE_{profile}$ can be calculated by,

$$KE_{profile} = \sum_i \frac{1}{2}\rho U_i^3 A_i \tag{7.5}$$

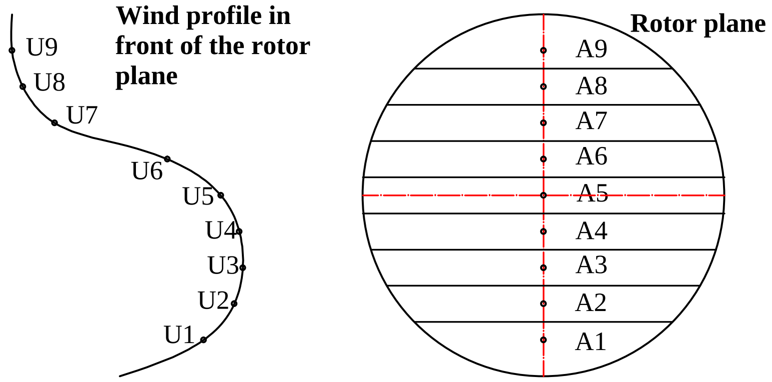

Figure 7.2: *Equivalent wind speed principle*

Where $\rho = 1.225\ kg/m^3$. Unlike observed LLJs wind speed, continuous information is available by using the LLJ model. Thus the height interval can be very small and each area in figure 7.2 can be approximated by the area of rectangular, which result in,

$$A_i = 2 \cdot dz \cdot \sqrt{R^2 - (Z_{hub} - Z_i)^2} \tag{7.6}$$

Where dz is the height interval, R is the rotor radius, Z_{hub} is the hub height and Z_i is the mean height of each height segment (the height of each black point shown in figure 7.2). Combine the equations then Equation 7.4 can be rewritten as,

$$P = C_P \cdot \sum_i \rho U_i^3 \cdot dz \cdot \sqrt{R^2 - (Z_{hub} - Z_i)^2} \tag{7.7}$$

7.2 Power analysis with known hub-height wind speed

In this section, the wind speeds of LLJs profile and the log wind profile are assumed to be the same at the hub-height. Under this condition, Obukhov length is a fixed value for a particular wind turbine. The reason can be found in the applied intersection height equation in the LLJ model, where $L = (Z_{hub} - 68)/0.4$. The fixed Obukhov lengths are 55 m for the 5 MW reference turbine and 127.5 m for the 10 MW reference turbine. Based on this equation, if a particular wind speed at hub height is defined, the friction velocity can be calculated (see table 7.2). The results of this analysis illustrate that with known wind speed at hub-height, how large the difference in power production can be due to the change in wind shear from the diabatic shear profile to a LLJ shear profile with a certain hub-height wind speed. The analysis will be done for $U_{hub} = 5, 7.5, 10, 11.5, 12.5, 15, 17.5, 20$ m/s respectively.

First the wind profiles are shown for a given hub height wind speed. The wind profiles relation are similar between the two reference turbines thus only the results of $U_{hub} = 10$ m/s of NREL 5 MW turbine are shown as example. See figures 7.3.

With increasing hub height wind speed U_{hub} and constant Obukhov length $L = 55$ m (5 MW reference turbine), the friction velocity/roughness length is increasing. This results

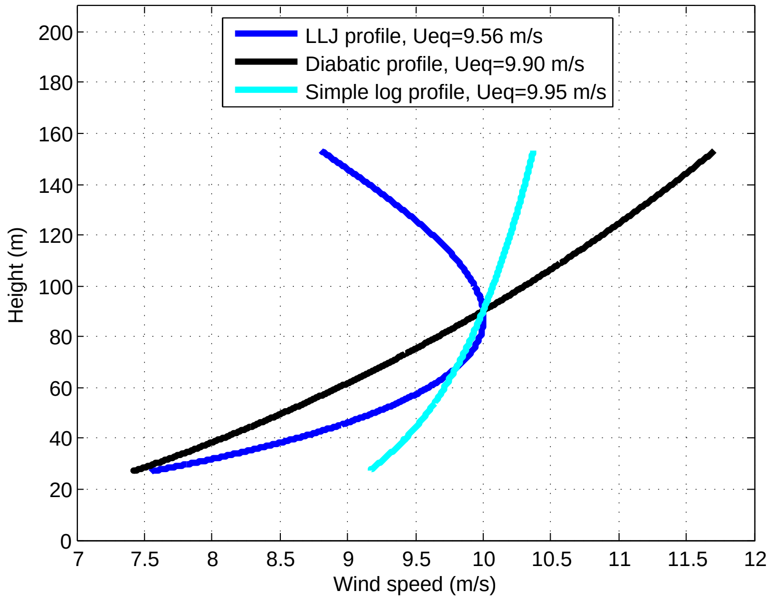

Figure 7.3: *Overview of different profiles (5 MW wind turbine,* U_{hub}*=10 m/s)*

Table 7.2: *Power analysis with certain hub-height wind speed*

Hub height wind speed (m/s)	u_* of NREL 5-MW turbine (m/s)	u_* of DTU 10-MW turbine (m/s)
5	0.09	0.10
7.5	0.14	0.16
10	0.19	0.22
11.5	0.23	0.26
12.5	0.25	0.28
15	0.30	0.34
17.5	0.36	0.41
20	0.42	0.48

in an increasing overall wind speed and increasingly strong wind shear at each profiles. The equivalent wind speeds are constantly lower than that of the diabatic wind profile and the simple log wind profile. Though the shears of diabatic wind profiles and simple log profiles are distinguishing, the equivalent wind speeds of these two wind model at a certain condition are quite close to each other.

Further analysis of the kinetic energy flux and power can be seen at figures 7.4 and 7.5. Based on figure 7.4, we know that with an increasing hub height wind speed (increasing friction velocity), the difference of kinetic energy flux between LLJs and diabatic wind profile/simple log wind profile is increasing. The difference is even bigger for a larger turbine.

In figure 7.5, the difference of the power curve between the LLJs profile and diabatic wind profile/simple log wind profile keeps increasing until the diabatic wind profile/simple log wind profile reaches the rated power. After the diabatic wind profile and the simple

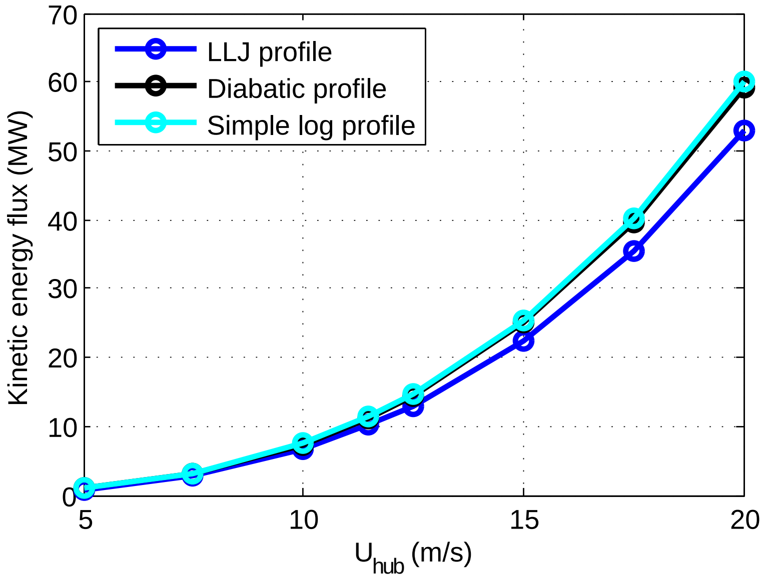

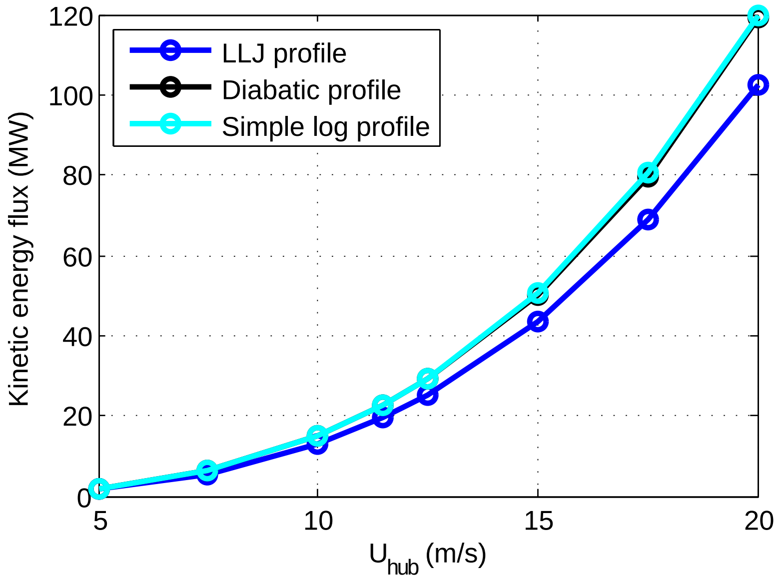

Figure 7.4: *Kinetic energy flux of two reference turbines. The analysis is done under different hub height wind speeds. The upper figure is of NREL 5 MW wind turbine and the bottom figure is of DTU 10 MW wind turbine.*

log wind profile reach the rated power, the difference will decrease due to continually increasing power of the LLJs profile. When the line of LLJs profile reaches the rated power, the difference becomes zero. The maximum difference is bigger for a turbine with larger rotor plane.

It can be concluded that the power production will decrease when a LLJ occurs if considering a fixed hub height wind speed in power assessment. And the difference increases for a larger turbine. The power production difference between LLJs profile and diabatic

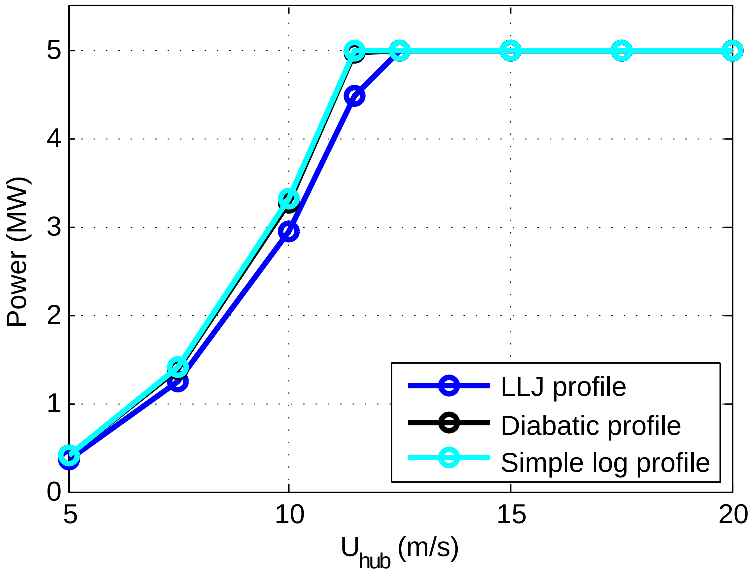

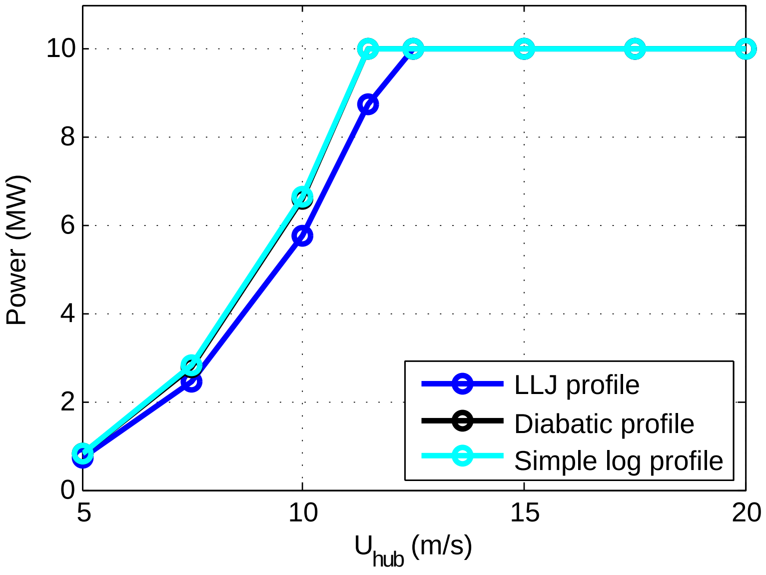

Figure 7.5: *Power curve of two reference turbines. The analysis is done under different hub height wind speeds. The upper figure is of NREL 5 MW wind turbine and the bottom figure is of DTU 10 MW wind turbine.*

profile is summarized in the table 7.3. From the table we can see that the difference can go up to around 10% with an increasing hub height wind speed, moreover, we can expect a even larger maximum difference for a wind turbine with larger rotor plane.

Table 7.3: Power production difference $P_{diff} = P_{LLJs} - P_{diabatic}$ under certain hub height wind speed

Hub height wind speed (m/s)	P_{diff} of 5 MW turbine (MW)	P_{diff} of 10 MW turbine (MW)
5	-0.0376	-0.0963
7.5	-0.1321	-0.3390
10	-0.3222	-0.8301
11.5	-0.4970	-1.2749
12.5	0	0
15	0	0
17.5	0	0
20	0	0

7.3 Power analysis with certain ambient conditions

In this section, the ambient conditions (roughness length, friction velocity, Obukhov length) for the LLJ and diabatic model are the same. The results show how large the power difference can be for given conditions if ambient conditions are the same. The two variables, which are friction velocity and Obukhov length, will be analyzed separately.

First it is assumed the Obukhov length is fixed at 150 m and the friction velocity is varying, where $u_* = 0.15, 0.18, 0.22, 0.3, 0.35, 0.45, 0.55$ m/s. The results are shown in the following figures.

For a certain ambient condition, the wind profiles are the same for the two reference turbines, but the partial wind profiles in front of the rotor planes are different. Figure 7.6 shows the different wind profiles that covers the two reference turbine rotor planes when friction velocity varies. One feature can be seen from the figure is that with an increasing friction velocity, the shear of both LLJ wind profile and dabatic wind profile are becoming stronger. Another feature has been stated before is that below the intersection height, the wind speed of LLJs are constantly bigger than that of diabtic wind profile. These two properties will result in different kinetic energy flux and power, see Figures 7.7 and 7.8.

The results in Figures 7.7 and 7.8 show two different situations. Under same ambient condition, the 5 MW turbine gains power when LLJs occur while the 10 MW turbine loses power. As has been discussed above, it is due to the hub height and rotor radius difference. When the friction velocity increases, the amount of gained/lost power increases. The power production difference between LLJs profile and diabatic profile is summarized in the table 7.4. It can be seen from the table that with an increasing friction velocity, the difference can go up to around $+7\%$ of the rated power for the 5 MW wind turbine and go down to around -4%.

The second analysis is done for a fixed friction velocity and a varying Obukhov length. A chosen fixed friction velocity is $u_* = 0.2$ m/s, and the varying Obukhov length is $L = 20, 60, 100, 140, 180$ m. It can be seen from the Figure 7.9 that when L is increasing, the intersection height is increasing, the wind speeds are decreasing and the wind shears are becoming weaker.

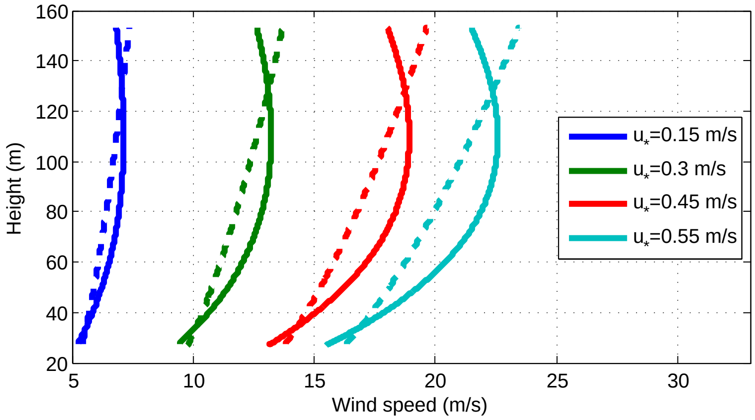

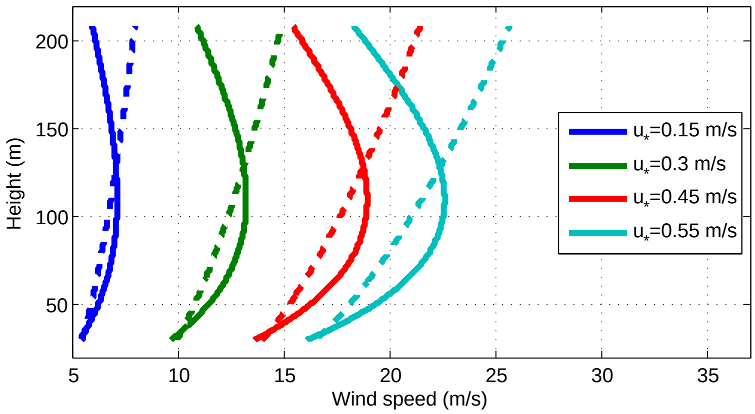

Figure 7.6: *Wind profiles of $L = 150$ m. The upper figure is of NREL 5 MW wind turbine and the bottom figure is of DTU 10 MW wind turbine.*

Table 7.4: *Power production difference $P_{diff} = P_{LLJs} - P_{diabatic}$ under certain L (L=150 m)*

Friction velocity (m/s)	P_{diff} of 5 MW turbine (MW)	P_{diff} of 10 MW turbine (MW)
0.15	0.1243	-0.1309
0.18	0.2060	-0.2172
0.22	0.3590	-0.3789
0.3	0	0
0.35	0	0
0.45	0	0
0.55	0	0

In Figure 7.10 the kinetic energy flux of the diabatic wind profiles decreases more sharply than that of LLJ profiles when Obukhov length increases. At the upper plot in this Figure, the kinetic energy flux of diabatic wind profiles is bigger than that of LLJ profiles at the beginning, but after $L = 100$ m, the situation reversed. The reason can be found from Figure 7.9, which is the increasing intersection height. After $L = 100$ m, the intersection height is higher than the hub height of the 5 MW reference turbine, which means more

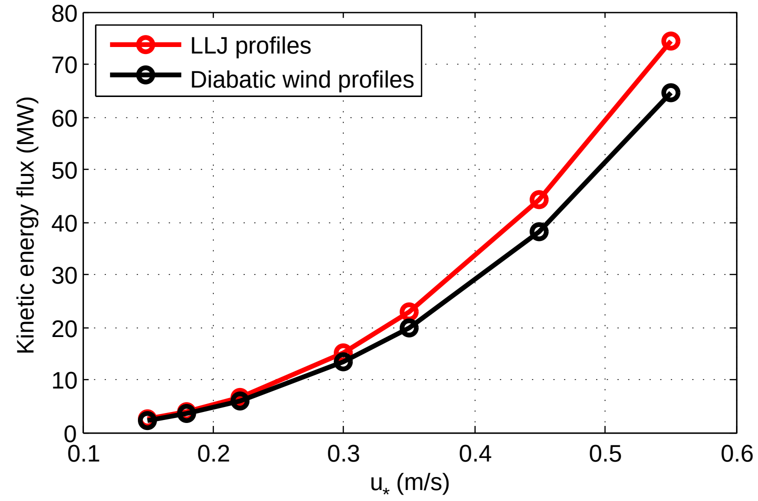

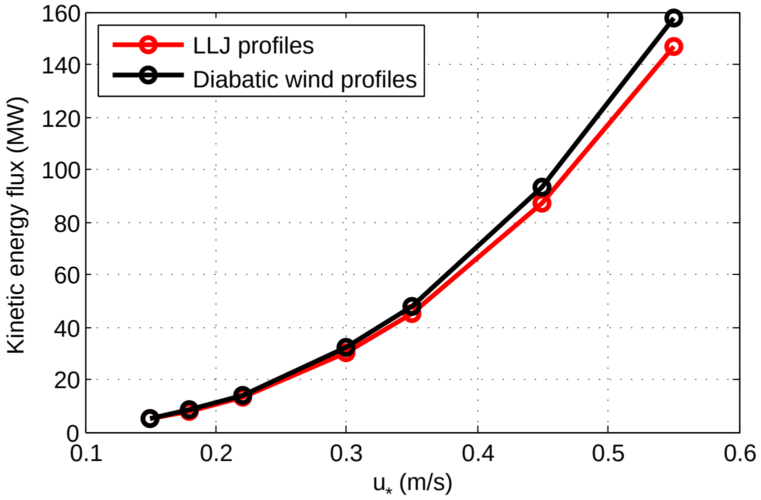

Figure 7.7: *Kinetic energy of varying* u_{star}. *The upper figure is of NREL 5 MW wind turbine and the bottom figure is of DTU 10 MW wind turbine.*

area of rotor plane is covered by the region in which LLJs wind speeds are higher than diabatic wind speeds. Although the kinetic energy flux of LLJ profiles decreases slower than that of diabatic wind profiles, this reversion does not happen for the 10 MW reference turbine because the hub height is relatively higher and the rotor plane is mostly covered with the region in which LLJs wind speeds are lower than diabatic wind speeds.

The resultant influence on power can be seen in Figure 7.11. When L is increasing, the power production will decrease. For both reference turbines, the power production difference first decreases and then increases, but a reversion can only be seen at the 5 MW wind turbine which coincides with the kinetic energy flux Figure 7.10. The power production difference between LLJs profile and diabatic profile is summarized in the table 7.5. According to the table, the difference varies from around -5% to around $+6\%$ of the rated power for the 5 MW turbine, and from around -10% to around $+5\%$ of the

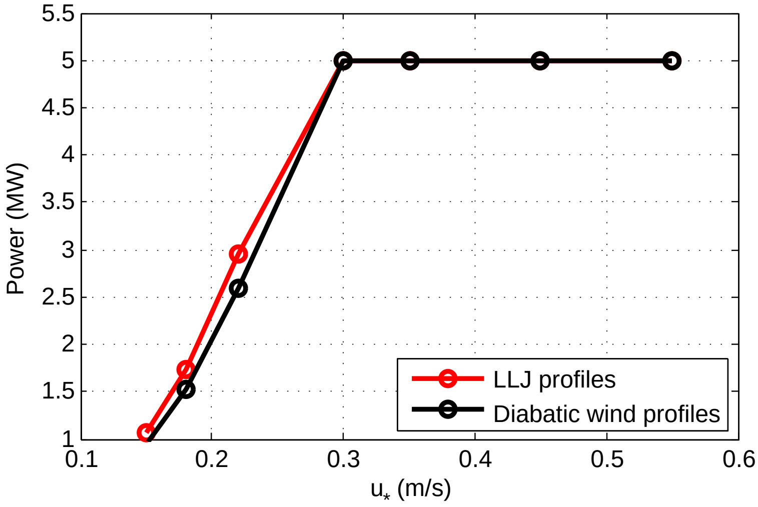

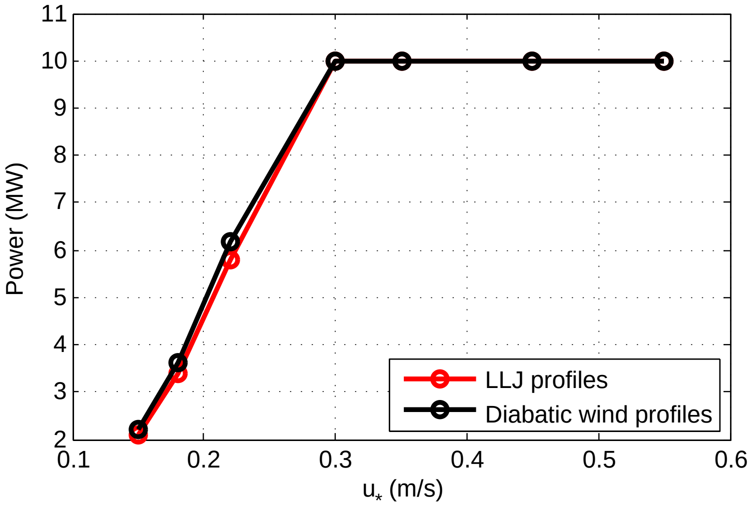

Figure 7.8: *Power of varying u_{star}. The upper figure is of NREL 5 MW wind turbine and the bottom figure is of DTU 10 MW wind turbine.*

Table 7.5: *Power production difference $P_{diff} = P_{LLJs} - P_{diabatic}$ under certain u_* ($u_* = 0.2$ m)*

Obukhov length (m/s)	P_{diff} of 5 MW turbine (MW)	P_{diff} of 10 MW turbine (MW)
20	0	0
60	-0.2741	-2.9908
100	0.1002	-1.2900
140	0.2544	-0.4380
180	0.3145	0.0484

rated power for the 10 MW turbine.

As a conclusion, a wind turbine might produce either more or less power than expected

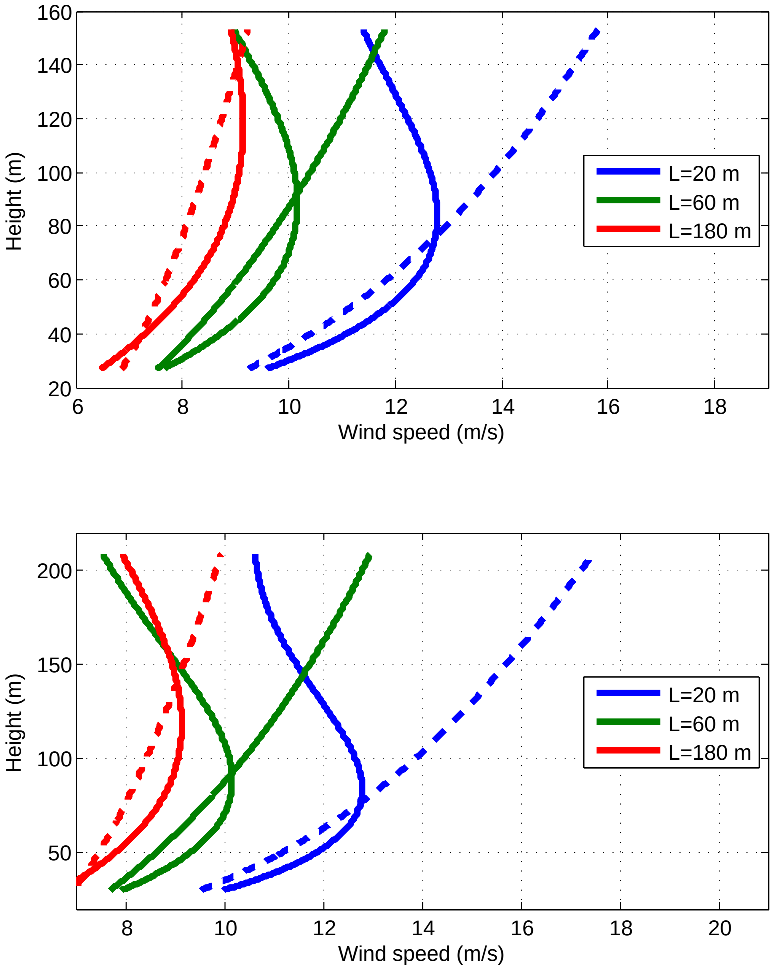

Figure 7.9: *Wind profiles of* $u_* = 0.2\ m/s$. *The upper figure is of NREL 5 MW wind turbine and the bottom figure is of DTU 10 MW wind turbine.*

when LLJs occur. This depends on the ambient conditions and the size of the turbine. In this analysis, L varies from 20 m to 180 m which covers most stability conditions under which LLJ may occur. Thus a gain in power production due to LLJs is most likely to happen at smaller wind turbines with lower hub heights because the intersection height is hard to reach the hub heights of large wind turbines.

7.4 Simulations on Bladed

For verifying the theoretical results illustrated above, similar analysis are done in the simulations software Bladed. Bladed is a complete developed software used for wind turbine performance and load calculations. In this section, the NREL 5 MW turbine is used and different wind shears are prescribed into Bladed to calculate the power production.

Firstly, the wind speeds of LLJ profile, diabatic profile and simple log wind profile are assumed to be the same at the hub height similar as in section 7.2. The analysis is done for

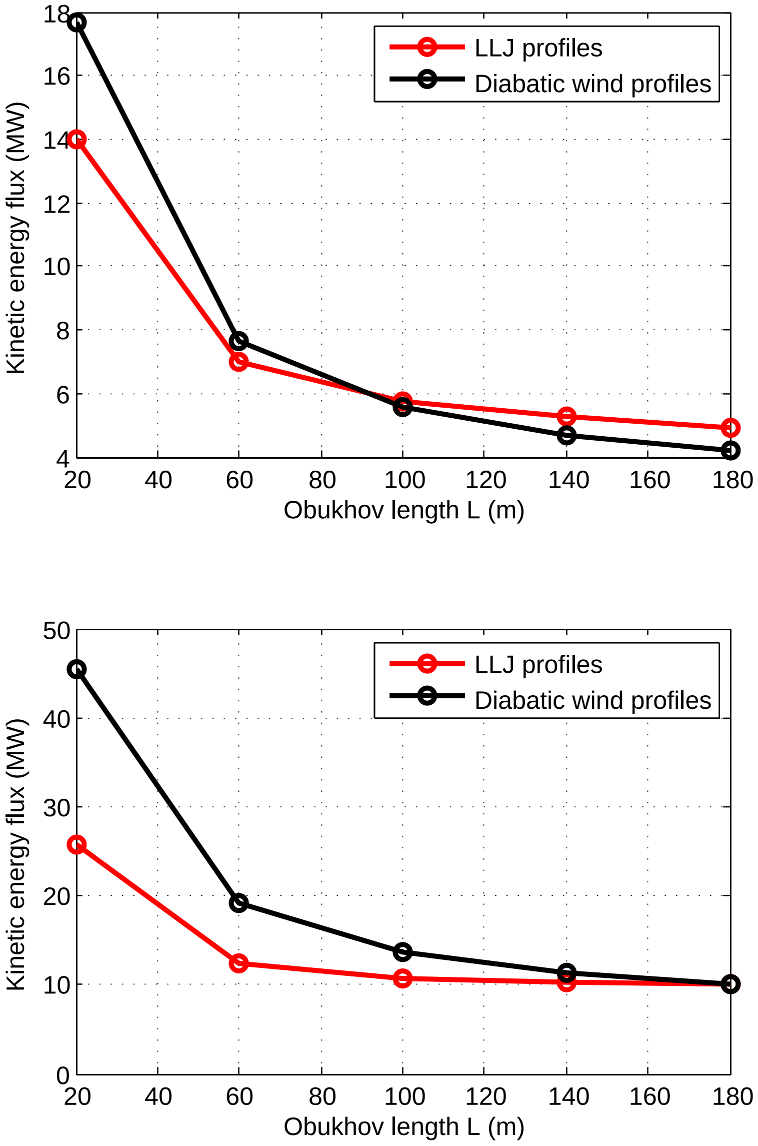

Figure 7.10: *Kinetic energy of varying L. The upper figure is of NREL 5 MW wind turbine and the bottom figure is of DTU 10 MW wind turbine.*

$U_{hub} = 5, 7.5, 10, 12.5, 15, 17.5, 20\ m/s$ respectively. The results are shown in Figure 7.12.

The simulated results are the same as the theoretical results in section 7.2 that the NREL 5 MW turbine generates less or equal power when LLJ occur. In the Figure the power generation of diabatic profile and simple log profile are overlapping thus only one line is visible. It can be inferred that the simple log profile/ diabatic profile line will first reaches the rated power, and LLJs causes a reduction in power production.

Secondly, the simulations are done with a fixed L and varying u_*, where $L = 150m$ and $u_* = 0.15, 0.18, 0.22, 0.3, 0.35, 0.45, 0.55\ m/s$. The results can be seen in Figure 7.13. The simulated results are also in accordance with the theoretical results that the NREL 5 MW

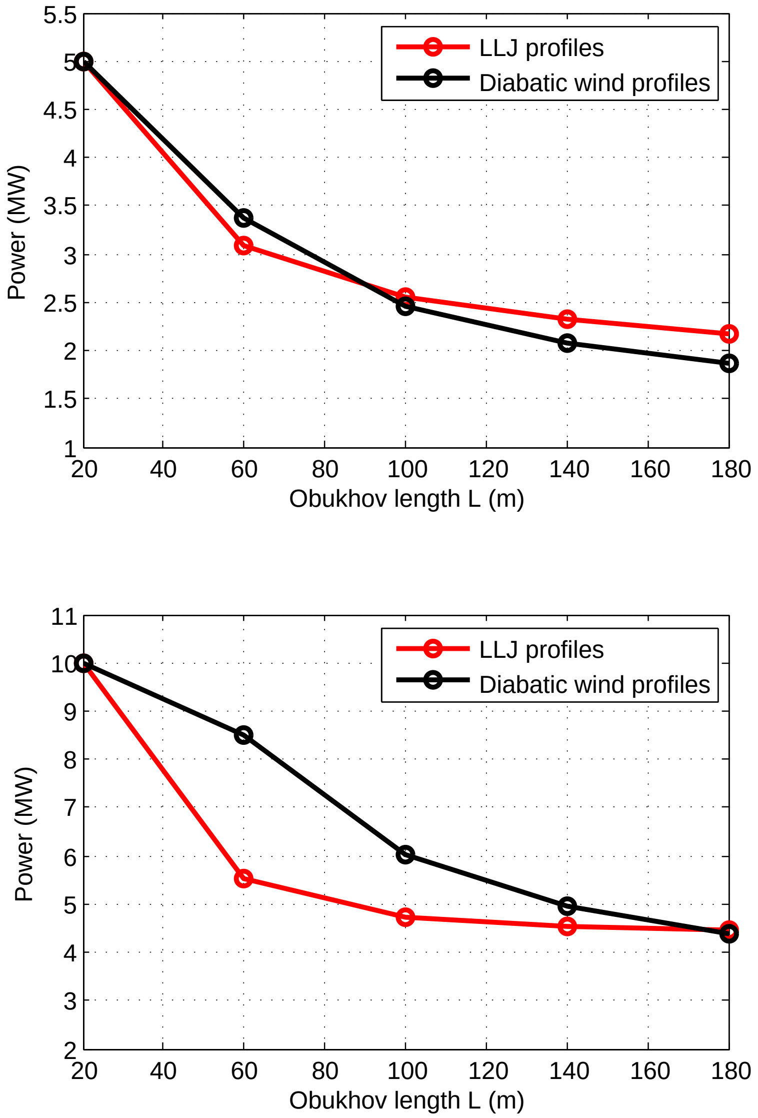

Figure 7.11: *Power of varying L. The upper figure is of NREL 5 MW wind turbine and the bottom figure is of DTU 10 MW wind turbine.*

turbine generates more power when LLJ occur. The reason is the jet height of LLJ is higher than the hub height of the 5 MW turbine and brings more energy than diabatic wind profile/ simple log wind profile.

Thirdly, the simulations are done with a fixed u_* and varying L, where $u_* = 0.2$ and $L = 20, 60, 100, 140, 180\ m$. The results can be seen in Figure 7.14. The simulated results also coincide with the theoretical results that an reversion is also reflected in the power production.

To compare the theoretical power production to the simulated power production of LLJs profile, the Figure 7.15 is plotted to show both the theoretical and simulated results. Two results have high agreement.

From the results of simulation it can be concluded that the influence of LLJs on wind

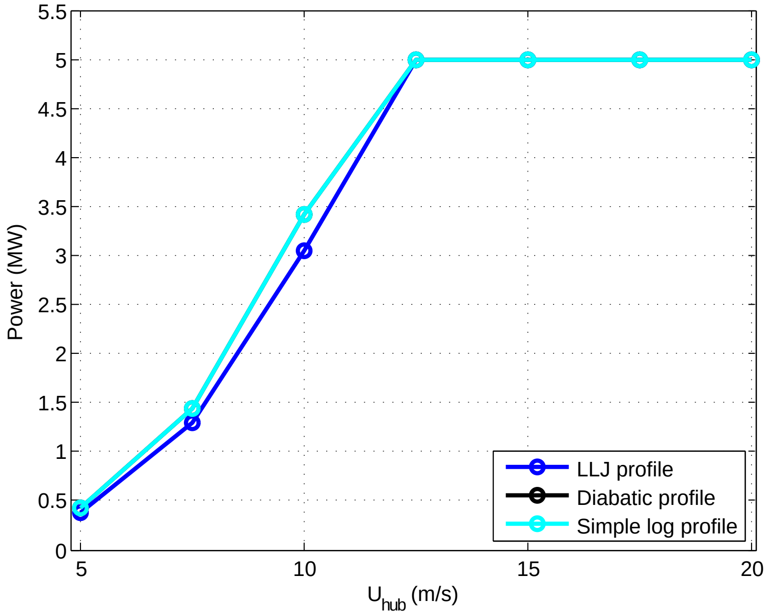

Figure 7.12: *Power of certain hub height wind speeds of NREL 5 MW wind turbine (simulated on Bladed)*

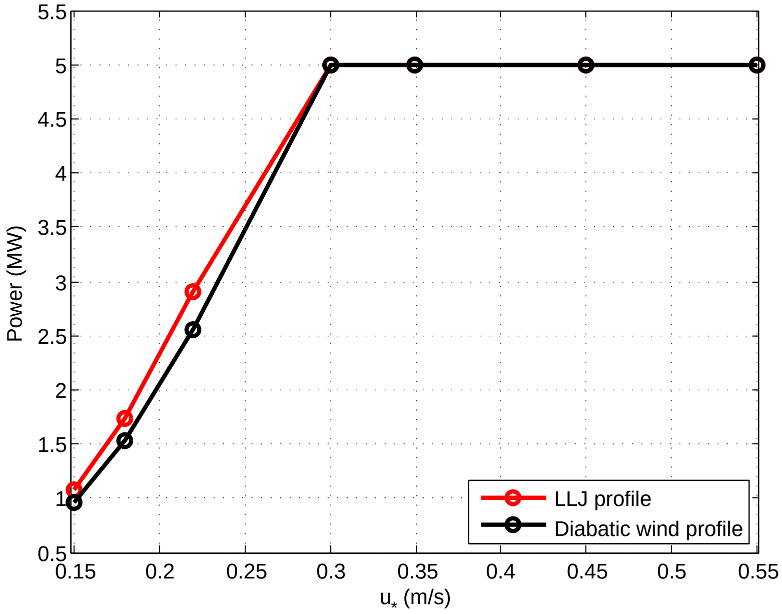

Figure 7.13: *Power of varying u_* of NREL 5 MW wind turbine (simulated on Bladed)*

turbine power production is determined by several factors: Obukhov length, friction velocity, wind turbine hub height and wind turbine rotor radius.

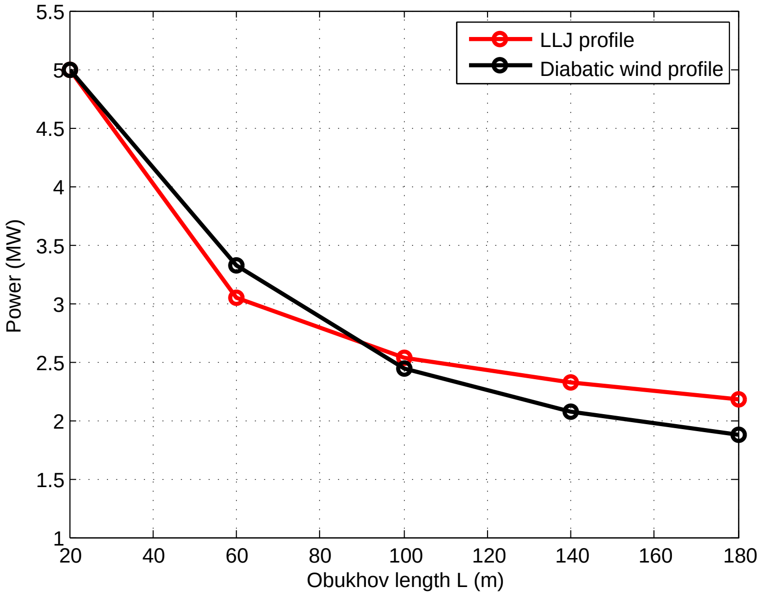

Figure 7.14: *Power of varying L of NREL 5 MW wind turbine (simulated on Bladed)*

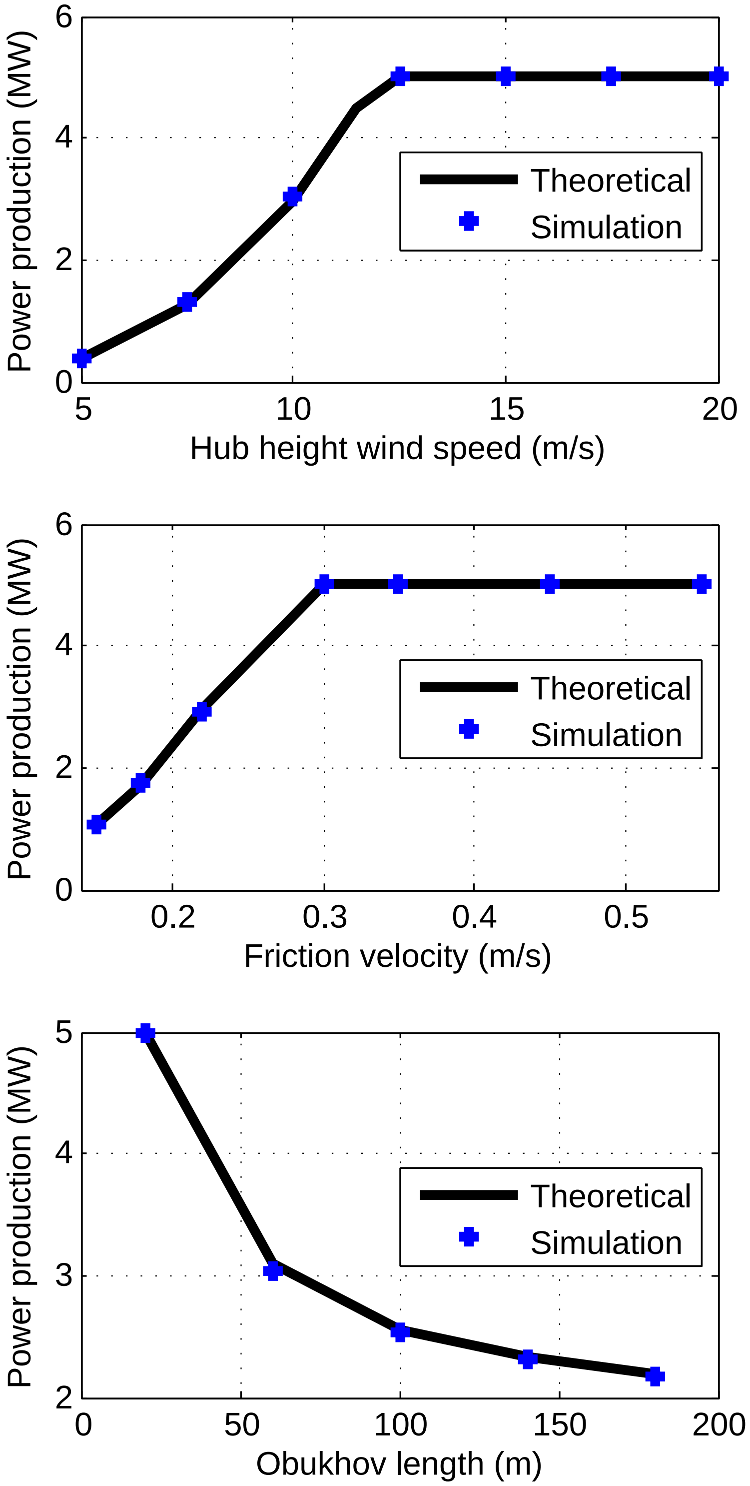

Figure 7.15: *Comparison between theoretical result and simulation of NREL 5 MW wind turbine. From top to bottoms are of certain hub height wind speed, certain Obukhov length (L=150 m) and certain friction velocity (u_*=0.2 m/s).*

Chapter 8

Discussion

In this chapter some deficiencies in this research are pointed out and discussed.

The data were mostly measured by LiDAR. As has been discussed in Chapter 4, the LiDAR was installed at the corner inside the met-mast structure. In another word, the data measured by LiDAR is relatively unreliable with comparison to the data measured by wind cups and wind vanes. Although some adjustments were made to improve the quality of the data, the validity cannot be well proved.

The offshore meteorology site IJmuiden was chosen due to the reason that most LLJs related research was carried out onshore. As a result, the new LLJ model developed in this research is only applicable for offshore.

The upper observation height at IJmuiden was 315 m, which is higher than the maximum wind turbine height. However, as has been described in Chapter 6, the observed intersection height might be confined within 120 m by the upper observation height limit. If this confinement indeed happened, the intersection height should have been higher when L is large. As a consequence, power production of both large wind turbine and small wind turbine may both benefit from LLJs.

Baas' criteria was applied to filter the observed wind profiles to find LLJs. He defined that the maximum wind speed should be at least 2 m/s and 25 % bigger than the next minimum. Applying this precisely defined criteria, many LLJs with relatively weak wind shear might be filtered out. It follows that these weak LLJs are not included in the new model and the power production analysis as well, but these LLJs will definitely influence the fatigue, load and power production of wind turbines.

This research only focused on LLJs phenomenon under stable atmospheric conditions. However, as has been found in Chapter 5, special phenomenon was observed under unstable conditions which conforms to Baas' criteria. Though this phenomenon cannot be explained by standard LLJs theory, it might have similar influence on wind turbines.

Lastly, the new LLJ model failed when the atmosphere is extremely stable. The reason was that the stability parameter applied in the diabatic wind profile model was unreliable under very stable conditions. In practice, the influence of LLJs on wind turbines is even stronger under extreme stable conditions. Thus an improvement of the stability parameter is required.

Chapter 9

Conclusions and Recommendations

9.1 Conclusions

In this section the main findings in this research are listed below. This research was carried out mainly based on 10-min wind data measured by wind cups, wind vanes and LiDAR in 2012.

Following Baas' LLJs criteira, 448 LLJs were observed with time criteria, which belong to 21 days in the year. Over 90 % of these LLJs were found under very stable conditions. While 1140 LLJs were observed without time criteria. These LLJs belong to 114 days in the year, which means there were 1/3 days in the year observed with the occurrence of LLJs. Over 80 % of these LLJs were found under very stable conditions. It can be concluded that the LLJ is a frequent phenomenon not only, as has been reported, onshore, but also offshore. LLJs are most likely occur under very stable conditions.

Comparing the diabatic wind profile to the LLJ wind profile under the same condition (u_*, L), it was found that the diabatic wind profile is not able to describe the occurrence of LLJs correctly. Especially when the atmospheric condition is very stable, the diabatic wind profile becomes a straight line, which failed to correspond with the actual situation.

The new LLJ model can be developed by defining the intersection height. The intersection height was found to be associated to atmospheric stability that the intersection height increases with decreasing stability. This height is important to wind turbine power analysis, because it determines below what height the wind turbine will gain power from the occurrence of LLJs.

As an answer to the main question, LLJs should be included in offshore wind turbine design. It can be modeled in a simple way for wind turbine power analysis, and the new LLJ model is based on three parameters: Obukhov length, friction velocity and roughness length. It was found that 1) when Obukhov length increased the jet speed decreased, but the jet height increased; 2) when friction velocity increased the jet speed decreased and the wind shear became weak; 3) and when roughness length increased the overall wind speed decreased.

Applying the new LLJ model on LLJs power production analysis, it was found that the wind turbine can produce either more or less power with the occurrence of LLJs depending on the three factors mentioned above and the size of the turbine. For instance, power production difference of the two reference wind turbine due to the occurrence of LLJs differed from the diabatic shear power production varied from 0 to 0.36 MW (5 MW) and from -0.38 to 0 MW (10 MW) respectively when friction velocity varied from 0.15 to 0.55 m/s. When Obukhov length varied from 20 to 180, the difference varied from -0.27 to 0.31 MW (5 MW) and from -2.99 to 0.05 MW (10 MW) respectively. Besides, the simulated results coincided with the theoretical one, which confirmed the applicability of the model for simulations.

9.2 Recommendations

In this section, several recommendations are made for future research.

Load and fatigue are crucial domain of research regarding wind turbine performance. The LLJ model, as has been stated in chapter 7, can be used on load and fatigue research. Thus similar to applying the model on wind turbine power production analysis, this model is recommended to be used to do studies and simulations on wind turbine fatigue and load research.

Forecasting LLJs for power prediction will be an easy task if we have a change of perspective. With abundant data, the regular of the probability and duration of LLJs occurrence under different stability conditions can be found. In each type of stability condition, the LLJs profile can be modeled. These combined knowledge can be used together with historical stability data at a specific designed wind farm site to approximate the power production caused by LLJs.

The new LLJ model which has been developed in this research is only applicable offshore, the applicability onshore remains unknown. It it proposed that further research should be accomplished onshore (in different types of terrain).

As has been found in Chapter 5, special atmospheric phenomenon was observed. This phenomenon has similar vertical wind profile with LLJs, while the very unstable conditions in which it may occur was opposite to the properties of LLJs. Studies need to be done to explain this phenomenon and analyze its influence on LLJs.

Last but not least, the stability parameter applied in diabatic wind profile model is not reliable under very stable conditions. To enhance the quality of the LLJ model, the stability parameter under stable condition need to be improved.

Reference

[1] P. Baas, F. C. Bosveld, H. K. Baltink, and A. A. M. Holtslag. A climatology of nocturnal low-level jets at Cabauw. *Journal of Applied Meteorology and Climatology*, 48: 1627 – 1642, 2009.

[2] N. Kelley, M. Shirazi, D. Jager, S. Wilde, J. Adams, and M. Buhl. Lamar Low-Level Jet Project Interim Report. Technical Report NREL/TP-500-34593, National Renewable Energy Laboratory, Jan. 2004.

[3] N. Kelley. The Great Plains Turbulence Environment: Its Origins, Impact and Simulation. Technical Report NREL/CP-500-40176, National Renewable Energy Laboratory, Jun. 2006.

[4] D. Sisterson and P. Frenzen. Nocturnal Boundary-layer Wind Maxima and Problem of Wind Power Assessment. *Environmental Science and Technology*, 12: 218 – 221, 1978.

[5] IEC 2005. *IEC 61400-1:Design requirements. 3 ed*, 2005.

[6] M. D. Takahashi. Mitigation of Wind Turbine/Vortex Interaction Using Disturbance Accommodating Control. Technical Report NREL/TP-500-35172, National Renewable Energy Laboratory, Dec. 2003.

[7] S. Wharton and J. K. Lundquist. Atmospheric Stability Impacts on Power Curves of Tall Wind Turbines - An Analysis of a West Coast North American wind farm. Technical Report LLNL-TR-424425, Lawrence Livermore National Laboratory, Feb. 2010.

[8] R. Wagner, M. Courtney, J. Gottschall, and P. Lindelöw-Marsden. Accounting for the speed shear in wind turbine power performance measurement. *Wind energy*, 14: 993 – 1004, 2011.

[9] R. B. Stull. *An introduction to boundary layer meteorology.* U.S. Atomic Energy Commission, Division of Technical Information, 1988. ISBN 9-027-72769-5.

[10] E. J. Plate. *Aerodynamic characteristics of atmospheric boundary layers.* AEC critical review series. U.S. Atomic Energy Commission, Division of Technical Information, 1971. ISBN B-000-6C1U5-Q.

[11] H. Charnock. Wind stress on a water surface. *Quarterly Journal of the Royal Meteorological Society*, 81: 639 – 640, 1955.

[12] J. W. Deardorff. Dependence of air-sea transfer coefficients on bulk stability. *Journal of Geophysical Research*, 73: 2549 – 2557, 1968.

[13] J. A. Businger, J. C. Wyngaard, Y. Izumi, and E. F. Bradley. Flux profile relationships in the atmospheric surface layer. *Journal of Atmospheric Sciences*, 28: 181 – 189, 1971.

[14] A. A. Grachev and C. W. Fairall. Dependence of the MoninObukhov stability parameter on the Bulk Richardson number over the ocean. *Journal of Applied Meteorology*, 36: 406 – 414, 1996.

[15] A. J. M. Wijk, A. C. M. Beljaars, A. A. M. Holtslag, and W. C. Turkenburg. Evaluation of stability corrections in wind speed profiles over the North Sea. *Journal of Wind Engineering and Industrial Aerodynamics*, 33: 551 – 566, 1990.

[16] A. J. Dyer. A review of flux-profile relations. *Boundary Layer Meteorology*, 1: 363 – 372, 1974.

[17] C. A. Paulson. The mathematical representation of wind speed and temperature in the unstable atmospheric surface layer. *Journal of Applied Meteorology*, 9: 857 – 861, 1970.

[18] A. A. M. Holtslag. Applied modeling of the nighttime surface energy balance over land. *Journal of Applied Meteorology*, 27: 689 – 704, 1988.

[19] S. E. Gryning, E. Batchvarova, B. Brmmer, H. Jrgensen, and S. Larsen. On the extension of the wind profile over homogeneous terrain beyond the surface boundary layer. *Boundary-layer meteorology*, 124: 251 – 268, 2007.

[20] J. Goualt. vents en altitude fort lamy (tchad). *Annales de Physique du Globe de la France d' Outre-Mer*, 33: 373 – 379, 1938.

[21] S. J. Farquharson. The diurnal variation of wind over tropical Africa. *Quarterly Journal of the Royal Meteorological Society*, 65: 15 – 183, 1939.

[22] A. K. Blackadar. Boundary layer wind maxima and their significance for the growth of nocturnal incersions. *Bulletin American Meteorological Society*, 38: 283 – 290, 1957.

[23] W. H. Hoecker. Three southerly low-level jet streams delineated by the Weather Bureau special pibal network of 1961. *Monthly Weather Review*, 91: 199 – 205, 1963.

[24] W. D. Bonner. Climatology of the low level jet. *Monthly Weather Review*, 96: 833 – 850, 1968.

[25] L. W. Uccellini. On the role of upper tropospheric jet streaks and leeside cyclogenesis in the development of low-level jets in the Great Plains. *Monthly Weather Review*, 108: 1689 – 1696, 1980.

[26] B. Kelbe. Features of westerly waves propagating over southern Africa during summer. *Monthly Weather Review*, 116: 60–70, 1988.

[27] M. A. Wilson. Atmospheric tidal motions over Australia below 20 kilometers. *Monthly Weather Review*, 103: 1110 – 1120, 1975.

[28] R. Brook. The Koorin nocturnal low-level jet. *Boundary-layer meteorology*, 32: 8133 – 154, 1985.

[29] T. D. Keenan, J. McBride, G. Holland, N. Davidson, and B. Gunn. Diurnal variations during the Australian monsoon experiment (AMEX) phase II. *Monthly Weather Review*, 117: 2535 – 2552, 1989.

[30] W. Schwerdtfeger. The effect of the Antarctic Peninsula on the temperature regime of the Weddell Sea. *Monthly Weather Review*, 103: 45 – 51, 1975.

[31] J. R. Holton. The diurnal boundary layer wind oscillation above sloping yerrain. *Tellus*, 19: 199 – 205, 1967.

[32] W. D. Bonner and J. Paegle. Diurnal variations in boundary layer winds over the South-central United States in summer. *Monthly Weather Review*, 98: 735 – 744, 1970.

[33] E. R. Reiter. Tropopause circulation and jet streams. *World Survey of Climatology*, 4: 85 – 193, 1969.

[34] J. R. Holton. *An Introduction to Dynamic Meteorology.* Academic Press. U.S. Atomic Energy Commission, Division of Technical Information, 1972.

[35] A. K. Blackadar. The vertical distribution of wind and turbulent exchange in a neutral atmosphere. *Journal of Geophysical Researchy*, 67: 3095 – 3102, 1962.

[36] E. Andreas, K. Claffy, and A. Makshtas. Low-level atmospheric jets and inversions over the western Weddell Sea. *Boundary-layer Meteorology*, 97: 459 – 486, 2000.

[37] R. M. Banta, R. K. Newsom, J. K. Lundquist, Y. L. Pichugina, R. L. Coulter, and L. Mahrt. Nocturnal low-level jet characteristics over Kansas during CASES-99. *Boundary-Layer Meteorology*, 105: 221 – 252, 2001.

[38] C. Whiteman, X. Bian, and S. Zhong. Low-level jet climatology from enhanced rawinsonde observations at a site in the southern Great Plains. *Journal of Applied Meteorology*, 36: 1363 – 1376, 1997.

[39] E.J. Werkhoven and J. P. Verhoef. Offshore meteorological mast IJmuiden: Abstract of instrumentation report. Technical Report ECN-Wind Memo-12-010, ECN, Feb. 2012.

[40] A. Peña. *Sensing the wind profile.* Ph.D. Thesis, RisøDTU, 2009.

[41] KNMI website. `http://www.knmi.nl/klimatologie/daggegevens/weerkaarten`, 2012.

[42] A. Shapiro and E. Fedorovich. Analytical description of a nocturnal low-level jet. *Quarterly Journal of the Royal Meteorological Society*, 136: 1255 – 1262, 2010.

[43] B. J. H. Wiel, A. F. Moene, G. J. Steeneveld, P. Baas, F. C. Bosveld, and A. A. M. Holtslag. A conceptual view on inertial oscillations and nocturnal low-level jets. *American Meteorological Society*, 67: 2679 – 2688, 2010.

[44] R. Wagner, I. Antoniou, S. M. Pedersen, M. S. Courtney, and H. E. J. The influence of the wind speed profile on wind turbine performance measurements. *Wind energy*, 12: 348 – 362, 2009.

Appendix A

Observed LLJs in each sector

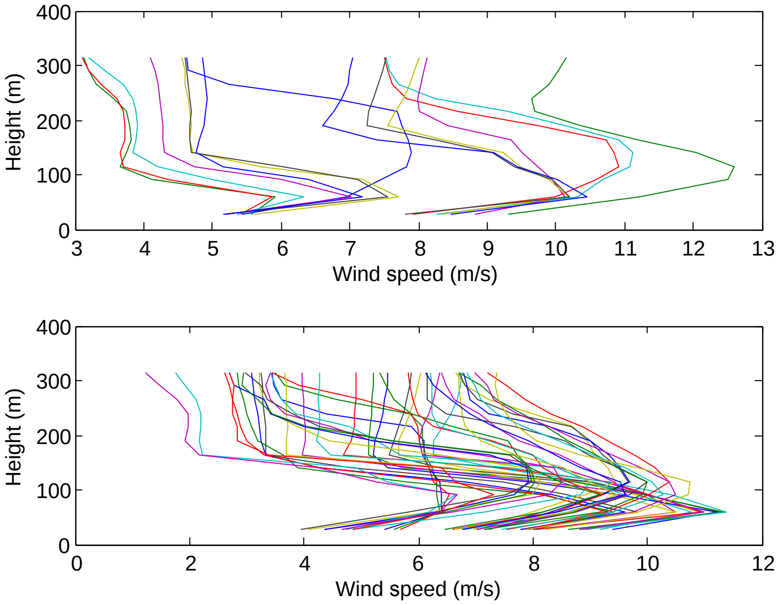

Figure A.1: *Observed LLJs with time criteria in sector 1 and 2*

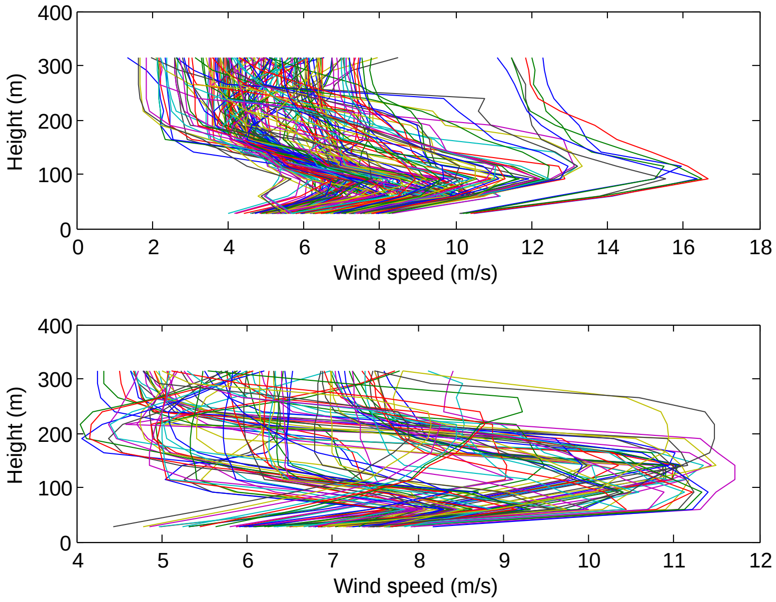

Figure A.2: *Observed LLJs with time criteria in sector 3 and 4*

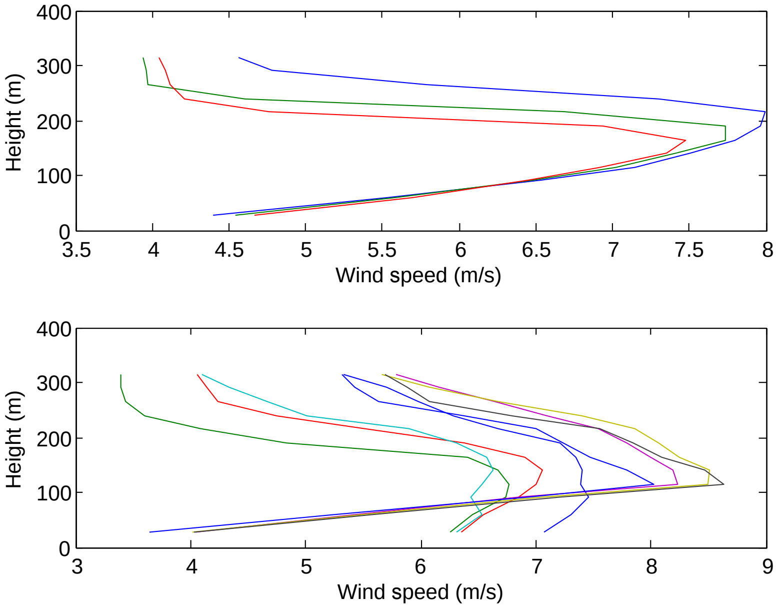

Figure A.3: *Observed LLJs with time criteria in sector 5 and 6*

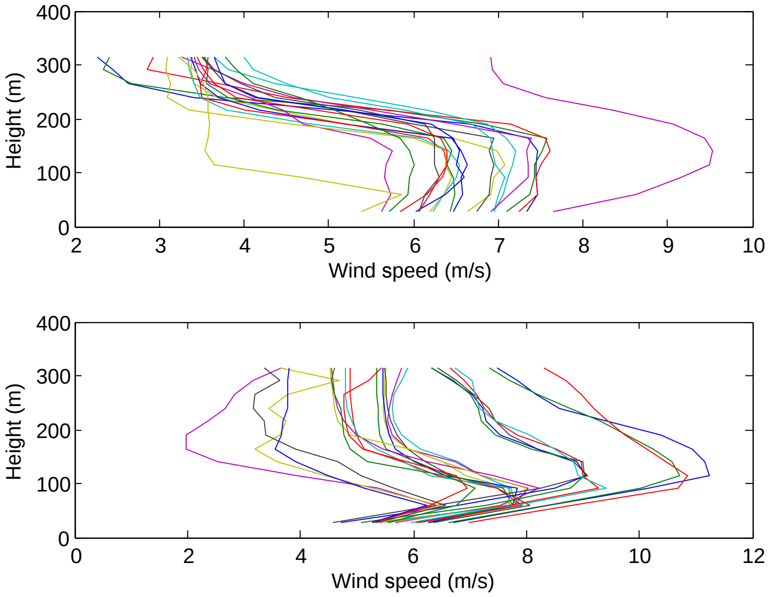

Figure A.4: *Observed LLJs with time criteria in sector 7 and 8*

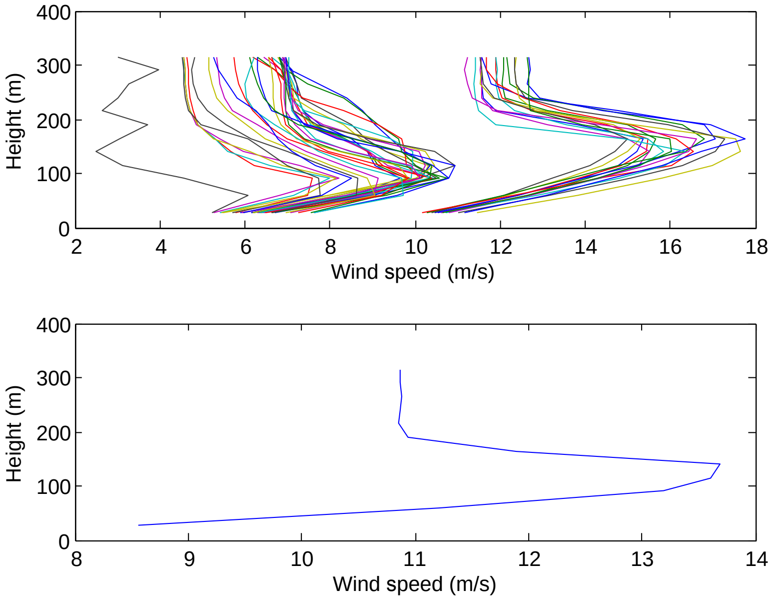

Figure A.5: *Observed LLJs with time criteria in sector 9 and 10*

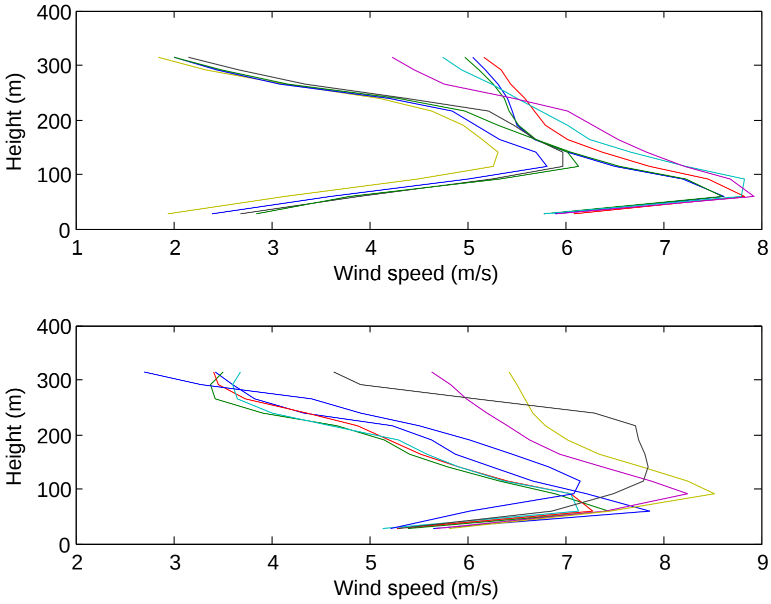

Figure A.6: *Observed LLJs with time criteria in sector 11 and 12*

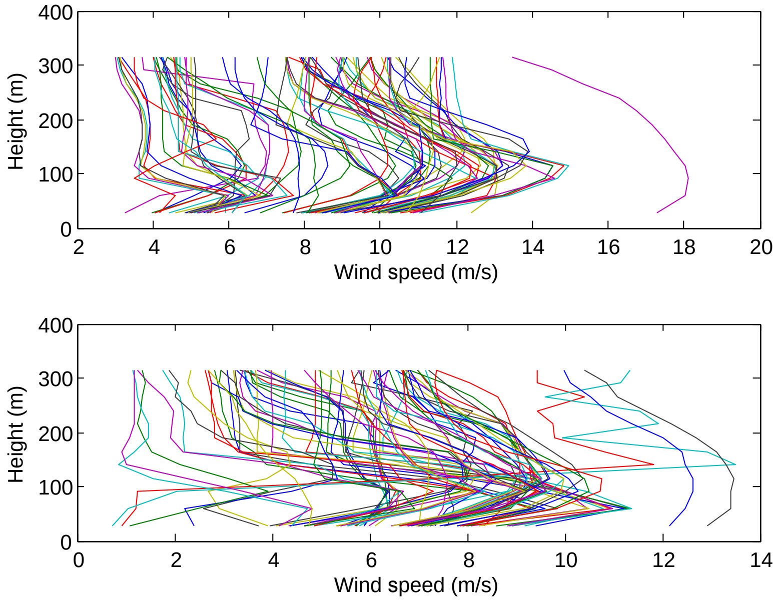

Figure A.7: *Observed LLJs without time criteria in sector 1 and 2*

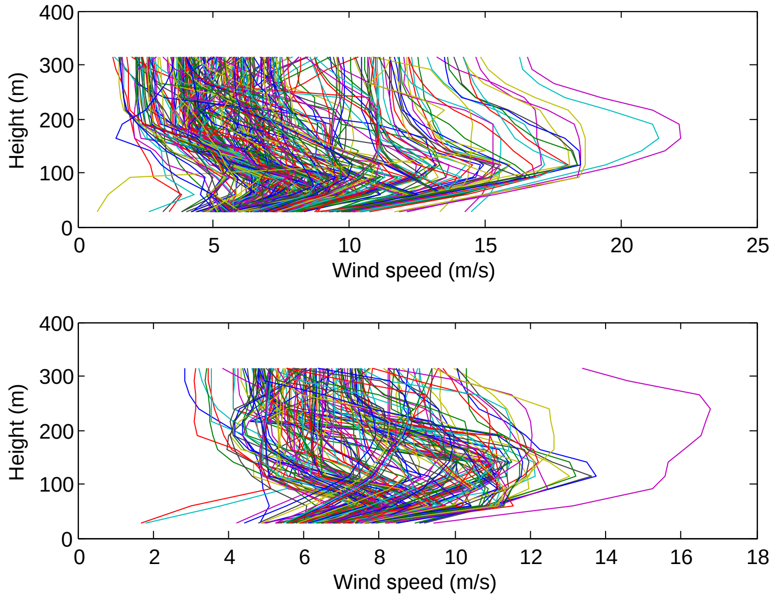

Figure A.8: *Observed LLJs without time criteria in sector 3 and 4*

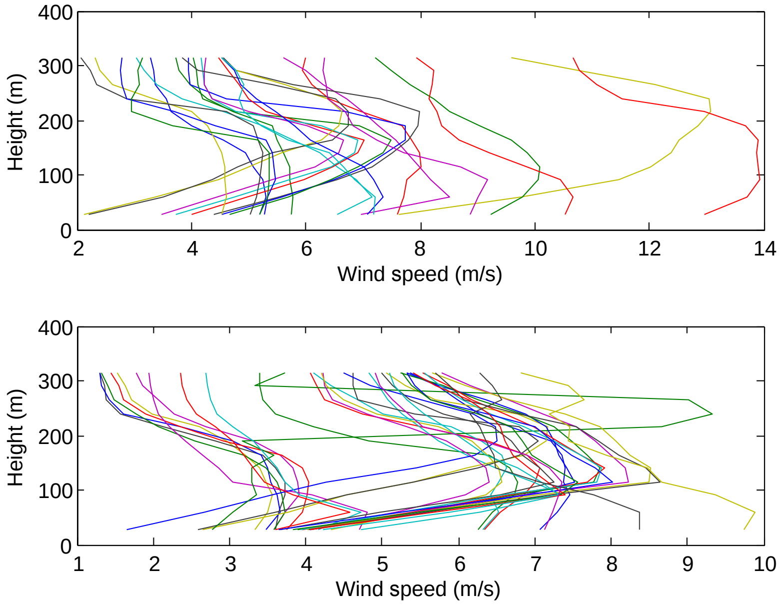

Figure A.9: *Observed LLJs without time criteria in sector 5 and 6*

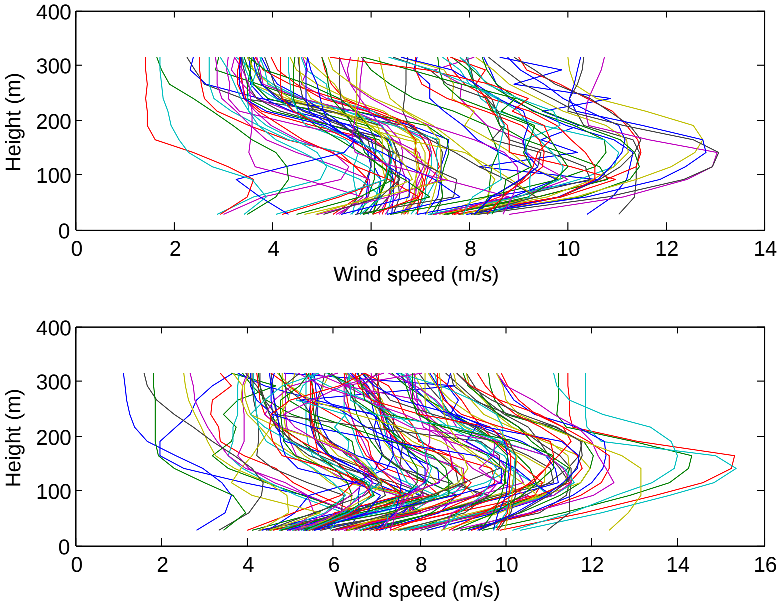

Figure A.10: *Observed LLJs without time criteria in sector 7 and 8*

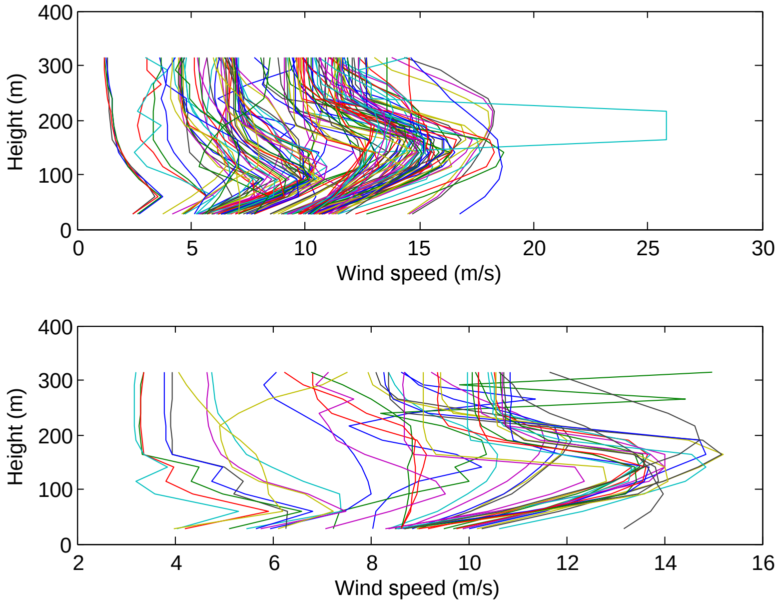

Figure A.11: *Observed LLJs without time criteria in sector 9 and 10*

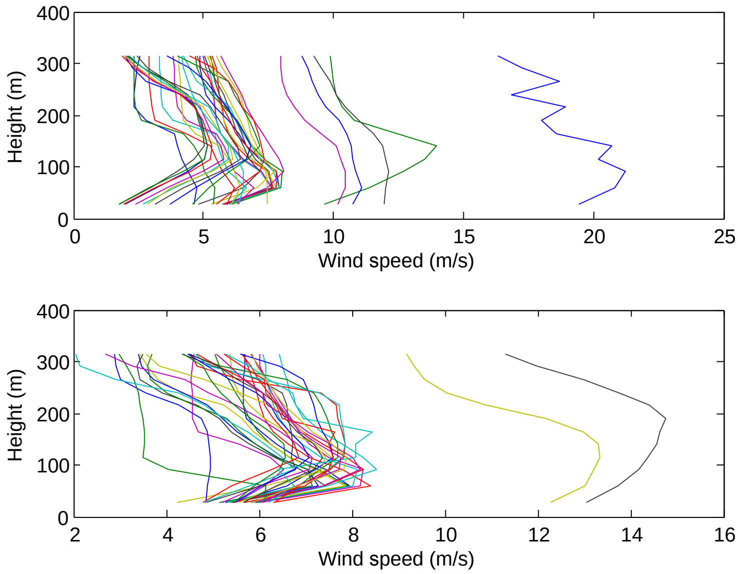

Figure A.12: *Observed LLJs without time criteria in sector 11 and 12*

Appendix B

Observed LLJs under different stability conditions

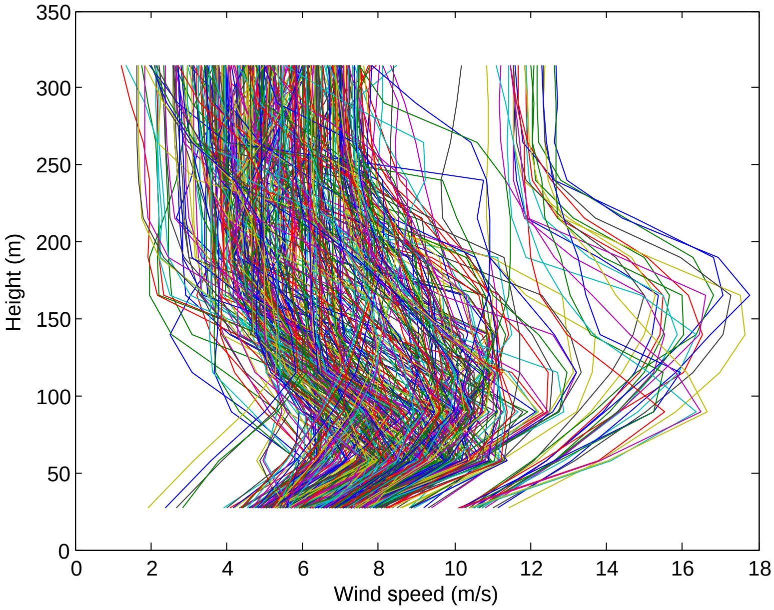

Figure B.1: *Observed LLJs with time criteria under very stable conditions*

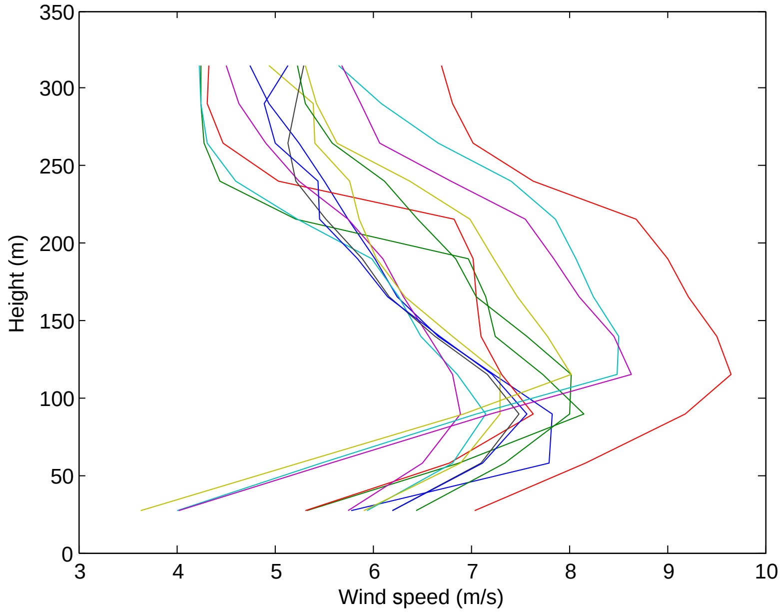

Figure B.2: *Observed LLJs with time criteria under stable conditions*

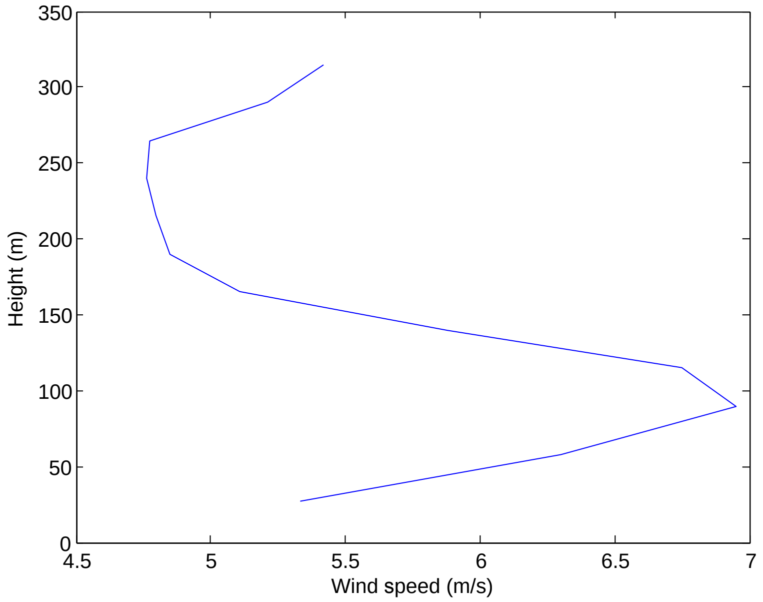

Figure B.3: *Observed LLJs with time criteria under near neutral conditions*

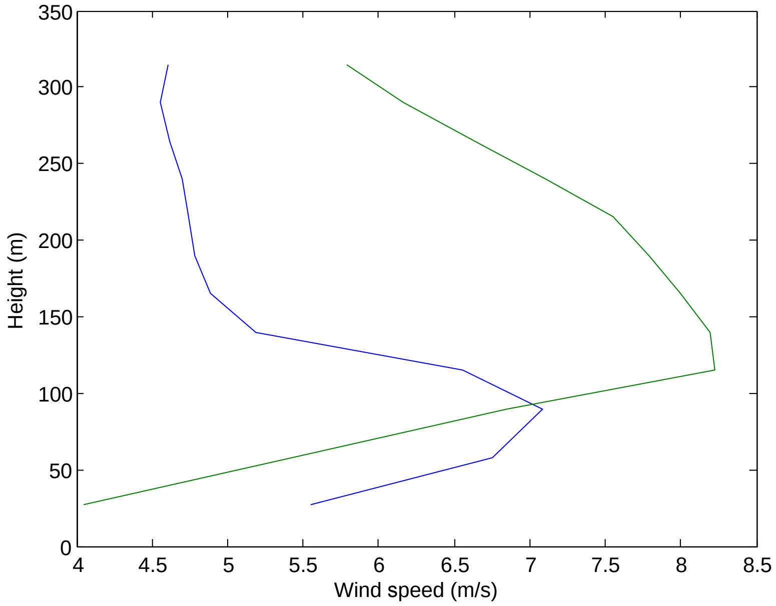

Figure B.4: *Observed LLJs with time criteria under unstable conditions*

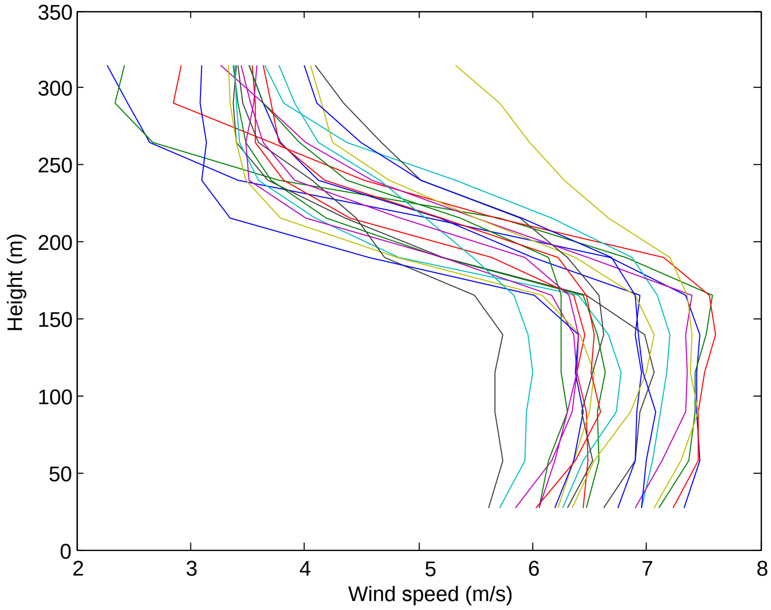

Figure B.5: *Observed LLJs with time criteria under very unstable conditions*

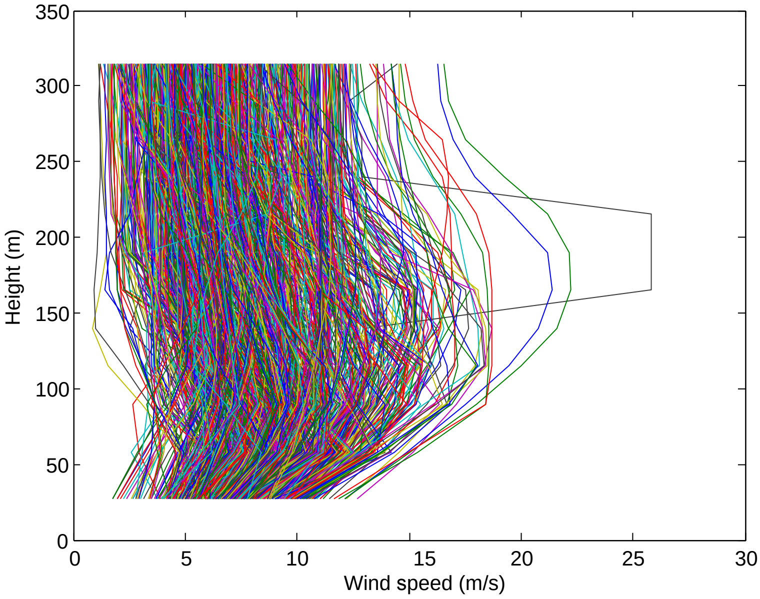

Figure B.6: *Observed LLJs without time criteria under very stable conditions*

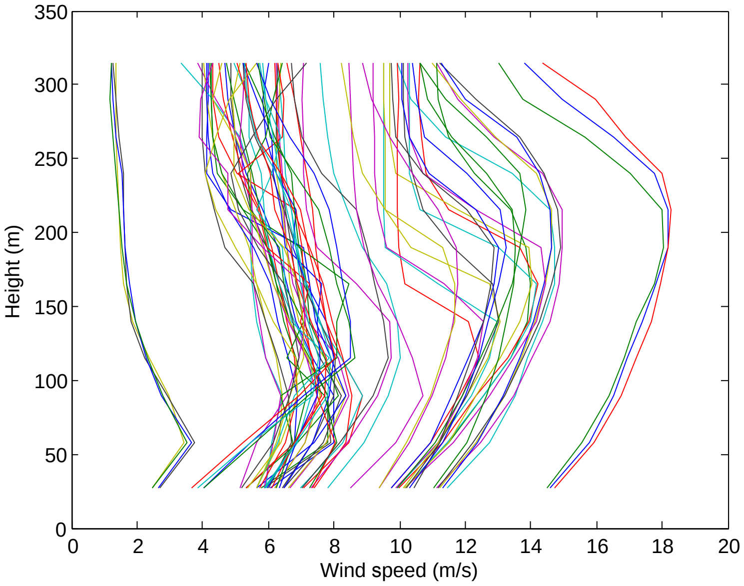

Figure B.7: *Observed LLJs without time criteria under stable conditions*

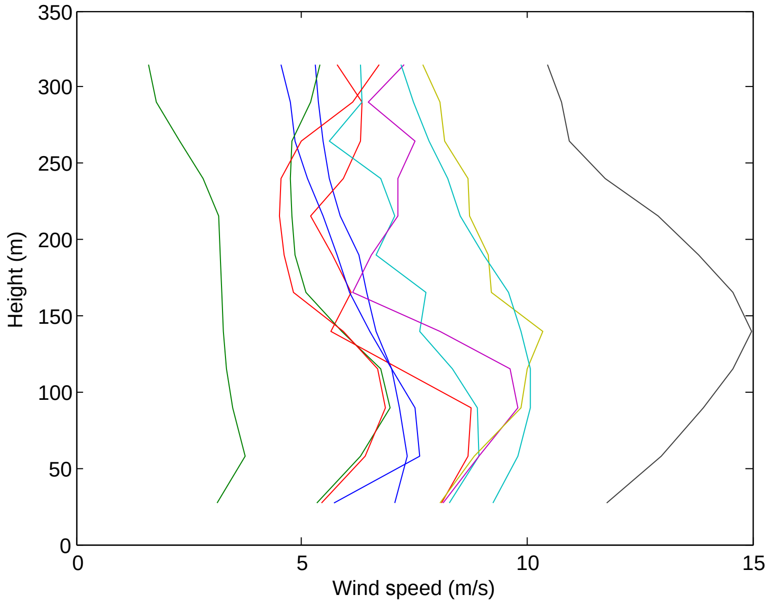

Figure B.8: *Observed LLJs without time criteria under near neutral conditions*

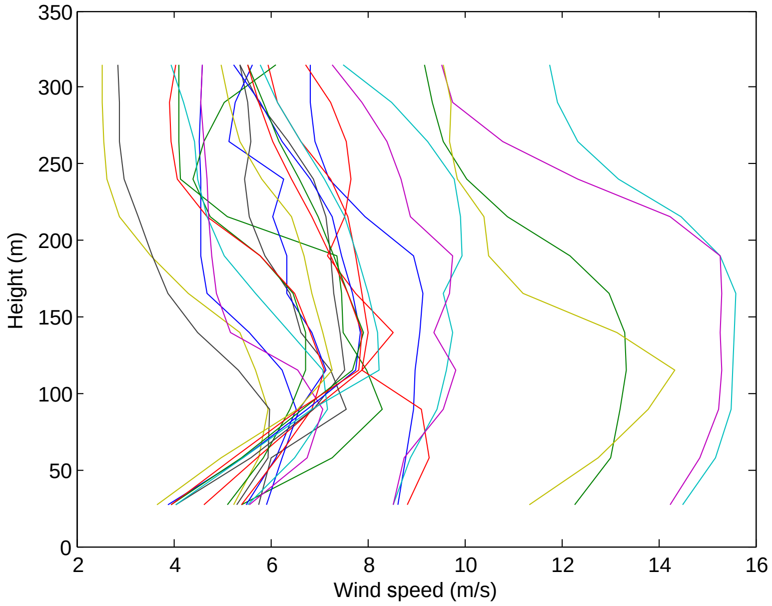

Figure B.9: *Observed LLJs without time criteria under unstable conditions*

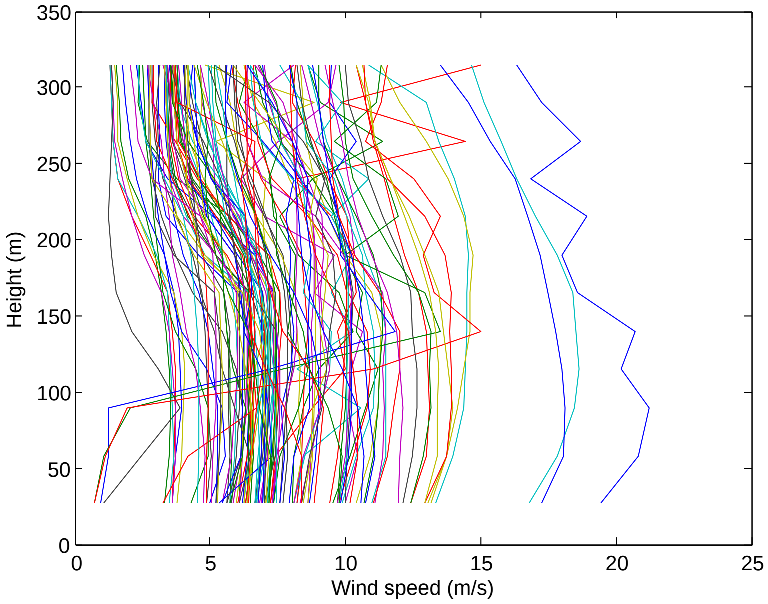

Figure B.10: *Observed LLJs without time criteria under very unstable conditions*